Dissertation-Precipitate Interactions in Magnesium-Neodymium Alloys

by

Zhihua Huang

A dissertation submitted in partial fulfillment
of the requirements for the degree of
Doctor of Philosophy
(Materials Science and Engineering)
in The University of Michigan
2019

Doctoral Committee:

Professor John E. Allison, Co-Chair
Professor Amit Misra, Co-Chair
Assistant Professor Liang Qi
Associate Professor Veera Sundararaghavan

Zhihua Huang

huzhihua@umich.edu

ORCID iD: 0000-0002-9960-0799

ACKNOWLEDGEMENTS

Looking back the past five years, I always feel blessed to receive guidance, help and love from the people surrounding me. I would like to express my gratitude at the end of this Ph.D. journey. Firstly, I would like to thank my advisors Prof. John Allison and Prof. Amit Misra. I have been knowing Prof. Allison since my undergrad time and he is always being kind and supportive to me. His mentality of hardworking and dedication on details always amazes and inspires me. I appreciate that Prof. Misra has always being strict and set a high bar to me. He is not only a supervisor that guide me to be a metallurgist and microscopist but also show me the traits of an honorable researcher who have integrity, dedication and great amount of interests toward nature. I would also like to thank my committee members Prof. Liang Qi and Prof. Veera Sundararaghavan for providing invaluable advices to shape my research and thesis. Additionally, great appreciations are paid to Prof. Qi and his student Chaoming Yang for helping me with simulation results which provide important insight to the observed mechanisms in the experiments.

I would like to show my special gratitude to Dr. Kai Sun at the Michigan Center for Material Characterization and Dr. Surendra Kumar Makineni who was the postdoc scholar in Prof. Allison group. They are so knowledgeable on electron microscopy and so kind to teach me hand-by-hand on how to operate the sophisticated instruments. I benefited from both their knowledge and good hearts.

Many thanks go to my colleagues in both Prof. Allison and Prof. Misra group. I enjoy every group meeting (if not too long) and discussion with them. Many of them become good friend of

mine. I always remember the time to talk hoop with Vir Nirankari and chat with Jacob Graves about martial art as well as hanging out with Qianying Shi and Zhenjie Yao and discuss my research plan with Qian Lei. There are also many other friends in Ann Arbor that I can’t list here but they are all very important and helpful to me.

Last but certainly not least, I am sincerely grateful to my parents and fiancée Yachi Chen who are always patient to me and show me unconditional love and support. They are my strength and faith whenever I am depressed and self-doubting. Without their support, nothing can be accomplished here. Hence, this work does not only come from my efforts but, more importantly, should be attributed to my beloved ones.

TABLE OF CONTENTS

LIST OF TABLES

LIST OF FIGURES

ABSTRACT

The dislocation-precipitate interaction in Mg-Nd alloy has been characterized by *in situ* straining in transmission electron microscopy (TEM). Postmortem study on deformed samples has been conduct on various technique including weak-beam dark field and high-angle annular dark-field scanning transmission electron microscopy (HAADF-STEM). Bulk properties data has been collected from the tensile test. In addition to experimental results, supplementary computational molecular dynamic (MD) simulation and first principle calculation provide insight and validation for found mechanisms.

The unit dynamic process between extended β_1 precipitate and basal dislocation is characterized via viewing dislocation-precipitate interaction at basal plane. Dislocations are observed to glide along precipitate broad facet. A dislocation-theory based analysis suggests that the shape, spacing and orientation (with respect to the glide plane) of β_1 precipitates may favor glide of pinned dislocations along interfaces as opposed to the classical mechanism of bowing and looping around the precipitate. The analysis also suggests the dislocation relaxation is the root cause for the interface gliding mechanism.

Further *in situ* straining and postmortem TEM dislocation analysis investigation revealed that basal <a> type dislocations interacted differently with β_1 (Mg_3Nd) and β''' ($Mg_{3\text{-}7}Nd$) precipitates. For β''' precipitates, dislocations directly shear the precipitates. For interactions with β_1 precipitates, dislocations were observed to by-pass the precipitates and then cross-slip to prismatic planes. The cross-slip associated with β_1 precipitates occurred at either the departure or

front end of the lenticular shaped phase. Dislocations with screw characteristic are able to overcome β_1 precipitate by double cross-slip. The cross-slip mechanism was explored by MD simulations, and found to be similar to the Friedel-Escaig mechanism in pure Mg. The role of cross-slip in a β_1-precipitate-dominant microstructure in enhancing ductility is discussed.

The cross-slip mechanism introduces dislocation kink receiving strong lattice resistance along propagating direction, which is suspected to prevent following dislocation motion and finally leads to dislocation pile-up. The dislocation pile-up phenomenon was then observed in *in situ* straining experiment. Analysis of the images from the *in situ* experiments as well as postmortem TEM of bulk deformed samples reveals that, in the presence of a dislocation pile-up of sufficient intensity, slip is transmitted through the β_1 precipitates. This impediment to dislocation motion from planar precipitate facets is analyzed using dislocation theory and density functional theory calculations. It is shown that the β_1 precipitate “walls” result in a strong but not impenetrable barrier to slip transmission.

The imposed dislocations pile-up effect on β_1 precipitates is systematically characterized from tensile and compressive sample. In the tensile samples, contrary to the one single plane shearing as expected from classic precipitate cutting mechanism, several shearing events occur at a series slip plane parallel to each other, resulting in a region of deformation layer. The precipitates are significantly deformed within the layer but still remain connected. MD simulations validate the experiment result and show that deformation gradually spread across the layer, indicating a new mechanism to accommodate imposed displacement from shearing events. In the compressive samples, precipitates are more vulnerable to fragment into small pieces, which is suspected to associate with the buckling effect from c axis compressive stress

CHAPTER 1

Introduction

Magnesium as the lightest structural material in the word receives great attention and research interests for its potential applications in automobile, aerospace, consumer electronic industries. Magnesium research primarily follows a similar methodology to counterpart aluminum alloys. Precipitation hardening as a most important strengthening mechanism in aluminum alloy has also been adopted to produce high strength magnesium alloys. Mg-Rare Earth (RE) alloys appear to be a promising alloys system because RE elements have high solubility in the magnesium matrix at elevated temperature and the solubility dramatically decreases as temperature goes down, making it ideal for precipitation hardening. Specifically, the plate-shape β_1 precipitates are uniformly distributed in the matrix, lying uniquely on prismatic plane. This morphology is regarded as the most effective one to inhibit basal dislocations motion, which make β_1 precipitates promising in future alloy design.

However, the yield strength of precipitation hardened magnesium alloys is still inferior to their counterpart aluminum alloys, even though the precipitate volume fraction is comparable. A commercial Mg-RE alloy WE54 (Mg-Y-Nd) has a yield strength around 225MPa for T6 condition, while the yield strength of 7075 aluminum alloy is above 500MPa for the same temper. Besides yield strength, the ductility of Mg-RE is limited as well (4% *vs.* 11% for the comparison alloys).

For future alloy development, it is crucial to understand the fundamental deformation mechanism at the nano- and meso-scale in order to design the ideal material microstructure.

It is well known that dislocations motion and their interaction with other defects and second phases plays an important role on determining mechanical behavior. In precipitation hardened Mg-RE alloy, this is heavily dependent on the interaction between dislocations and precipitates. Although classic models have been established for dislocation-precipitate interactions such as Orowan looping and the Hirsch prismatic loop model to bypass the blocking precipitates, they are still insufficient and incomplete for magnesium alloys. Firstly, the classic models are generally based on spherical precipitates while the precipitates in the Mg-RE alloy are generally high aspect ratio plates. In this study, it will shown that the large broad facet of the beta1 precipitate plate alters the interaction mechanism. Secondly, the dislocation-precipitate interaction dynamic process may depend on the matrix structure. The prismatic loop described in Hirsh model is absent in the Mg-Nd alloy conditions described in this dissertation because the double cross-slip dislocation jog is still mobile in the hexagonal closed packed (HCP) structure.

With the utilization of *in situ* straining in TEM and postmortem TEM, the two fundamental questions that are addressed in this thesis are the following:

1. What is the dynamic unit dislocation-precipitate interactions process for precipitates in Mg-RE alloy?
2. What impact the dislocation-precipitate interactions imposes to the deformed precipitates structure and mechanical behavior?

The experimental result reveals the dynamic interaction process between basal dislocations and β''' and β_1 precipitates, showing the importance of precipitate type on mechanical properties.

Furthermore, the unit interaction mechanism is also critical for Dislocation Dynamics (DD) simulation, as the work is part of the PRdictive Integrated Structural Material Science Center (PRISMS) in University of Michigan where cooperative experimental and simulation groups implement Integrated Computational Material Engineering (ICME) principle for next generation alloy development. A correct dislocation-precipitate interaction mechanism is necessary and essential for simulation results to predict the accurate material behavior.

CHAPTER 2

Literature Review

This chapter gives an overview of the deformation mechanics in magnesium HCP structure, representative strengthening precipitates in Mg-RE alloys and classic dislocation-precipitate interaction mechanisms. These sections set the foundation of the work. It provides an overview of the hcp slip systems and observed precipitates in Mg alloys. This chapter also highlights the perspective provided by previous research and how that body of research inspires this work.

2.1 Deformation Mechanics in Magnesium Alloys

2.1.1 Slip System and Twinning

Many slip systems are exhibited by the magnesium HCP structure. Mg is known for its plasticity anisotropy as these different slip systems possess significantly different values for the critical resolved shear stress (CRSS). Fig. 2.1 shows five deformation modes in Mg, namely basal, prismatic, pyramidal I and II, and tensile twinning systems. At room temperature, basal dislocations are activated much easier than other slip systems as shown in Fig. 2.2. The ratio between prismatic and basal CRSS is usually around 100 from single crystal studies [2]. However, polycrystal results show an almost identical CRSS between prismatic and basal slip [Agnew, Sean R 2005, Koike, J 2003]. The difference is argued by Koike that the triple points serve as stress concentrator which will amplify the applied stress ten times larger. Yet, even taking account of the stress intensity from polycrystals, it will reduce the ratio to 10 which is still significantly higher than 1. The discrepancy between single and polycrystal study is still unclear.

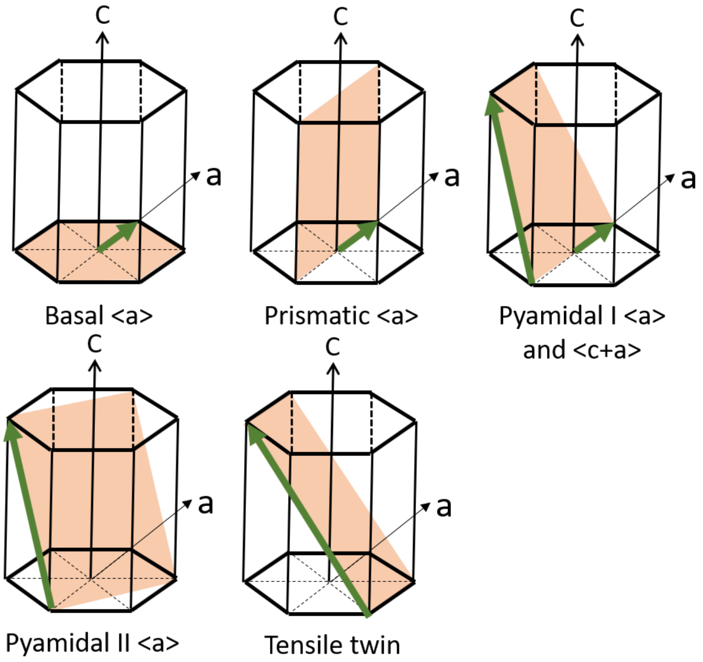

Fig. 2. 1 Deformation systems in Mg. Green arrows represent Burgers vector and light orange shaded area represents the slip planes.

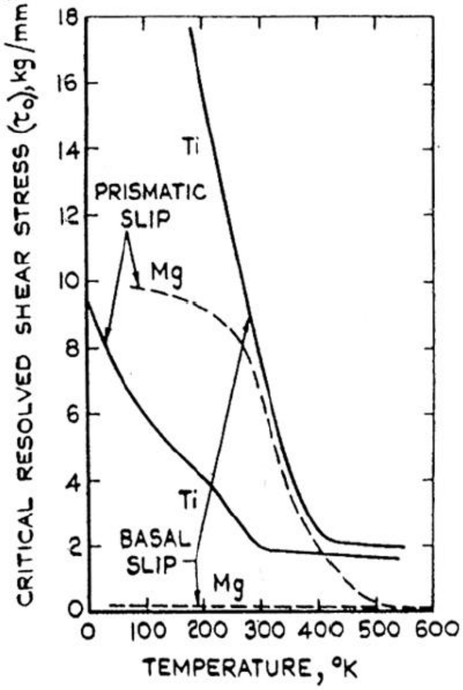

Fig. 2. 2 The CRSS of basal and prismatic slip in Ti and Mg singles crystals at various temperatures [1]

Prismatic slip can also generated from basal dislocation cross-slip. *Couret* and *Caillard* [2] published their *in situ* TEM work on prismatic slip in single crystal Mg showing the prismatic glide is controlled by thermally activated motion of rectilinear screw component, known as the Friedel-Escaig (F-E) mechanism [3]. According to F-E mechanism (F-E), a cross-slipped basal dislocation is dissociated into two partial dislocations on the basal plane, and glides by thermally activated kink pairs propagating along the length of the basal screw dislocation. The mechanism is shown in Fig. 2.3

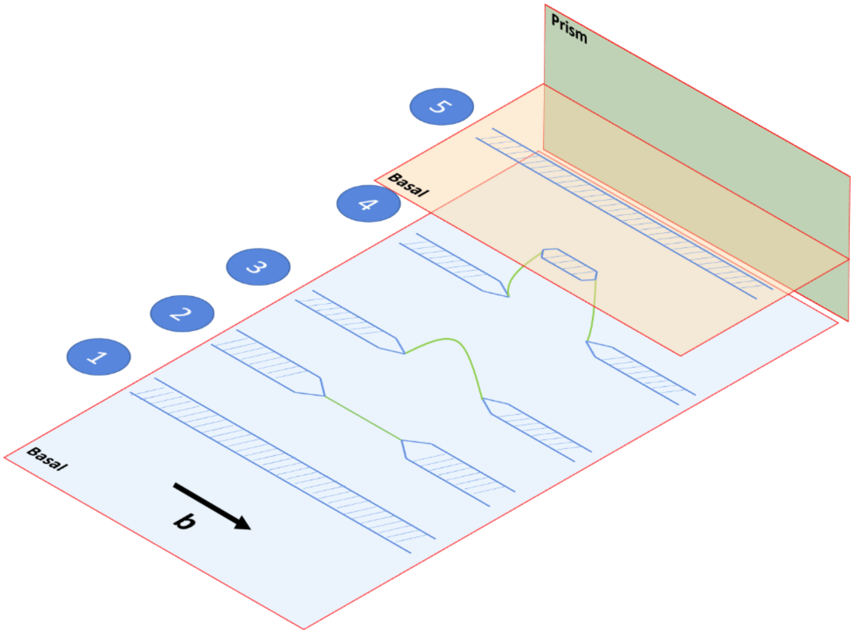

Fig. 2. 3 Schematic of the Friedel-Escaig (F-E) cross-slip mechanism. The mechanism sequence is numbered. The shadow areas represent stacking faults on the basal plane (Blue box Basal) and green lines represent the perfect screw dislocation segment that cross slips on the prismatic plane (Green box Prism) before dissociation to partials on an adjacent basal plane (Orange box Basal).

Twinning is another major deformation mode that occurs at room temperature in Mg alloys [4]. Furthermore, twinning and <c+a> dislocations are the only two deformation modes that can accommodate strain along c axis. The CRSS for tensile twin nucleation is less than <c+a> dislocation, prioritizing it to activate before <c+a> dislocation. However, unlike <c+a> dislocation, twinning is irreversible and can only accommodate c axis strain as much as 12%.

Twinning is classified as compression twin {10-11}[10-12] and tension twin {10-12}[10-11]. The activation of certain twinning type depends on the applied stress vector. The compression twin occurs much less than tensile twin because of its high CRSS to nucleate. The difference between compression and tensile twin CRSS makes Mg alloys vulnerable for tension-compression yield asymmetry (TCYA) [4], which presents another challenge for Mg alloys to industrial application.

In contrast to twinning, <c+a> dislocations are sustainable to accommodate strain along c axis, which makes it very attractive for ductility improvement. It hence attracts significant amount of research in recent years. Many experiments have shown <c+a> dislocations are generated when compressed along c axis in single crystal Mg. Some researches show the <c+a> dislocations activate on pyramidal II plane [5, 6] while some show in pyramidal I plane [7]. Recent MD simulation [8] have suggested that <c+a> dislocation can nucleate and slipped at pyramidal I plane with much less stress but able to be cross slipped to pyramidal II plane under higher stress. The <c+a> cross-slip mechanism between pyramidal I and II plane has been proposed to be critical to maintain magnesium plasticity [9].

Both <a> and <c+a> dislocations can dissociate into partial dislocation in magnesium matrix following equation 2.1 and 2.2.

$$\frac{1}{3}[1\bar{2}10] \rightarrow \frac{1}{3}[10\bar{1}0] + \frac{1}{3}[01\bar{1}0] \qquad (2.1)$$

$$\frac{1}{3}[\bar{2}113] \rightarrow \frac{1}{6}[\bar{2}20\bar{3}] + \frac{1}{6}[\bar{2}02\bar{3}] \qquad (2.2)$$

The basal <a> and non-basal <a> dislocation will dissociate into two Shockley partial dislocations but only stacking fault in basal plane is energetically stable [10]. However, <c+a> dislocations dissociate into two sessile basal Frank partials dislocation since the Burgers vector does not lie on the slip plane. Detailed two beam condition studies for such dissociation have been conducted by Sandlobes *et al* [11] and further analyzed by Agnew *et al* [12] as shown in Fig. 2.4.

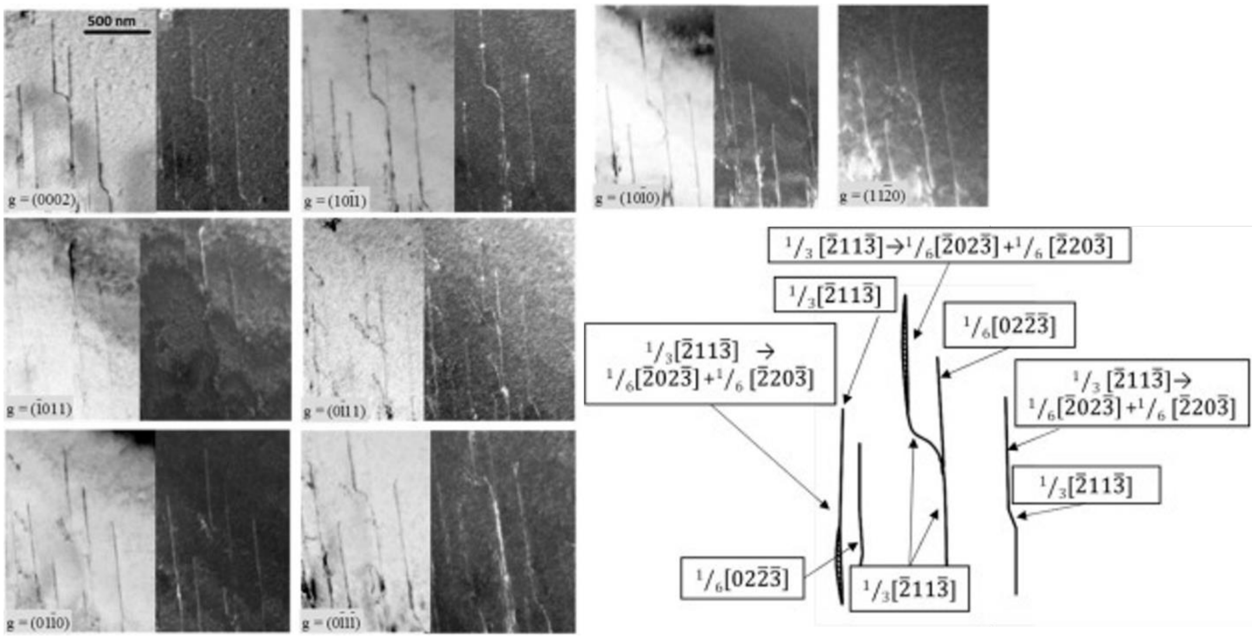

Fig. 2. 4 Bright and Dark field TEM images for eight two beam conditions. The schematic shows the concluding dislocation dissociation reaction corresponding to the experimental result [12]. The experiment is performed by Sandlobes et al in Mg-Y alloy [11].

2.1.2 Ductility in Magnesium Alloys

As shown in previous section, basal slip is the dominant deformation mode in magnesium alloys at room temperature. The large discrepancy of CRSS in different slip systems results in plastic anisotropy. According to Taylor criterion, a minimum of five independent slip systems are required to achieve homogeneous ductility [13]. However, the basal slip systems in magnesium can only provide two independent slip systems. As mentioned, the twinning system can only accommodate certain amount of strain and being irreversible, hence can count as a half slip system. Therefore, the Taylor criterion is not satisfied by these two deformation modes alone in magnesium alloys. Moreover, even though the resolved shear stress is large enough to activate <c+a> dislocations, as shown by equation 2.2, they will spontaneously dissociate into sessile basal dislocations. Fig. 2.5 shows the MD simulation performed by Curtin *et al.* [14], exhibiting the <c+a> dislocations dissociate into different sessile configurations under different stress states.

Dissociated dislocations has partial dislocation characteristic as shown in the hexagonal schematic in Fig. 2.5. As suggested by MD simulations, <c+a> dislocations dissociate into basal plane with out of basal plane Burgers vectors, hence to be sessile dislocations.

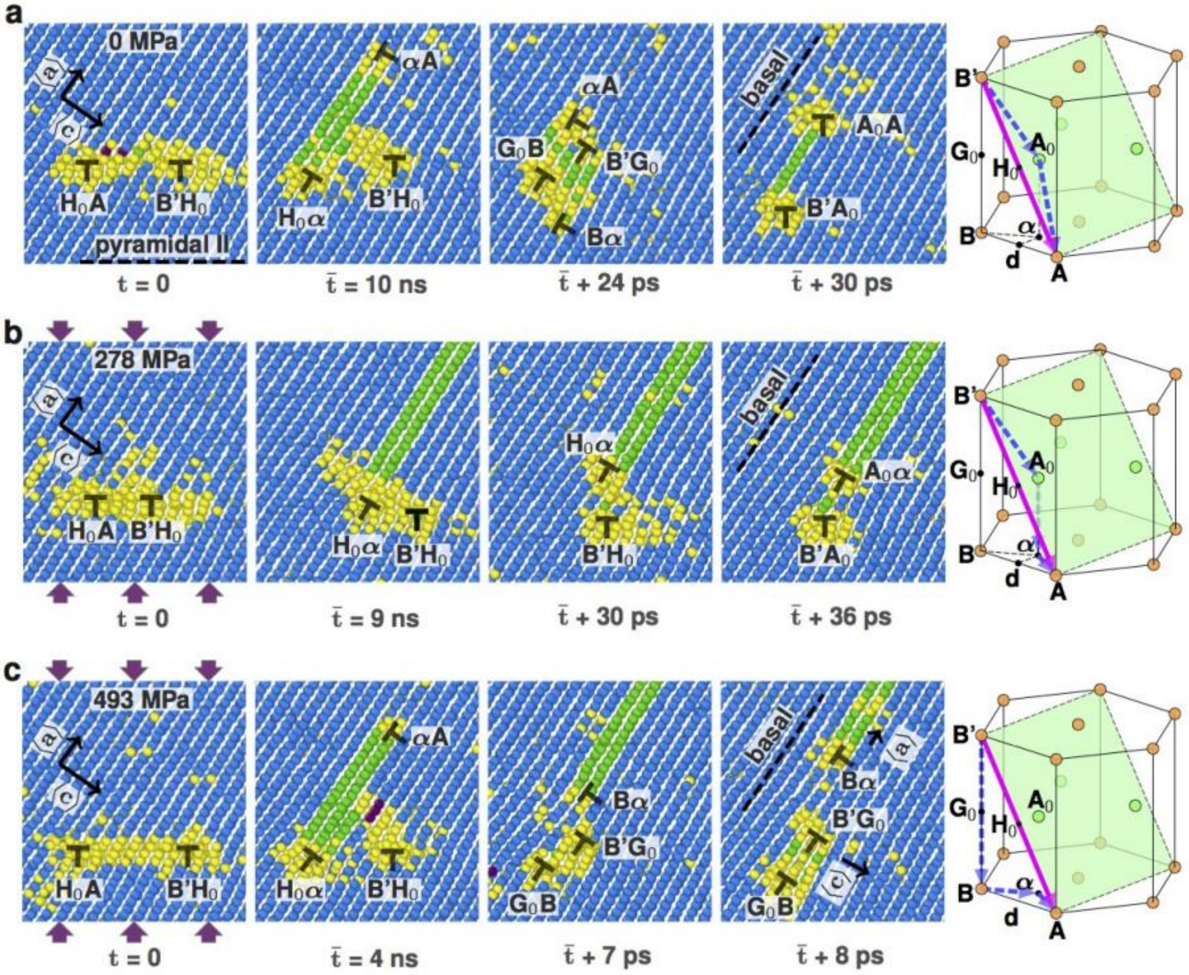

Fig. 2. 5 Transition of easy glide pyramidal II <c+a> dislocation to sessile basal dislocations under different stress states [14].

The MD simulations correspond to the HAADF-STEM image on <c+a> dissociated dislocations core structure [15] as shown in Fig. 2.6. In image b), the Burgers vector loop indicate it has a Burgers vector of A_0A in Fig. 2.5 a). The atomic structure reaches a good agreement between MD simulations and HAADF-STEM characterization outside of dislocation core.

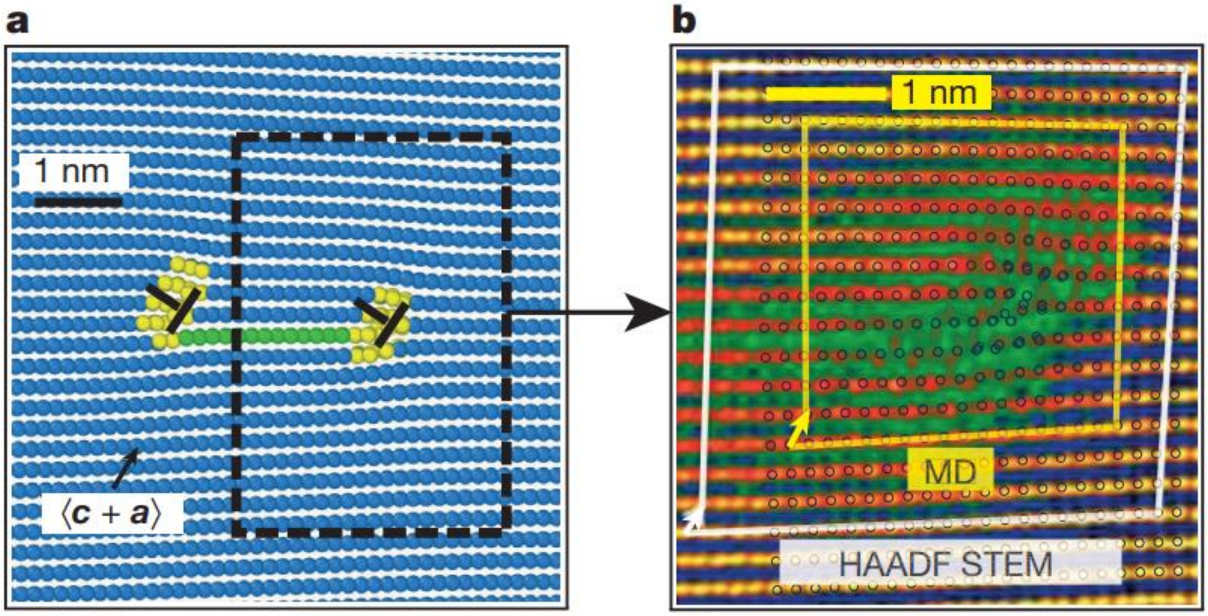

Fig. 2. 6 Comparison between MD simulation and HAADF-STEM image on <c+a> dissociated basal dislocations [14]. Image b) shows the core structure of A0A dislocation in Fig. 2.5 a). White circle is the superposition of atomic positions from MD simulations.

The dissociated dislocations behave as obstacles to incoming dislocations leading to a rapid strain hardening for pure magnesium. The transition between glissile **P**yramidal dislocations to the sessile **B**asal dislocations (PB transition) are believed as the origin of low ductility of magnesium alloys [14]. Because of the lack of adequate number of independent slip systems and <c+a> PB transition, magnesium is generally regarded as having poor ductility. However, exceptional ductility is found in many fine grained samples. Koike *et al*. [17] utilized severe plastic deformation (SPD) to process AZ31B alloys producing a refined grain size that exhibited greater than 45% tensile elongation at room temperature. Based on dislocation analysis in a highly deformed sample, Koike found an abundance (40%) of non-basal <a> type dislocations, suggesting the profuse occurrence of cross-slip activity. Similar result was shown by Agnew *et al*. [18] as well, who further pointed out that the non-basal cross-slip can provide two extra independent slip systems 1/3<1-210>(10-10), so a total of four independent slip systems can be activated. The promotion of extra non-basal slip systems might account for increased room temperature tensile ductility, particularly under deformation conditions such as unconstrained in-plane tension.

Although the combination of basal and non-basal <a> dislocation can efficiently accommodate ductility along a axis, the bottleneck of improved ductility is still the limit on c axis deformation, which is controlled by <c+a> dislocation. Rare earth (RE) element addition have been proven to be effective, not only does it weaken the texture after rolling or extrusion but it also promotes <c+a> dislocation activity [19]. Fig. 2.7 shows the ductility improvement after RE addition [20].

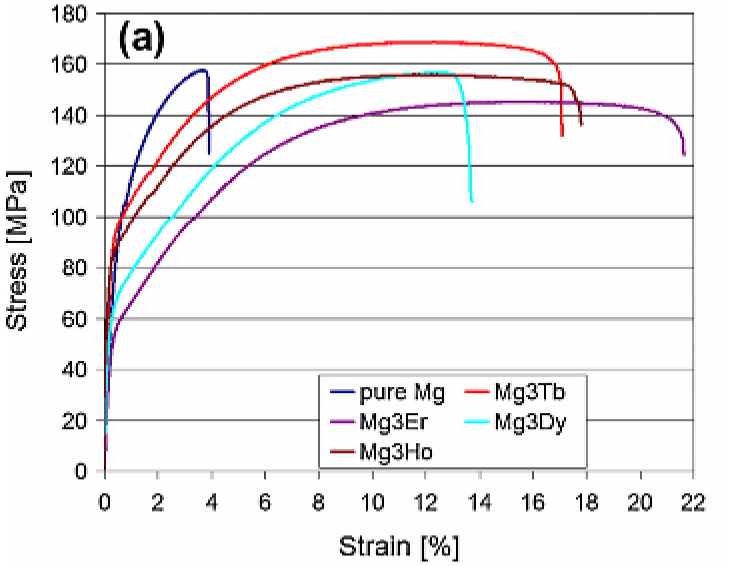

Fig. 2. 7 Ductility improvement after RE addition [20]

The ductility improvement in the Mg-RE alloy has been attributed to several different factors. The nucleation of pyramidal <c+a> dislocations are regarded as the critical step in producing the out-of-plane shear. I_1 stacking fault can enable the formation of dislocation structure on pyramidal plane. Additionally, it is commonly acknowledged that RE addition will lower the stacking fault energy. It is argued that the lower stacking fault energy will generate more I_1 stacking fault where will serve as heterogeneous source to the <c+a> dislocations. [21]. In the contrast, this ideology is not compatible with PB transition theory. Recent density functional theory (DFT) [22] shows the effect of Y addition on basal stacking fault energy can also be achieved by Al at similar amount and the effect on pyramidal plane stacking fault can be achieved by Zn as well. The result suggests that the ductility improvement with Y addition is not tightly associated with the stacking fault energy. On the other hand, they propose [9] that the Y addition reduces the <c+a> dislocation cross-slip energy between pyramidal I and II plane, therefore preventing the <c+a> dislocations from transition to sessile basal dislocations.

There have been fewer studies investigating the ductility mechanism of precipitation hardened alloys and it is generally believed that precipitation hardening will decrease the ductility for a given strength increment [Zhang 2008, 25, 16]. For example, commercial alloy AZ91 shows a precipitation hardening at a cost of ductility. Fig. 2.8 shows the trend of strength and ductility as aging time increases.

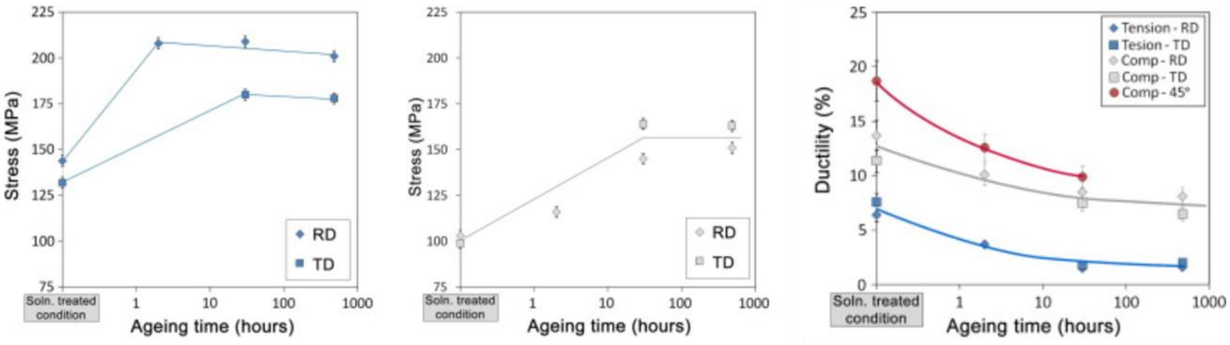

a) tension b) compression c) Ductility

Fig. 2. 8 The strength and ductility of AZ91 at different aging times [16].

Nevertheless, many researches show some of the precipitation hardened magnesium alloys exhibit good ductility compared to solution heat treatment (SHT) condition [Zhang 2008, 24, 25]. In the Guinier-Preston (GP) zone hardened Mg-Al-Ca-Mn alloy, Bhattacharyya *et al.* [25] report that this alloy has a good combination of strength and ductility at peak aged condition which contains high density of GP zone, as shown in Fig. 2.9. It is attributed to the GP zone that provide an increase in yield strength and avoid deleterious effect of conventional precipitation such as being nucleation sites for voids, leading to heterogeneous slip distribution and precipitation free zone. Further plasticity modeling study [26] suggests, the GP zone hardens both basal and prismatic plane and reduce the anisotropy of grain single crystal yield surface. The reduction on plasticity anisotropy is most likely why the ductility is preserved.

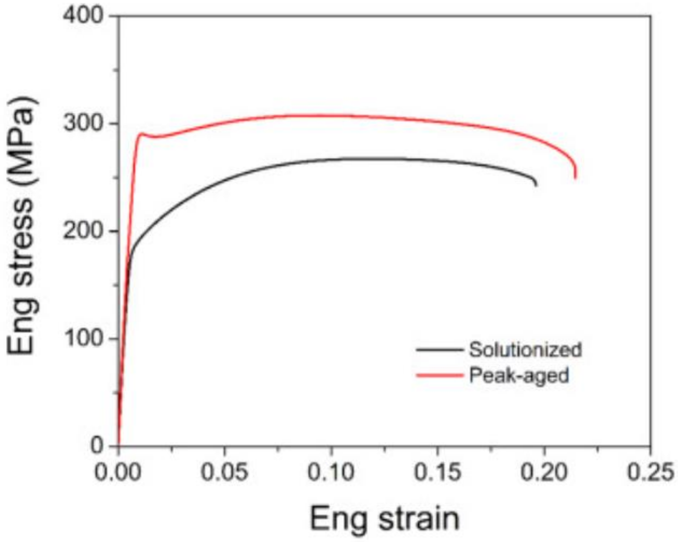

Fig. 2. 9 the engineering stress-strain curve for solutionized and peak-aged conditions in Mg-Al-Ca-Mn alloy [25].

2.2 Precipitation in Mg-Rare Earth Alloys

The precipitation hardening sequence is shown in the Table 2.1 [27] It is noticeable that most of the Mg-RE alloys share similar precipitation sequence. Among these precipitates, β'', β' and β_1 precipitates are common strengthening phases in Mg-RE alloys:

1. Fine and having a similar structure to the magnesium matrix (β'' and β' precipitates)
2. Coarse and having a different structure to the magnesium matrix (β_1 precipitates)

Instead of elaborating all existing precipitates, this section will review specifically the structure and composition of selected precipitates in Mg-Nd alloy, whose interactions with dislocations have been extensively studied in this thesis research.

Table 2. 1 Part of the whole precipitation sequence in individual magnesium alloy systems [27]

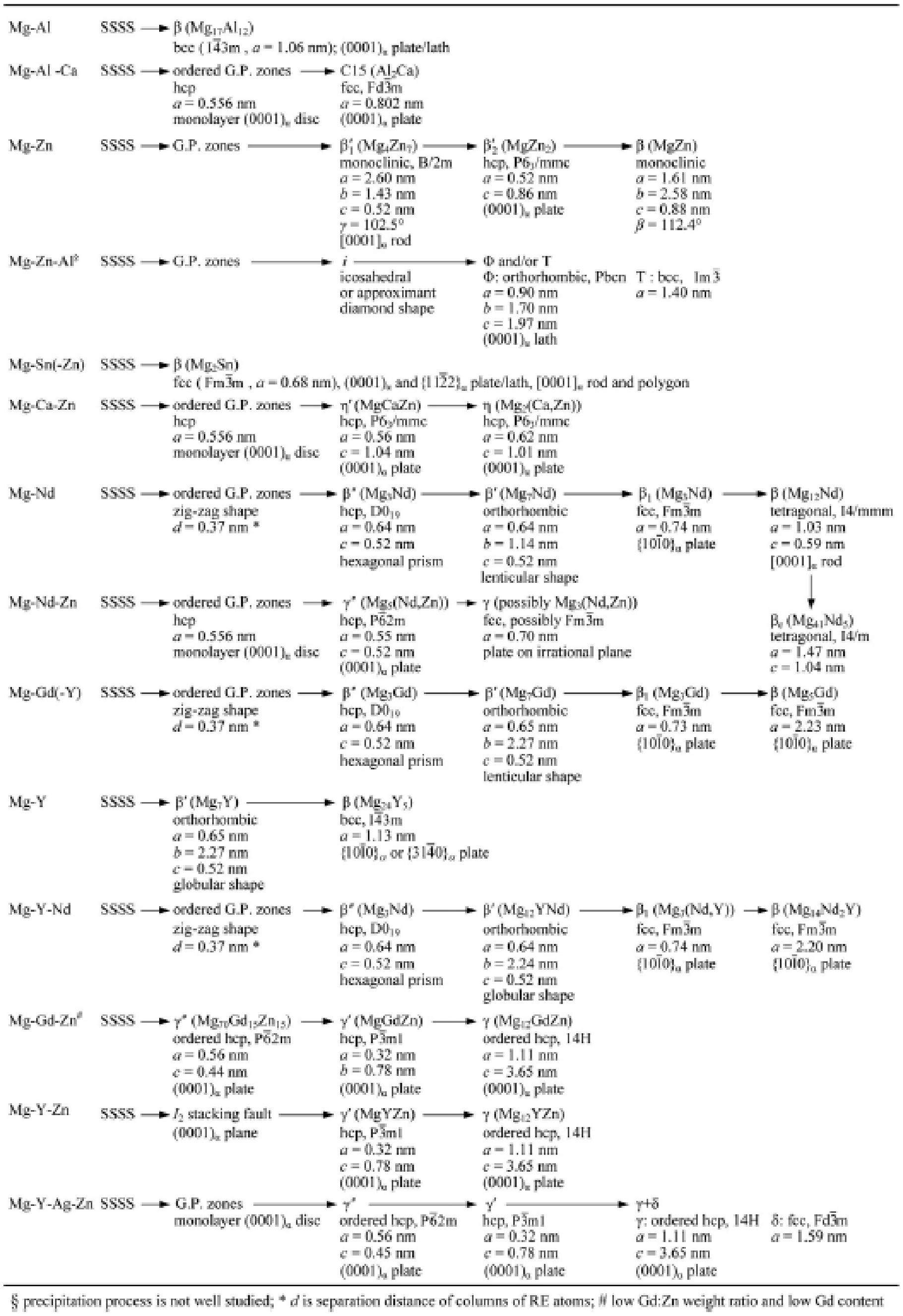

Mg-Al	SSSS	→ β ($Mg_{17}Al_{12}$) bcc ($I\bar{4}3m$, a = 1.06 nm); $(0001)_\alpha$ plate/lath				
Mg-Al -Ca	SSSS	→ ordered G.P. zones hcp a = 0.556 nm monolayer $(0001)_\alpha$ disc	→ C15 (Al_2Ca) fcc, $Fd\bar{3}m$ a = 0.802 nm $(0001)_\alpha$ plate			
Mg-Zn	SSSS	→ G.P. zones	→ β_1' (Mg_4Zn_7) monoclinic, B/2m a = 2.60 nm b = 1.43 nm c = 0.52 nm γ = 102.5° $[0001]_\alpha$ rod	→ β_2' ($MgZn_2$) hcp, $P6_3/mmc$ a = 0.52 nm c = 0.86 nm $(0001)_\alpha$ plate	→ β (MgZn) monoclinic a = 1.61 nm b = 2.58 nm c = 0.88 nm β = 112.4°	
Mg-Zn-Al§	SSSS	→ G.P. zones	→ i icosahedral or approximant diamond shape	→ Φ and/or T Φ: orthorhombic, Pbcn a = 0.90 nm b = 1.70 nm c = 1.97 nm $(0001)_\alpha$ lath	T : bcc, $Im\bar{3}$ a = 1.40 nm	
Mg-Sn(-Zn)	SSSS	→ β (Mg_2Sn) fcc ($Fm\bar{3}m$, a = 0.68 nm), $(0001)_\alpha$ and $\{11\bar{2}2\}_\alpha$ plate/lath, $[0001]_\alpha$ rod and polygon				
Mg-Ca-Zn	SSSS	→ ordered G.P. zones hcp a = 0.556 nm monolayer $(0001)_\alpha$ disc	→ η' (MgCaZn) hcp, $P6_3/mmc$ a = 0.56 nm c = 1.04 nm $(0001)_\alpha$ plate	→ η ($Mg_2(Ca,Zn)$) hcp, $P6_3/mmc$ a = 0.62 nm c = 1.01 nm $(0001)_\alpha$ plate		
Mg-Nd	SSSS	→ ordered G.P. zones zig-zag shape d = 0.37 nm *	→ β'' (Mg_3Nd) hcp, $D0_{19}$ a = 0.64 nm c = 0.52 nm hexagonal prism	→ β' (Mg_7Nd) orthorhombic a = 0.64 nm b = 1.14 nm c = 0.52 nm lenticular shape	→ β_1 (Mg_3Nd) fcc, $Fm\bar{3}m$ a = 0.74 nm $\{10\bar{1}0\}_\alpha$ plate	→ β ($Mg_{12}Nd$) tetragonal, I4/mmm a = 1.03 nm c = 0.59 nm $[0001]_\alpha$ rod ↓
Mg-Nd-Zn	SSSS	→ ordered G.P. zones hcp a = 0.556 nm monolayer $(0001)_\alpha$ disc	→ γ'' ($Mg_3(Nd,Zn)$) hcp, $P\bar{6}2m$ a = 0.55 nm c = 0.52 nm $(0001)_\alpha$ plate	→ γ (possibly $Mg_3(Nd,Zn)$) fcc, possibly $Fm\bar{3}m$ a = 0.70 nm plate on irrational plane		β_e ($Mg_{41}Nd_5$) tetragonal, I4/m a = 1.47 nm c = 1.04 nm
Mg-Gd(-Y)	SSSS	→ ordered G.P. zones zig-zag shape d = 0.37 nm *	→ β'' (Mg_3Gd) hcp, $D0_{19}$ a = 0.64 nm c = 0.52 nm hexagonal prism	→ β' (Mg_7Gd) orthorhombic a = 0.65 nm b = 2.27 nm c = 0.52 nm lenticular shape	→ β_1 (Mg_3Gd) fcc, $Fm\bar{3}m$ a = 0.73 nm $\{10\bar{1}0\}_\alpha$ plate	→ β (Mg_5Gd) fcc, $Fm\bar{3}m$ a = 2.23 nm $\{10\bar{1}0\}_\alpha$ plate
Mg-Y	SSSS	→ β' (Mg_7Y) orthorhombic a = 0.65 nm b = 2.27 nm c = 0.52 nm globular shape	→ β ($Mg_{24}Y_5$) bcc, $I\bar{4}3m$ a = 1.13 nm $\{10\bar{1}0\}_\alpha$ or $\{31\bar{4}0\}_\alpha$ plate			
Mg-Y-Nd	SSSS	→ ordered G.P. zones zig-zag shape d = 0.37 nm *	→ β'' (Mg_3Nd) hcp, $D0_{19}$ a = 0.64 nm c = 0.52 nm hexagonal prism	→ β' ($Mg_{12}YNd$) orthorhombic a = 0.64 nm b = 2.24 nm c = 0.52 nm globular shape	→ β_1 ($Mg_3(Nd,Y)$) fcc, $Fm\bar{3}m$ a = 0.74 nm $\{10\bar{1}0\}_\alpha$ plate	→ β ($Mg_{14}Nd_2Y$) fcc, $Fm\bar{3}m$ a = 2.20 nm $\{10\bar{1}0\}_\alpha$ plate
Mg-Gd-Zn#	SSSS	→ γ'' ($Mg_{70}Gd_{15}Zn_{15}$) ordered hcp, $P\bar{6}2m$ a = 0.56 nm c = 0.44 nm $(0001)_\alpha$ plate	→ γ' (MgGdZn) hcp, $P\bar{3}m1$ a = 0.32 nm b = 0.78 nm $(0001)_\alpha$ plate	→ γ ($Mg_{12}GdZn$) ordered hcp, 14H a = 1.11 nm c = 3.65 nm $(0001)_\alpha$ plate		
Mg-Y-Zn	SSSS	→ I_2 stacking fault $(0001)_\alpha$ plane	→ γ' (MgYZn) hcp, $P\bar{3}m1$ a = 0.32 nm c = 0.78 nm $(0001)_\alpha$ plate	→ γ ($Mg_{12}YZn$) ordered hcp, 14H a = 1.11 nm c = 3.65 nm $(0001)_\alpha$ plate		
Mg-Y-Ag-Zn	SSSS	→ G.P. zones monolayer $(0001)_\alpha$ disc	→ γ'' ordered hcp, $P\bar{6}2m$ a = 0.56 nm c = 0.45 nm $(0001)_\alpha$ plate	→ γ' hcp, $P\bar{3}m1$ a = 0.32 nm c = 0.78 nm $(0001)_\alpha$ plate	→ γ+δ γ: ordered hcp, 14H a = 1.11 nm c = 3.65 nm $(0001)_\alpha$ plate	δ: fcc, $Fd\bar{3}m$ a = 1.59 nm

§ precipitation process is not well studied; * d is separation distance of columns of RE atoms; # low Gd:Zn weight ratio and low Gd content

2.2.1 β’’’ precipitate

Recent research shows the β’’’ and β’ precipitates in Mg-RE precipitation sequence is the combination of Nd hexagonal rings and zigzag chains [28] as shown in Fig. 2.10. The composition is hence dependent on the combination from hexagonal Mg_3Nd ring to the whole zigzag Mg_7Nd chains.

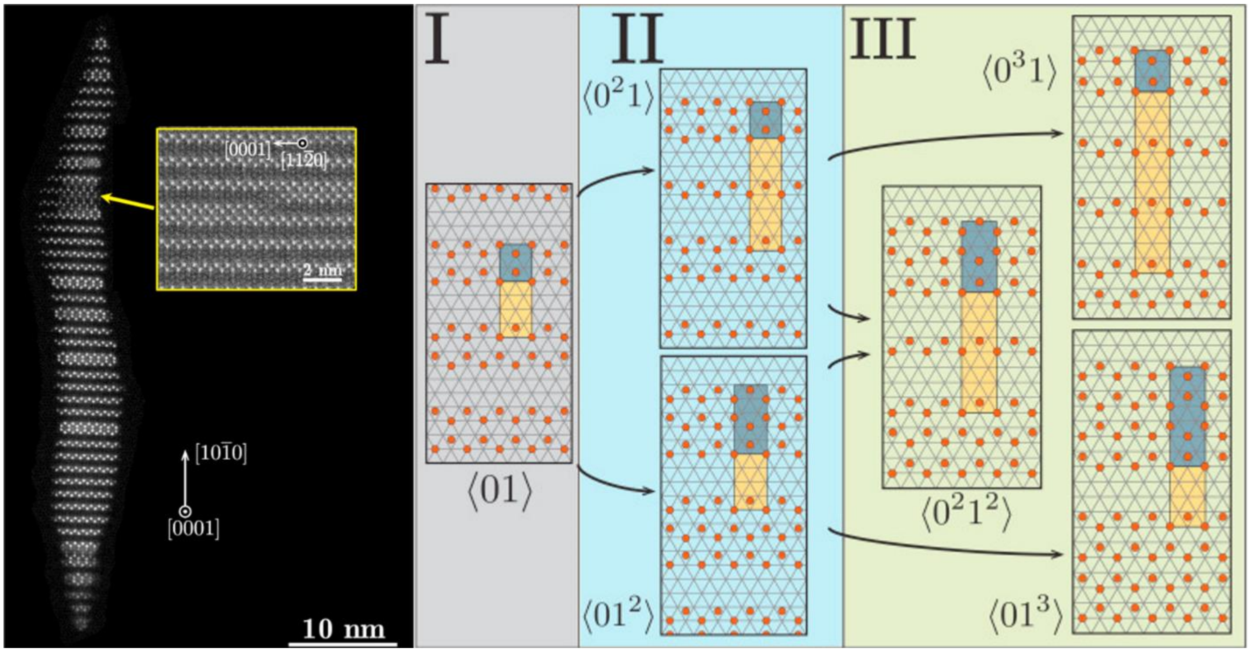

Fig. 2. 10 The HAADF-STEM image of β''' phase in Mg-Nd alloy viewed from [0001] direction. The schematic illustrates the structure of β''' phase is the combination of hexagonal ring (denoted 0) and zigzag chain (denoted 1).

Essentially, regardless of the combination of hexagonal rings and zigzag chains, β''' precipitate formed by replacing certain Mg atoms positions with Nd atoms. The final structure therefore is on the same hcp lattice as the magnesium matrix and therefore amenable to dislocation shearing due to the continuous slip systems. Fig. 2.11 shows the β''' precipitate sheared by basal dislocation by suggesting the shift along basal plane [67].

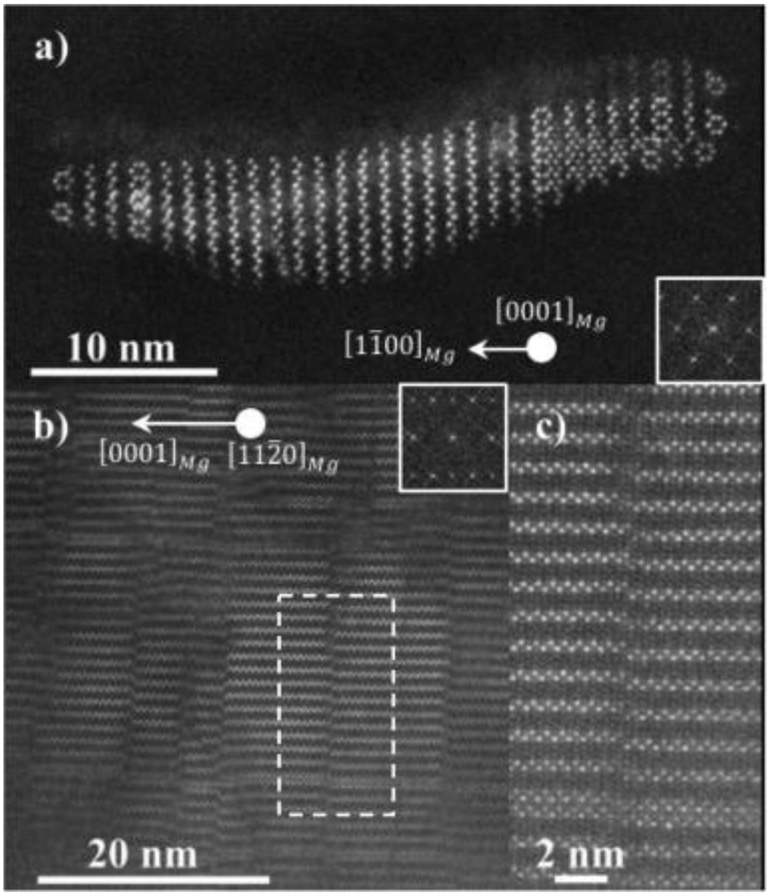

Fig. 2. 11 HAADF-STEM images of β''' precipitate morphology change after deformation. The microstructural shift on basal plane indicates basal dislocation shearing.

2.2.2 β_1 precipitate

Prolonged aging will transform β''' to another metastable phase β_1 [29]. The β_1 precipitate has an orientation relationship to the matrix as $(-112)_{\beta1}//(10\text{-}10)_{Mg}$ and $[110]_{\beta1}//[0001]_{Mg}$. As shown in Fig. 2.12, because of the HCP structure symmetry, β_1 precipitates can form as triad with broad facets lying on (10-10) plane. Taking consideration of precipitate twinning for each triad precipitate, there are a total of 6 variants for β_1 precipitate [30]. The HRTEM image in Fig. 2.12 c) shows the β_1 precipitate, in contrast to β''' precipitate, has a different microstructure to the matrix. Systematical convergent beam electron diffraction (CBED) resolves the β_1 precipitate to be an f.c.c. structure with a space group Fm3m (a=0.74nm), which is also referred as $D0_3$ ordered structure. The composition is determined to be Mg_3Nd [30].

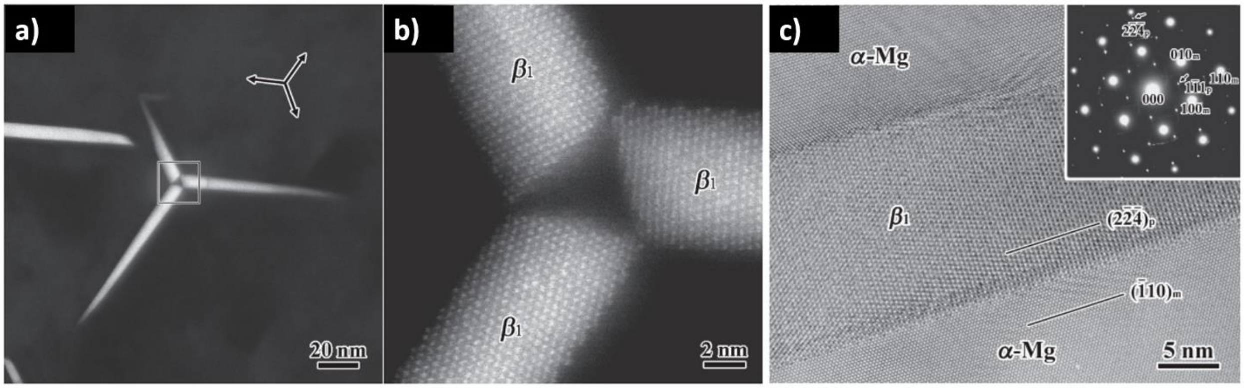

Fig. 2. 12 HAADF-STEM images a-b of β_1 precipitate in Mg-Nd alloy. Image b) is the high magnification of image a). The HRTEM image c) shows the orientation relationship between β_1 precipitate and magnesium matrix. The incident beam is parallel to [0001] Mg zone axis.

The $D0_3$ structure β_1 precipitate is reported to be coherent with magnesium matrix but not with slip system. $D0_3$ type of phases in general have <111>{110} slip system which is only aligned with magnesium basal slip system 1/3<1-210>{0001} on one specific slip system. Additionally, the Burgers vector magnitude between β_1 precipitates and magnesium matrix is different as well. This crystal structure discontinuity leads to a popular belief that the β_1 precipitate is impenetrable. However, recent research [31] reveals the β_1 precipitate is able to be sheared by basal dislocation as shown in Fig. 2.13. The precipitates show shift along basal plane, suggesting a basal dislocation shearing trace. It is interesting to see the shift doesn’t show a clear offset as usually observed in classic precipitate shearing. Furthermore, the precipitates are seemingly rotated in the matrix as shown in Fig. 2.13 c). These abnormal phenomena are not able to be explained in the classic shearing manner as reviewed in the next section.

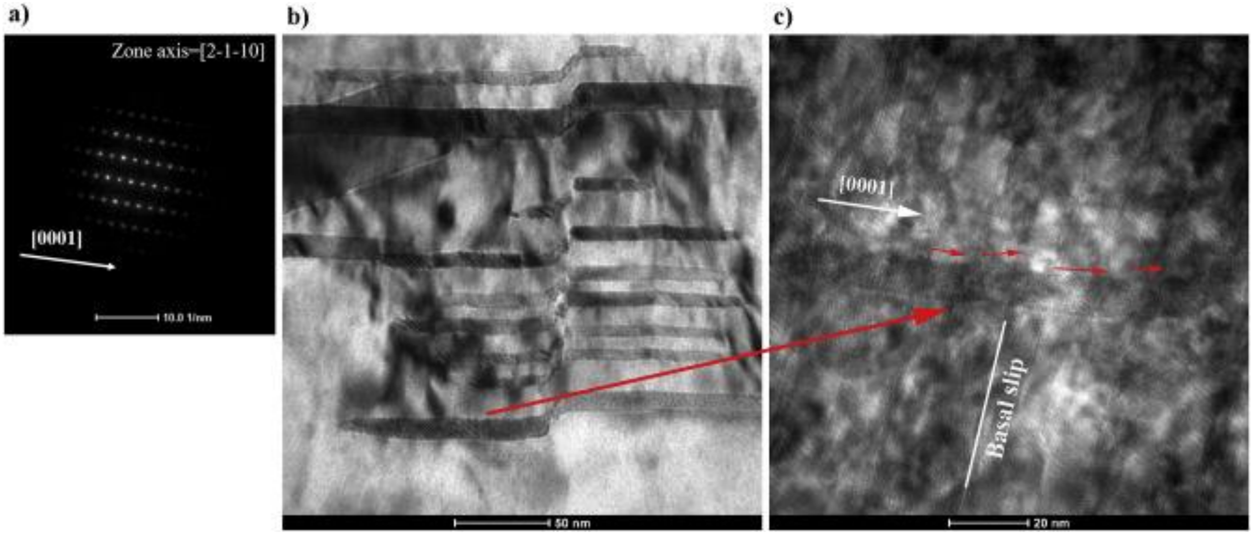

Fig. 2. 13 Basal dislocation shear through β_1 precipitate in MN11 alloys. The incident beam is parallel to [1-210] [31].

2.3 Dislocation-Precipitate Interactions Mechanisms

The dislocation-precipitate interactions can be generally categorized as precipitate shearing and precipitate bypassing. The specific mechanism depends on the precipitate-matrix coherency, precipitate structure, volume fraction and precipitate shape. Among shearing mechanism, precipitation shearing in ordered structure is of particular interests because both β''' and β_1 precipitates are ordered structure. Two precipitate bypassing mechanisms, Orowan looping and the Hirsch model are reviewed in the following section.

2.3.1 Precipitation shearing

For fine, coherent precipitates (largest dimension around 20nm), such as β''' (Fig. 2.10), dislocations are able to shear through the precipitate along a continuous slip system. For large coherent precipitate (largest dimension around 300nm), it is also possible for dislocation to cut through via dislocation accumulation [31]. Generally, the required shear stress to cut through a particle can be approximated by

$$\tau_c \approx \frac{\pi f \gamma_s}{b} \qquad (2.3)$$

where f is volume fraction of precipitate and γ_s is the precipitate-matrix interface energy and b is the dislocation Burgers vector [32].

For ordered structure, the precipitate-matrix interface is replaced by half of the antiphase boundary energy (APBE) because the shearing process involve creation of antiphase in the ordered precipitate as shown in Fig. 2.14. Because of the creation of antiphase boundary, the APB will attract the second the dislocation to reverse to the original structure. Therefore, dislocations often travel in pairs in ordered structure.

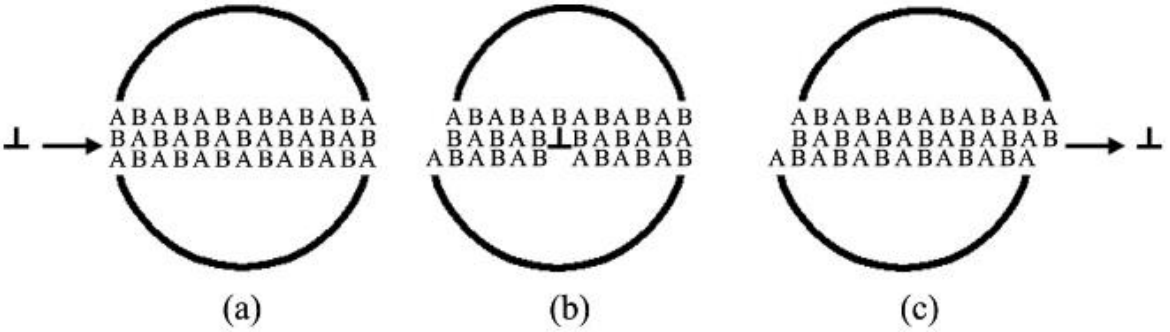

Fig. 2. 14 Schematic of the process that dislocation shearing through ordered precipitate. a) shows the perfect ordered structure prior to the shearing. b) is the intermediate state when the dislocation cut through the precipitate and leave antiphase boundary behind. The sheared structure in c) shows a full antiphase boundary along the entire slip plane.

For some ordered structure such as $D0_3$, a pair of dislocations are not enough to reverse the structure. The structure has been characterized to have <111>{110}slip system. A unit of four dislocation is observed in Fe_3Al $D0_3$ phase [33]. The structure is reversed after two <111> translational vector and can be completed by four ¼ <111> displacement vector. The four-fold dissociation in $D0_3$ structure has been characterized as

$$2 < 111 > \rightarrow 4 \times \frac{1}{2} < 111 > \qquad (2.4)$$

2.3.2 Orowan looping

Orowan looping is widely acknowledged as an important mechanism that describes the interaction between dislocations and impenetrable precipitates [34]. It essentially describes that dislocations bypass the particles by bowing around and leave a dislocation loop around the particle. As shown in Fig. 2.15, the process can be interpreted from dislocation line tension perspective [35].

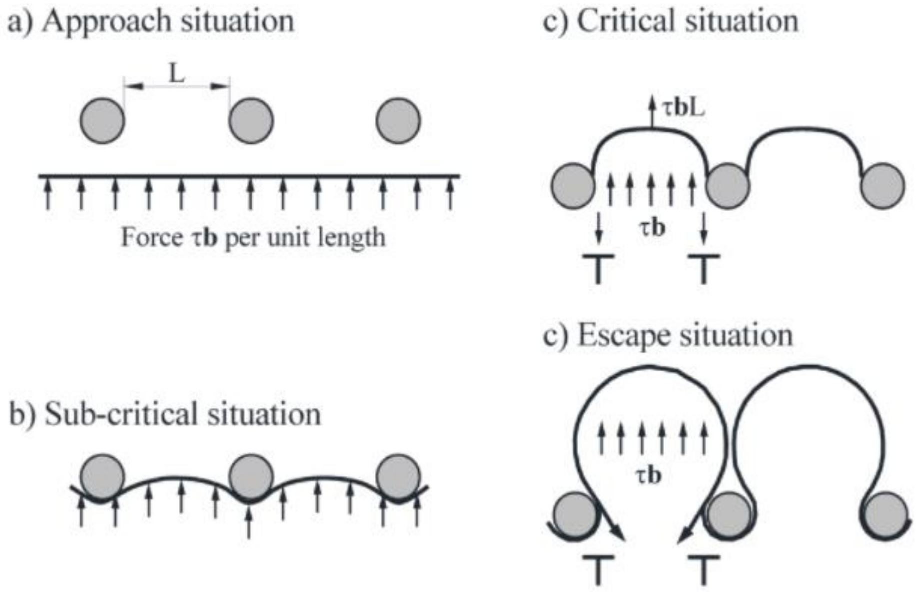

Fig. 2. 15 Schematic of Orowan looping. The critical situation can be estimated as dislocation bowing to semicircle shape in c) [35].

In constant line tension model, the force is constant along dislocation line regardless of its dislocation characteristic such as screw or edge. The Peach-Koehler stress along dislocation depends on the radius of bowing shape as governed by

$$\tau = \frac{T}{bR} = \frac{Gb}{2R} \qquad (2.3)$$

where T is the line tension along dislocation and can be estimated as $Gb^2/2$, R is the radius of curvature and G is shear modulus. Obviously, the force reaches its maximum when R comes to its minimum value L/2 where L is the interparticle spacing between precipitate. The image c) in Fig. 2.15 shows that the maximum stress (Gb/L) is reached when the dislocation adopts a semicircle shape.

The increase in CRSS from precipitation hardening τ_{Orowan}, can be estimated by the Orowan mechanism as well [36, 37]. The equation is given as

$$\tau_{Orowan} = \frac{Gb}{2\pi\lambda\sqrt{1-v}} ln\frac{d_p}{r_0} \qquad (2.4)$$

where λ is the inter-particle spacing in the slip plane, d_p and r_0 are outer and inner cut-off radii for calculation of dislocation energy, G is shear modulus of the matrix phase, b is the magnitude of the Burgers vector, and υ is Poisson's ratio.

The equation 2.4 takes consideration of dislocation characteristic on line tension energy and takes the mean value$\sqrt{1 \times (1-v)}$ (1 accounts for screw dislocations and $(1-v)$ accounts for screw dislocations) to represent the average value of a mixed dislocation. The inner cut-off radii r_0 is the smallest scale where elasticity theory still applies, which is usually taken as one Burgers vector. However, the value of outer radii is of more controversy. The classic Orowan looping theory describes the precipitate as a small spherical particle, while practical alloy like Al-Cu alloy and Mg-RE alloys have precipitates of finite size which are non-spherical and non-equiaxed. A self-stress effect will rise as the finite size of precipitate and depends on specific interaction configuration. The self-stress comes from dislocation-dislocation interaction between the curving components when the dislocation is bowed by precipitates. Certain modification is conduct on correcting the issue [38]. The computational results suggest the outer cut-off radii is related to the precipitate distribution and shape. For example, a rectangular shape precipitate as shown in Fig. 2.16, the outer cut-off radii can be estimated as $\sqrt{WL}$ where W is the width and L is the length of the precipitate.

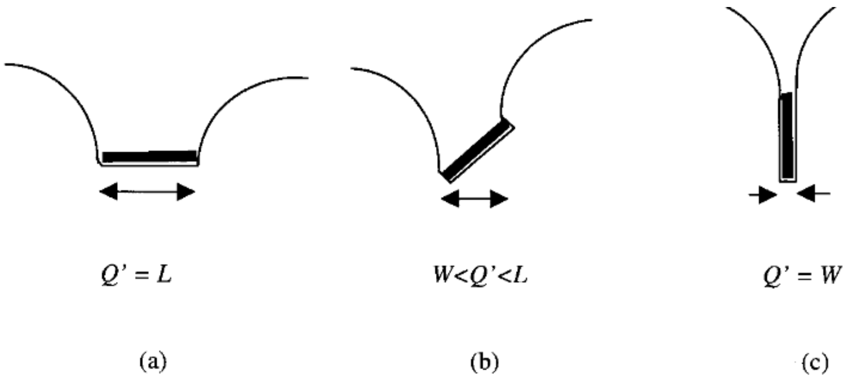

Fig. 2. 16 Schematic illustration of outer cut-off radii variation at different geometrical interactions

The finite size of precipitate not only introduces the self-stress effect but also complicates the value of interparticle spacing. Modification has been employed in aluminum and magnesium alloys [39, 40]. The modification utilizes a mathematical approach which takes account the shape effect on reducing interparticle spacing. For example, Fig. 2.17 shows the spacing between prismatic precipitate plates. The new effective interparticle spacing λ can be calculated from geometrical relationship reflecting the efficiency of different precipitate shapes. The corresponding Orowan equation can be modified by inserting the effective interparticle spacing into equation 2.4.

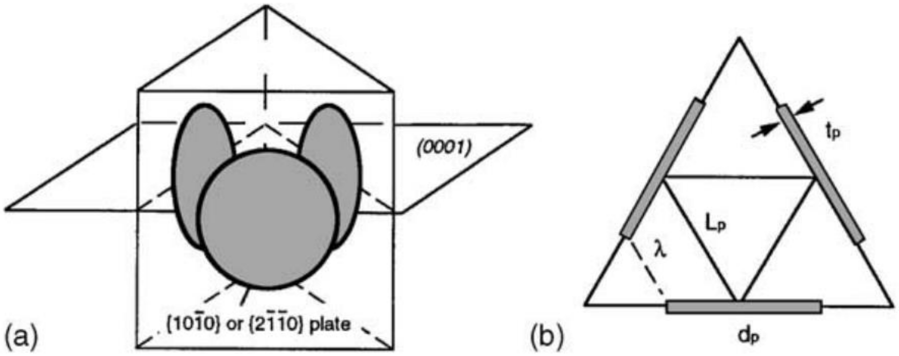

Fig. 2. 17 The triangular arranged plate shape precipitate on reducing effective interparticle spacing λ [40].

After including shape effect factor, the results render the prismatic plate is the most effective morphology to reduce the interparticle spacing for the same precipitate volume fraction, as shown in Fig. 2.18. It also suggests the aspect ratio is as important as the precipitate shape, providing an insight on precipitate design.

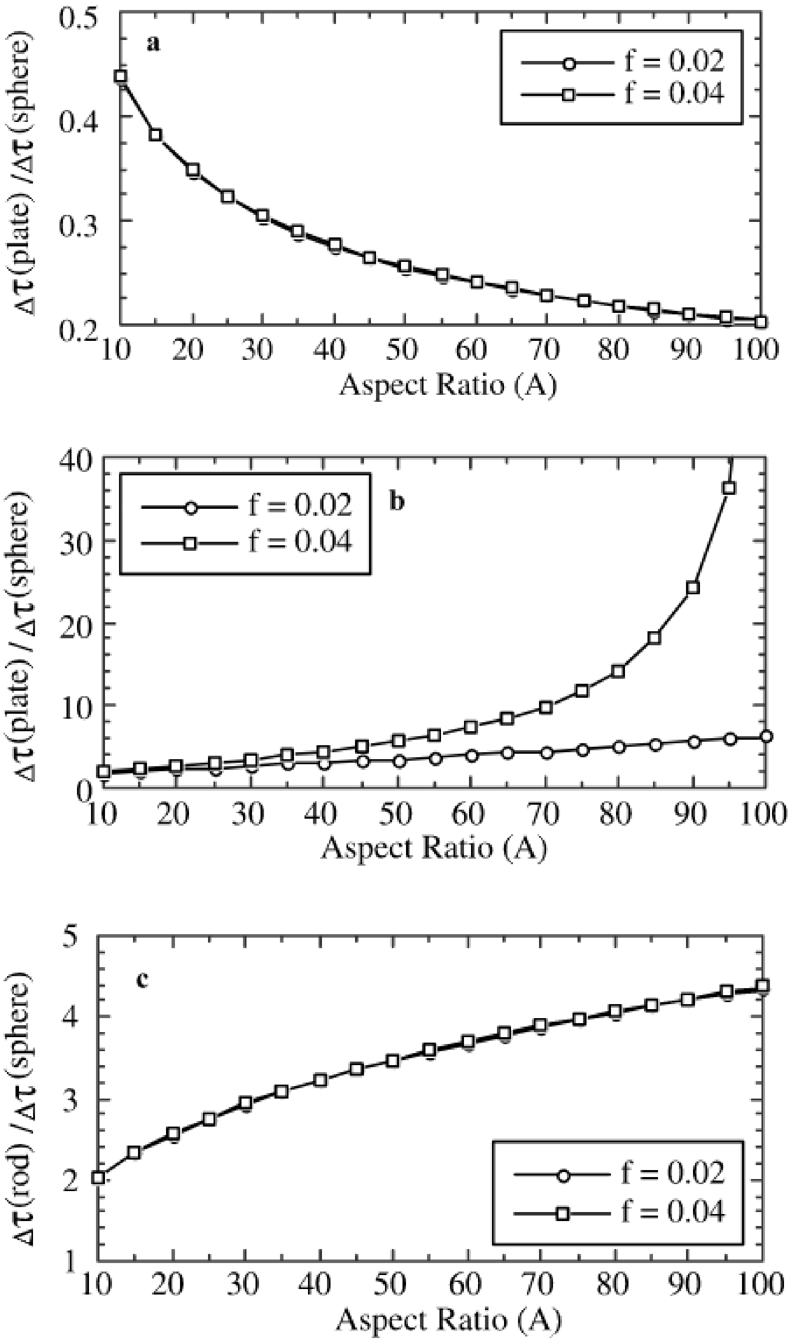

Fig. 2. 18 The variation of ratio between different precipitate morphology and spherical shape. a) is the basal plate, b) is the prismatic plate and c) is the c axis rod.

An important aspect in the Orowan mechanism is the loop that the bypassed dislocation leaves behind. The loop is sometimes visible around the precipitate in TEM images as shown in

Fig. 2.19 [42]. Existing Orowan loop will serve as an immobile dislocation to repel like sign following dislocations on the same glide plane, which leads to further strain hardening

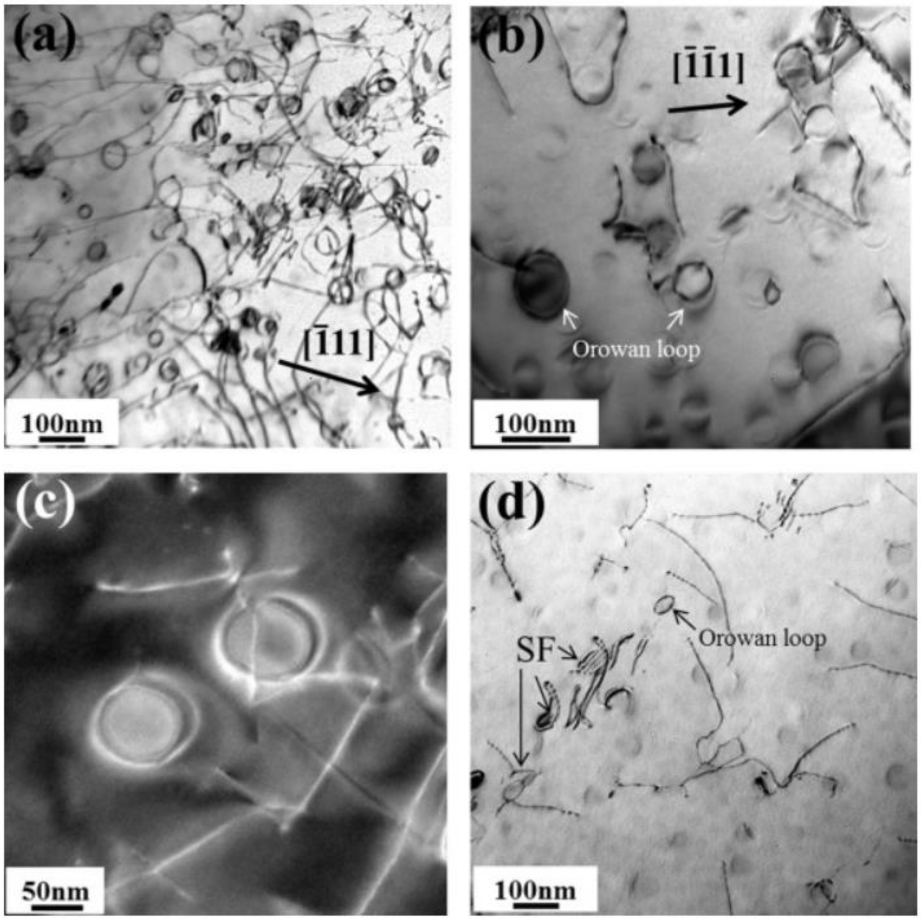

Fig. 2. 19 Orowan loop observation in TEM. Samples taken from Ni-Fe-based superalloy after creep rupture 750oC/150MPa [42].

However, the interface dislocation is known to be able to relax at precipitate interface in order to lower the line tension energy. The relaxation degree depends on interface geometry and atomic structure [41]. Recent MD simulation shows the interface dislocation can be absorbed at γ precipitate $Mg_{17}Al_{12}$ [43]. The interface dislocation relaxation has important consequence in the following hardening since it changes the dislocation line tension energy and stress field.

2.3.3 Hirsch Mechanism

The Orowan looping mechanism successfully demonstrates the interaction between dislocation and impenetrable particle. However, the successive looping mechanism theoretically will cause the strain hardening to be unrealistically high. Hirsch [68, 69] proposed a mechanism to address this issue. The major modification from the Hirsch mechanism is to include a cross-slip mechanism during the interaction. The trademark of this mechanism is forming a superjog via cross slip, but it is resistant to further forward motion and results in a prismatic loop. As shown in Fig. 2.20, dislocations cross slip two-three times to overcome the blocking precipitate and leave a prismatic loop behind. The Orowan loop in Fig. 2.20 a) can also be induced to cross slip and react to moving dislocations, resulting in another prismatic loop as shown in Fig. 2.20 d).

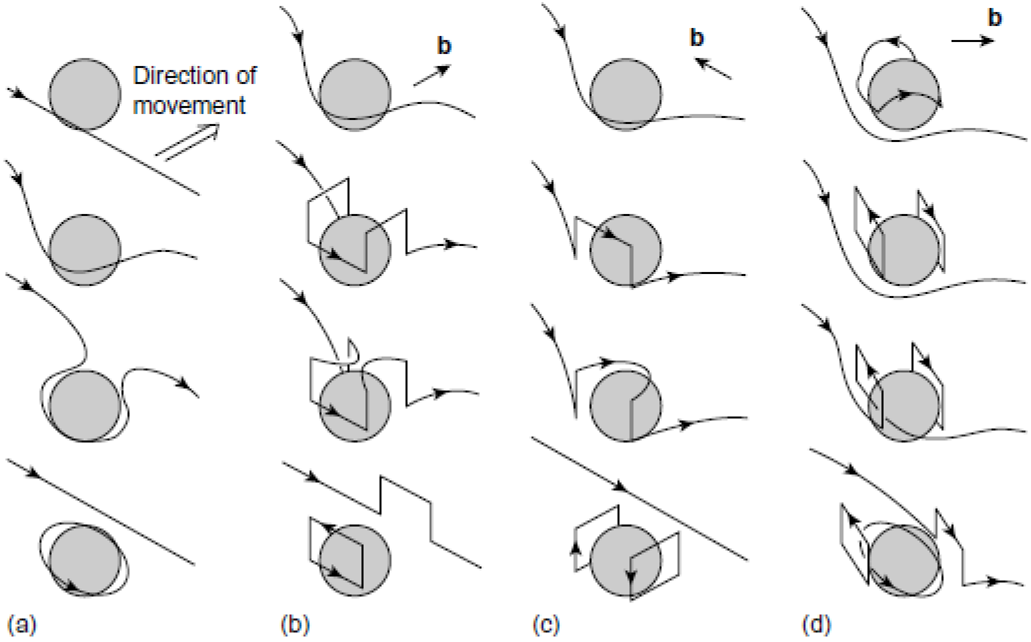

Fig. 2. 20 The schematic illustration of Hirsch mechanism. Orowan looping is shown in a) and Hirsch mechanism of different dislocation Burgers vector is exhibited in b)-d).

CHAPTER 3

Experimental and Computational Approach

This chapter describes the research methods used in the thesis work. The author conducted the computational work in collaboration with Prof. Liang Qi and his student Chaoming Yang. The major experimental approach for the thesis is transmission electron microscopy (TEM) especially *in situ* indentation.

3.1 Sample Preparation

Mg-2.4wt. %Nd extruded bar and casting billet was obtained from CanmetMATERIALS, Canada. The bar was extruded from the 85 mm cast billet to a final diameter of 15 mm at 300 ^oC at a speed of 254 mm/min. The cast billet was solution heat treated at 530^oC for 3 hours prior to the extrusion. The final extruded bar was sectioned, and the sections were reheated to 530^oC for 1 hour for homogenization, followed by water quenching. Metallographic specimens were prepared from homogenized sections. Texture and grain size information was characterized from electron back-scattered diffraction (EBSD) in a TESCAN MIRA3 scanning electron microscope (SEM). Aging heat treatment was performed to both extruded bar and casting billet at 250 °C to different times to acquire different precipitate structures. Finally, standard tensile samples with 1-inch gauge length were machined to quantify the tensile behavior. These samples were tested using a hydraulic (MTS) test machine at an initial strain rate of 10^{-4} /s. A total of six heat treatment conditions were investigated: solution heat treated (SHT), plus aging at 250 °C for 30 minutes, 2 hours, 6 hours, 9 hours, and 100 hours. Casting billet was machined to standard compression sample and test at a strain rate of 10^{-4}/s to a total compressive strain of 3% and 5%.

For post mortem study, TEM foils were prepared from the compression samples and the gauge section of bulk tensile test which had been pulled to failure. All foils were taken 5 mm away from fracture surface and in a uniform deformation region. Samples for *in situ* indentation in TEM were prepared from solutionized casting alloys and aged for 30 mins and 9 hours to test samples with β′′′ and β_1 precipitates, respectively. Samples were mechanically polished to 100 μm and electropolished in a twin-jet polisher following a procedure provided by Nie and Muddle [30]. High-resolution TEM imaging was conducted in a double aberration-corrected JEOL 3100R05 TEM operated at 300kV, whereas diffraction contrast dislocation analysis was conducted in a JEOL 2010F TEM. *In situ* straining samples were preferentially electropolished at the sample edges to produce electron transparent regions for contact with the indentation tip. A Hysitron PI95 TEM PicoIndenter was used for this experiment. A detail of the setup is described in the next section.

3.2 *In situ* Straining in Transmission Electron Microscope

The electropolished sample was glued by silver paste to the stage of a Hysitron PI95 TEM Picoindenter leaving the transparent region facing the 1μm flat punch indenter tip. Fig. 3.1 schematically shows the *in situ* straining setup. Local deformation is introduced by indentation at a displacement rate of 1 nm/s and dislocation activity was recorded by a Gatan OneView camera at a frame rate of 12 frames/second. Since the area of the TEM foil deformed by the indenter tip is small with respect to the grain size, the deformed region can be regarded as a part of a single crystal. Most of the selected foils have an orientation near basal plane and some near to $(\bar{1}2\bar{1}3)$ plane. Experiments are conducted in a JEOL 2010F transmission electron microscope.

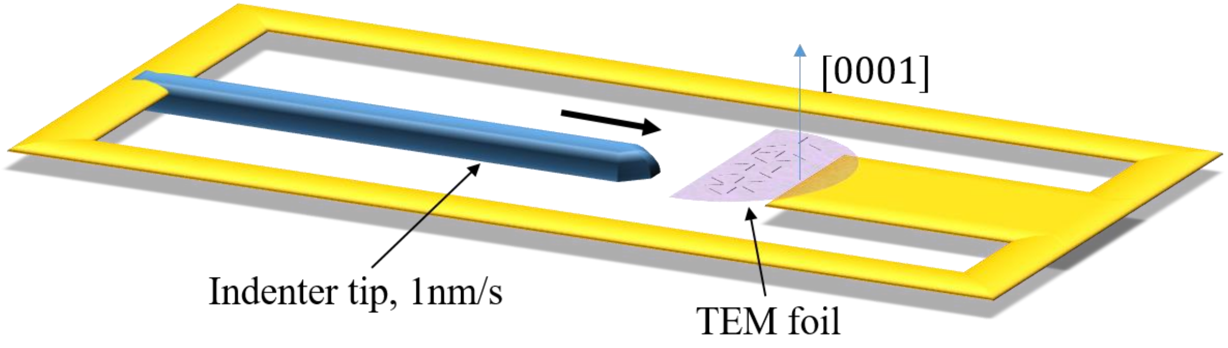

Fig. 3. 1 Schematic of the TEM in situ indentation setup. The TEM foil in this figure is selected with its normal (blue arrow) closely parallel to [0001]. Black dashes in foil represent precipitates of three different variants. The indentation direction is indicated by thick black arrow.

3.3 Molecular Dynamic and First Principle Simulation Setup

MD simulations were performed based on a modified embedded-atom method (MEAM) interatomic potential of Mg-Y alloys [44]. The Mg-Y MEAM potential was used as a surrogate material system due to the lack of accurate Mg-Nd potentials. Two simulation boxes were set-up as shown in Fig. 3.2, one for the study of an edge dislocation interacting with the precipitate and one for a screw dislocation interacting with the precipitates. As shown in the Fig. 3.2, the bases of the simulation box for the screw dislocation case are X $\parallel [\bar{1}2\bar{1}0]$, Y $\parallel$ [0001], Z $\parallel [\bar{1}010]$ with the size along each dimension as 46.36, 41.90 and 33.14 nm, respectively. The bases of the edge dislocation setup are oriented as X $\parallel [\bar{1}010]$, Y $\parallel$ [0001], Z $\parallel [\bar{1}2\bar{1}0]$, and the simulation box has dimensions of 47.87 × 46.53 × 33.20 nm. Both simulation setups contain ~2.9 million atoms.

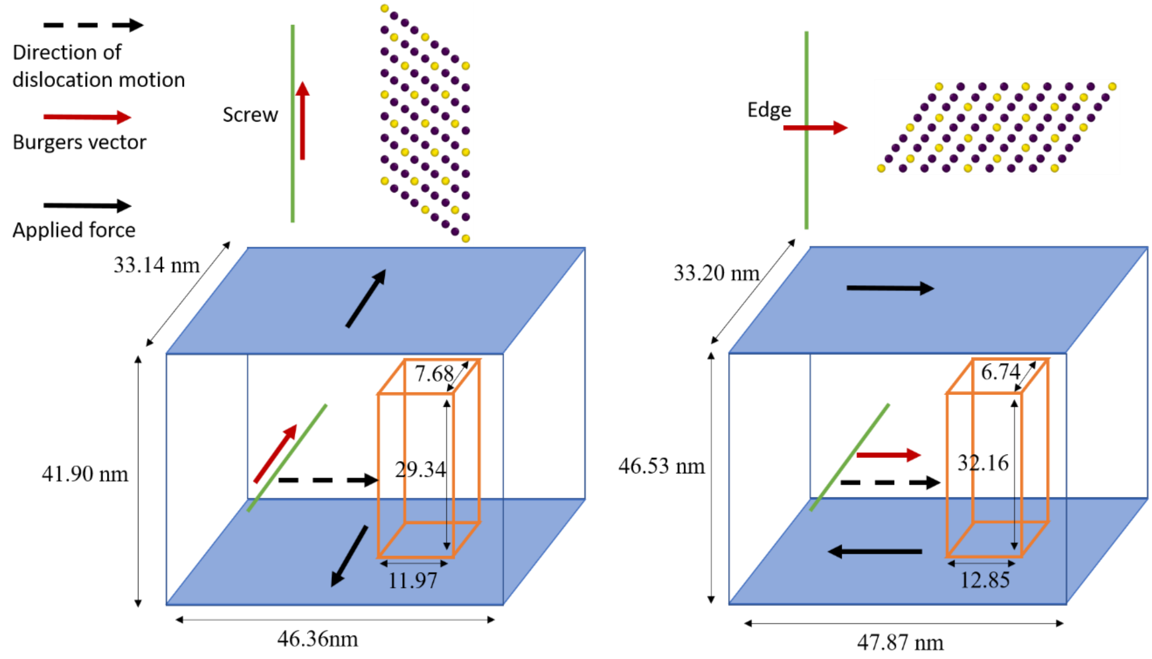

Fig. 3. 2 MD simulation setup for analysis of interaction of screw and edge dislocation with a β1 precipitate (shown as an orange cuboid).

Periodic boundary conditions were applied along X and Z directions and cut the Y directions to make free surfaces which were used to apply traction forces. A periodic array of dislocations was introduced in the perfect HCP lattice based on Stroh's formula [45], and applied methods described by Bacon [46] to maintain the periodicity along the X-Z plane after introducing dislocations. To simulate a precipitate in our system, a cuboid was cut out from the box and replaced with the same shape and oriented D0$_3$ Mg$_3$Y to satisfy the orientation relationship $[\bar{1}11]_{\beta_1}//[11\bar{2}0]_{\mathrm{Mg}}$ and $(110)_{\beta_1}//(0001)_{\mathrm{Mg}}$. The size of the cuboid is 12.85 × 32.16 × 6.74 nm in the edge setup and 11.97 × 29.34 × 7.68 nm in our screw setup. The precipitate size is selected to be consistent with the inter-precipitate spacing but not necessarily the precipitate aspect ratio since it is believed the latter has less influence on the mechanism manifestation.

The MD simulation started by an isothermal-isobaric (NPT) upon time integration on Nose-Hoover style to allow the system to reach pressure equilibrium at 300K. Once the system reached equilibrium at 300K, the canonical (NVT) ensemble was applied on the system. The driving shear stress was applied through surface traction by adding a constant force on the top and bottom surface at each time step. According to the Peach-Koehler equation, for the screw, the forces were applied along the Z direction; and for the edge, forces were applied along the X direction, as shown in Fig 3. The magnitude of applied forces F_{app} per atom were calculated as:

$$F_{app} = \sigma_{shear} * A_{xz}/N_{surf} \qquad (3.1)$$

where σ_{shear} is the shear stress component that drives dislocations to move, A_{xz} is the surface area of x-z plane, and N_{surf} is the number of atoms on the surface. Our MD simulations were performed in a timestep of 1 fs. The constant shear stress applied on the simulation box corresponding to the applied constant force was 200 MPa.

The DFT calculations were performed using the Vienna *Ab initio* Simulation Package (VASP) [47] based on the PAW-PBE pseudopotentials [48, 49]. The calculation supercell size was 5.25 Å × 7.41 Å × 114.37 Å, containing with 108 Mg atoms and 36 Nd atoms and 20 Å vacuum along z direction. The supercell axes were x ∥ [-110], y ∥ [001], and z ∥ [110] in Cartesian coordinates. 13 × 9 × 1 k points were sampled by the Monkhorst-Pack method and used 350 eV as the cutoff energy for the plane wave basis set. Due to crystal symmetry, antiphase boundaries (APB) were introduced by shifting half of the supercell along ¼ [11-1] and ½ [11-1] vector on (110) plane in Mg_3Nd precipitates. VASP was used to calculate the energies of the supercell before and after introducing the APB, respectively. Ionic relaxation was performed to all atoms by conjugate gradient algorithm until the total energy converges to $1e^{-4}$ eV. The APB energy was obtained by the total energy difference divided by the x-y plane area of the supercells.

CHAPTER 4

Interaction of Glide Dislocations with Extended Precipitates

4.1 Introduction

As described in Chapter 2, for many magnesium alloys, precipitation hardening is an important mechanism for impeding dislocations on the basal glide planes. In particular, precipitates that are aligned parallel to the prism planes, so-called prismatic precipitates, have been shown to be effective in pinning basal dislocations [50, 40]. Commercial alloys such as WE54, WE43 and Mg-RE (RE represents rare earth element) utilize the prismatic β_1 precipitate as a strengthening phase [51, 52, 53]. The β_1 phase has an ordered structure $D0_3$ (space group $Fm\overline{3}m$, a_{β_1}=0.74nm) with a composition of Mg_3RE [54], and is generally regarded as non-shearable by basal slip in Mg matrix [55]. The strengthening of such non-shearable precipitates are dominated by Orowan looping.

For these extended non-spherical and non-equiaxed precipitates, as reviewed in Chapter 2, certain modifications have been taken on original Orowan equation. However, most of these modifications are mainly correcting some parameters in the equation such as interparticle spacing and outer cut-off radii. The dynamic interaction process for non-equiaxed precipitates attracts little attention, while it is of great importance to understand the dynamic process for dislocation-precipitate interactions simulation like MD and DD. Additionally, it is scientifically important to find any new interaction mechanisms for different precipitate shapes.

In this Chapter, the author utilizes *in situ* straining in TEM to characterize the interaction between basal dislocations and β_1 precipitates. The results are rationalized by dislocation-theory based model.

4.2 Results

Two scenarios are presented in this section viewing the precipitate-dislocation interactions, respectively, from $<0001>$ and $<\bar{1}2\bar{1}3>$ orientations. The β_1 precipitates have a lath morphology and are parallel to the $(10\bar{1}0)$ habit plane. The orientation relationship between β_1 precipitates and matrix is $[10\bar{1}0]_m \parallel [\bar{1}12]_p$ and $(0001)_m \parallel (110)_p$. The precipitates have a high aspect ratio and are approximately 200 nm along both length $[\bar{1}2\bar{1}0]$ and height $[0001]$ dimensions but only 10 nm in thickness. In the studied aging condition (9 hours at 250°C), the β_1 precipitates in the over-aged sample are prone to be semi-coherent. In order to have the best contrast, both bright field and dark field diffraction conditions were used. For the (0001) view plane, dark field imaging was used and dislocations appear as bright lines in section 4.2.1 whereas for the $(\bar{1}2\bar{1}3)$ view plane, bright field imaging was used and dislocations appear as dark lines in section 4.2.2. The *in situ* experiments were supplemented with post mortem analysis that indicated that the predominant slip systems were <a> Burgers vectors on basal planes, that is also the slip system reported to have the lowest CRSS in magnesium [56]. Bowed dislocations also tend to elongate along the Burgers vector to increase the screw component to minimize its energy, resulting in an elliptical shape such as the bowed segment (marked as 2) in Fig. 4.1 d).

4.2.1 Dislocations glide along interface

Figure 4.1 shows the behavior of a single dislocation interacting with an extended β_1 precipitate. The glide dislocation is observed to be pinned and then eventually bypass the precipitates. The selected area is tilted to be near to the basal plane. The studied dislocation segment is marked with an arrow in Fig. 4.1 a). With increasing stress during the indentation process, the initial dislocation starts to glide and reaches a new pinned configuration in Fig. 4.1 b).

The pinned dislocation segment in Fig. 4.1 b) has been divided into part 1 and 2. It is noticeable that part 1 starts to glide (from Fig. 4.1 b) to c)) by moving the right end on the precipitate facet. Fig. 4.2 shows the corresponding schematic view of the observed dislocation-precipitate interactions. In Fig. 4.2 a) to b), the pinned segments 1 and 2 continue bowing as stress increases to a point when the right end of segment 1 moves along the precipitate interface. The dashed dotted line in Fig. 4.2 b) portrays an intermediate position of segment 1 between 9.05s and 9.09s in the *in situ* experiment. In this study, we define the dislocation configuration at the onset of interfacial glide as the critical condition. In order to maintain the continuity of the dislocation, the glide along the interface is expected to create extra dislocations line length at the interface, which are represented as red dash lines in Fig. 4.2. Once the interface glide initiates, the mobility of the free end to glide along precipitate interface is significantly higher than the bowing process leading to a fast transition from one pinned configuration to another one. In considering Fig. 4.1 and 4.2, it should be noted that interfacial glide does not occur simultaneously for segments 1 and 2. Although the pinned segments 1 and 2 are formed from one single original dislocation, the bowing and interfacial glide behavior are independent from each other. This justifies that the pinned dislocation behavior depends on the segment between two pinned points rather than the whole dislocation, which is one of the basic assumptions in the following model.

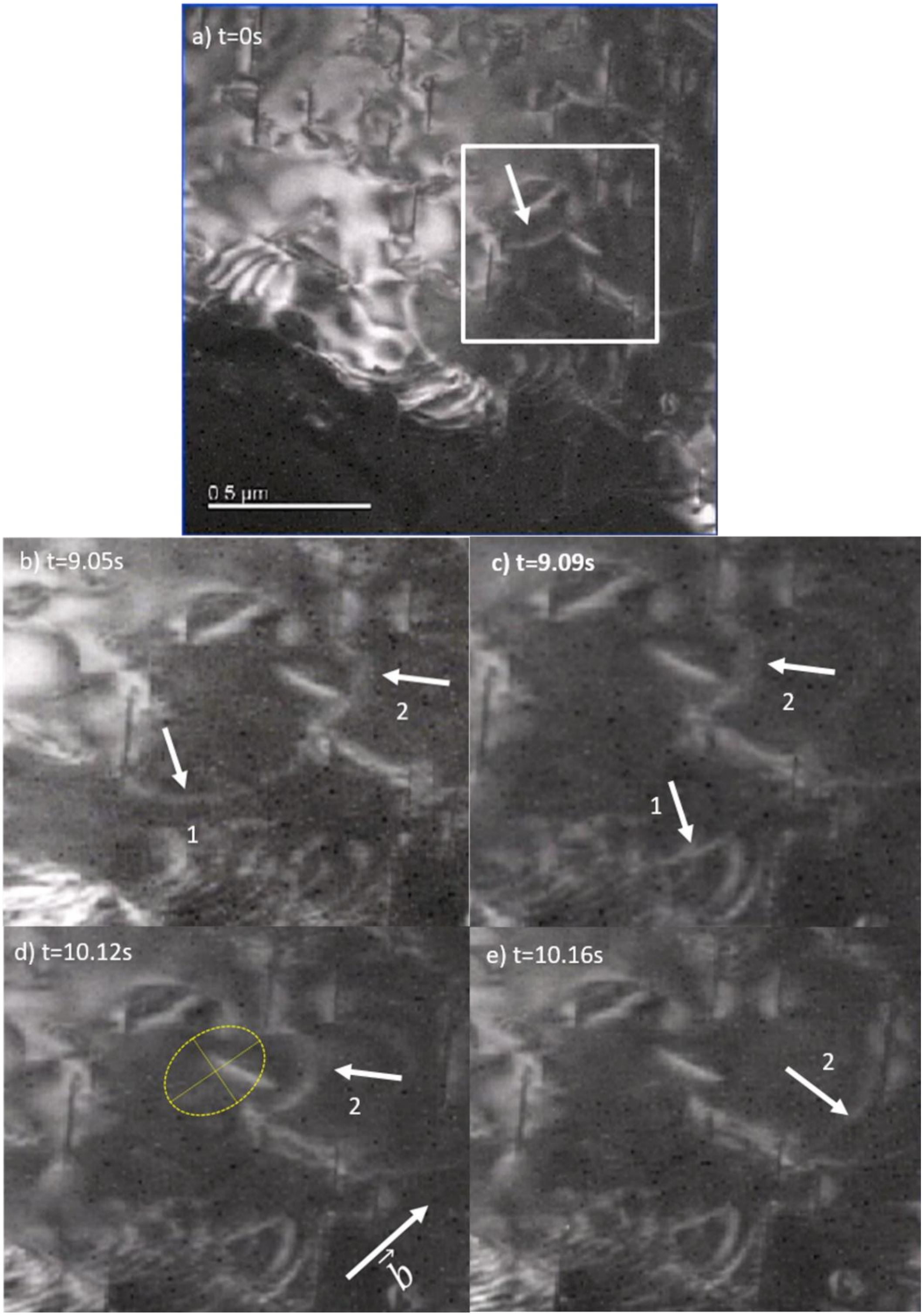

Fig. 4. 1 TEM images of dislocation glide on the basal plane. The region in Fig. 4.1 b, c, d,e are from the marked region in Fig. 4.1a. The time interval between b) and c), d) and e) is very short (one frame

0.04s) recording the dislocation propagation for both segments. Frame d) shows an elliptical shape of the bowed dislocation segment 2.

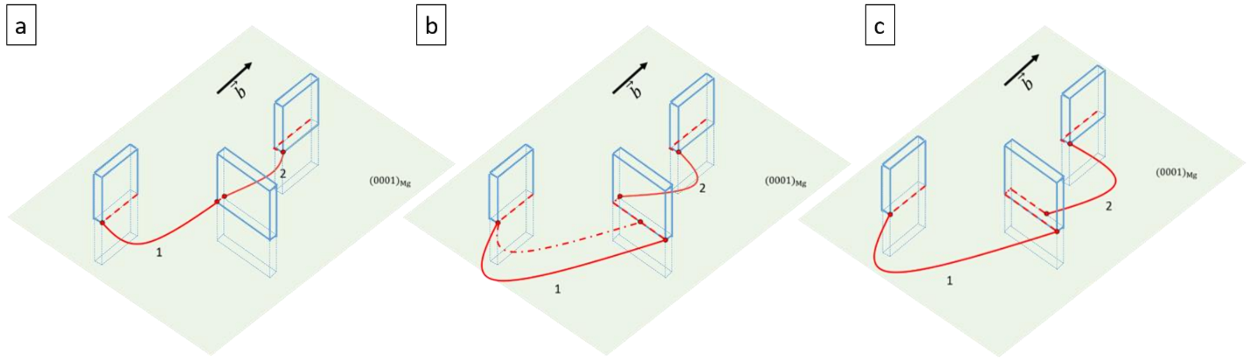

Fig. 4. 2 Schematics of precipitate-dislocation interactions depicting progression of the experimental images shown in Fig.4.1. β_1 precipitates are oriented perpendicular to the basal plane depicted as plates with broad facets. Dislocations are constrained in the basal plane and the interfacial dislocations are represented by red dashed lines.

<u>4.2.2 Orientation-dependent effect</u>

In Figure 4.3, a foil region is examined that is oriented near to $(\bar{1}2\bar{1}3)$. Thus the foil plane lies 30^{o} from the basal axis so that the precipitates are observed in a slant view. In section 4.2.1, dislocations initially interact with the narrow edge of the β_1 precipitate, followed by the formation of interfacial dislocations as the dislocation glides parallel to the broad facets of the precipitates. In the *in situ* video, these interactions happen with the broad facets and display the different dislocation behaviors. Figure 4.3 shows two different precipitate-dislocation configurations at the same time. Two pinned dislocations are studied in this case: 1) A dislocation (marked as 1) is observed to glide from the left bottom of the image and makes contact with the broad facet of the precipitates. 2) A dislocation (marked as 2) is observed to be pinned at the narrow edge of the precipitate near the left top of the image. In general, the two segments do not have to be in the same basal slip plane but in the schematic, are shown in the same plane for convenience. In Fig. 4.3 a), a purple dotted line is used as a reference to connect the two pinned nodes and mark the orientation of the initial dislocation line. The main difference between the two pinned segments is the angle between the initial dislocation line direction and the broad precipitate facet. We define this angle as orientation angle. For segment 2, its initial dislocation line is about 30^o away to the precipitate long axis, whereas the initial dislocation line of segment 1 is nearly parallel to it.

Segment 2 in Fig. 4.3 behaves similar to the dislocation in Fig. 1 in that it bows against the narrow edge and initiates interfacial glide when it reaches the critical condition. As in Fig. 4.3 c), after interfacial glide occurs at precipitates interfaces, segment 2 is pinned at the departure side. Without strong bowing, segment 2 is able to glide out of view at Fig. 4.3 d), which indicates a weak detachment force. In contrast, the behavior of segment 1 is completely different. As shown in Fig. 4.3 a), the segment 1 first approaches the broad interface of the precipitate and creates an interfacial dislocation marked as red dashed line in the schematics. Then, it gets pinned as depicted in Fig. 4.3 b). When it continues to glide, it bows around two pinned nodes in Fig. 4.3 c) and creates interfacial dislocations at precipitate interfaces as the dotted lines represent in Fig. 4.3 d). Comparing these two segments, from Fig. 4.3 a) to c), both segments are bowed from the pinned nodes but segment 2 is able to glide at precipitate interface, whereas no interfacial glide occurs on segment 1 after it is pinned at the position depicted in Fig. 4.3 d).

The *in situ* experiment shows two different bowing configurations for segments 1 and 2. Segment 1 bows much more than segment 2. Because the back stress exerted from dislocations are related to the bowing shape, the difference in bowing shape is deemed to indicate these segments have different pinning stresses. The interfacial glide of segment 2 facilitates its propagation without the need to further increase bowing under the applied stress. There is no fundamental difference between segment 1 and 2 in terms of dislocation characteristics. As mentioned above, it is the precipitate-dislocation configurations that are different, and the occurrence of the proposed interfacial glide mechanism reduces the pinning effect for specific dislocation-precipitate geometries. In this video, precipitates with lower orientation angles appear to exhibit a stronger pinning effect than those with larger angles.

In summary, the different bowing configurations between these two segments gives an indication that the strengthening effect for single precipitate-dislocation interaction depends on the relative precipitate-dislocation orientation.

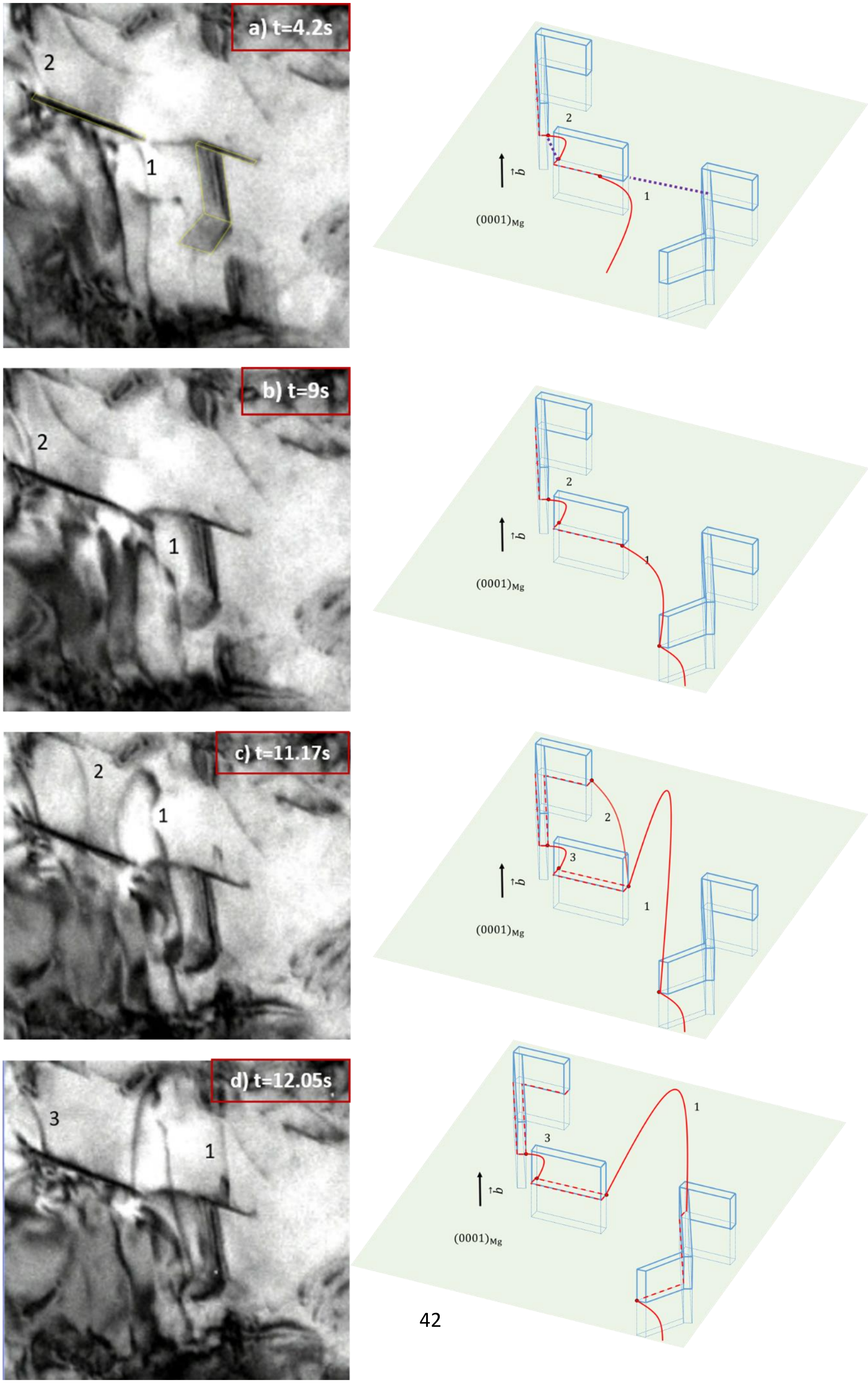
a) t=4.2s
2
1
b) t=9s
2
1
c) t=11.17s
2
1
d) t=12.05s
3
1
$\vec{b}$
$(0001)_{Mg}$
2
1
3

Fig. 4. 3 TEM images of motion of dislocations on basal $(\mathbf{0001})$ plane thread through two parallel precipitates. Schematics in the right column correspond to the recorded frame at left. The viewing direction$[\bar{\mathbf{1}}\mathbf{2}\bar{\mathbf{1}}\mathbf{3}]$ of images relative to schematics is shown in schematic a). The precipitates of interest are also outlined in a). Initial dislocation line direction is represented as purple dotted line in a). After segment 2 glides out of view, a following dislocation segment 3 is pinned in c) and d).

4.3 Discussion

In the *in situ* straining experiment, we have observed interfacial glide at broad facet of linear extended β_1 precipitates. Unlike the classical bowing mechanism in which the dislocation encircles the precipitate completely to form a loop, interfacial glide can create dislocations at interfaces without extensive bowing. For a given precipitate-dislocation configuration, Fig. 4.4 shows the difference between the two mechanisms. In both situations, dislocations are pinned at the tip of precipitates. However, after reaching the critical condition, interfacial glide is initiated in Fig. 4.4 a) showing a different sequence that occurs creating interfacial dislocations compared with the classical bowing shown in Fig. 4.4 b). The conditions that favor the unit process shown in 4 a) over 4 b) are analyzed below based on dislocation theory.

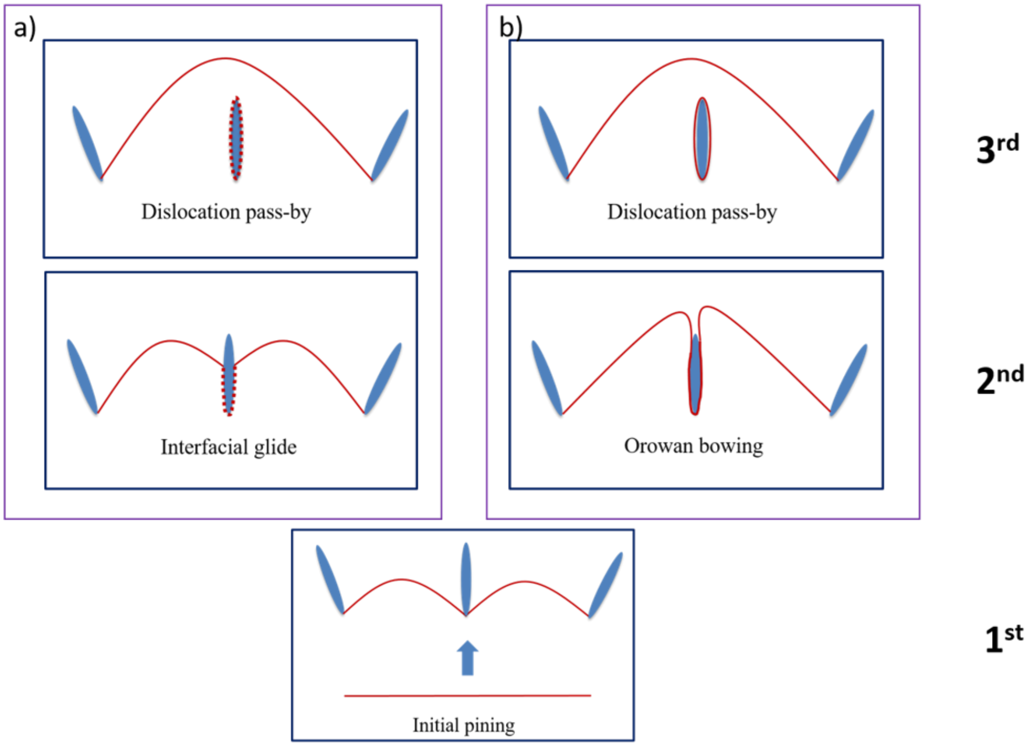

Fig. 4. 4 Schematic diagram of a) proposed interfacial glide mechanism and b) classical bowing mechanism for overcoming the given precipitate configuration. The dotted line around the center precipitate is the interfacial dislocation created by forward dislocations. Solid lines represent the initial position, critical condition, intermediate position and final position from bottom to top.

4.3.1 Dislocation Theory Analysis

In order to comprehend this phenomenon, a model based on dislocation line tension is developed, as shown schematically as in Fig. 4.5.

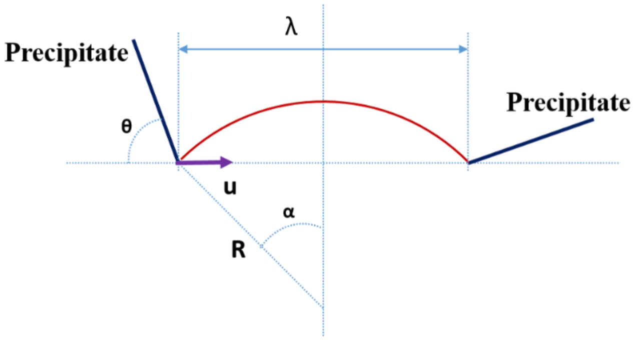

Fig. 4. 5 Dislocation-precipitate geometry for a pinned dislocation segment. The arrow indicates, as a reference, the initial unbowed dislocation line direction (u). For the precipitate on the left, the

orientation angle θ is defined as measured clockwise from u to the trace of the broad facet of the precipitates. For the precipitate on the right, it is defined as measured counter clockwise.

In this model, we assume that given the different θ values for the two pinning points, the initiation of glide along the interface may be favored for one point over the other. It has to be mentioned that this is a generic scenario where dislocation get pinned by two extended precipitates. No preferred orientation between precipitates is presumed in the model, although it will be 60^o or 120^o angle between different β_1 precipitate variants. The analysis is thus applicable for general configuration.

Once the dislocation begins to glide along the interface, it will lose the force equilibrium until it reaches another pinned position, normally the departure side of the precipitate.

For the sake of mathematical simplicity, the bowed segment is treated as an arc with a radius of R. Angle α is the half of central angle for the bowed segment. For a given inter-particle spacing λ, a larger value of α shows a stronger bowing segment. We define $x = \sin(\alpha^*) = \frac{\lambda}{2R}$ as the bowing magnitude, ranging from 0 to 1, related to the strength of the pinning point, where α^* represents a critical value of α.

Fig. 4.6 shows two possible configurations of the pinned dislocation, Fig. 4.6 a) for the case of no glide along interface and Fig. 4.6 b) for the case of dislocation glide along interface.

E_1 is the dislocation energy at the critical condition. If there is no interfacial glide, Fig. 4.6 a), the pinned dislocation will continue bowing to a new position with an energy of E_2. The area swept by dislocation bowing is S_1 and is related to the plastic work done. On the other hand, if interfacial glide occurs, Fig. 4.6 b), a small interfacial dislocation segment is created with an energy of E_i and the new curved dislocation has an energy of E_3. The area swept by dislocation movement is S2. From an energy point of view, interfacial glide can initiate only if the energy of the second configuration, Fig. 4.6 b), is lower than the first one, Fig. 4.6 a). Therefore, the energetic criterion to favor interfacial glide is as follows:

$$E_3 + E_i - \tau b S_2 < E_2 - \tau b S_1 \tag{4.1}$$

where τ is the Peach-Koehler stress. If the bowed dislocation is in force equilibrium at the critical condition, the external stress is equal to the back stress calculated from the dislocation.

$$\tau = \frac{T}{bR} = \frac{Gb}{2R} \tag{4.2}$$

where T is the line tension which is approximately $\frac{Gb^2}{2}$ using a constant line tension model.

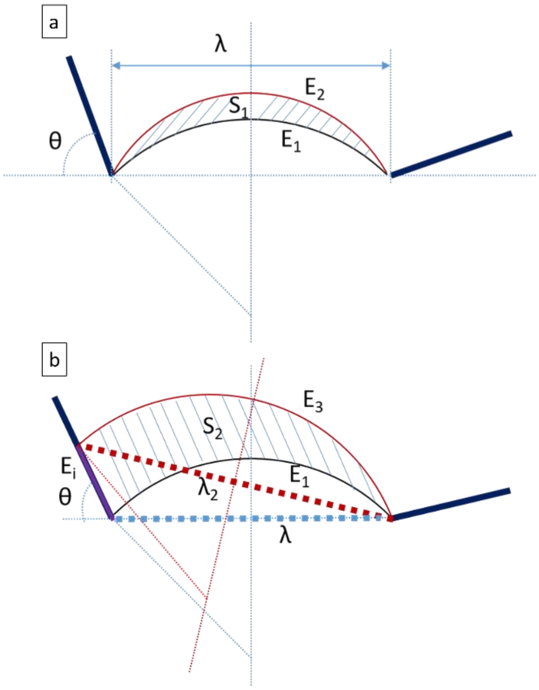

Fig. 4. 6 Schematic of two dislocation bowed shapes due to different energy configurations: a) bowing without interfacial glide and b) interfacial glide from the critical condition. The interfacial dislocation in b) is represented by the purple line. This infinite small interfacial dislocation segment is exaggerated in the schematic for viewing purpose. The heavy dotted lines highlight the distance between pinned points.

Since the bowed shape is assumed to be an arc, i.e., it is insensitive to the Burgers vector direction, a constant line tension model is applied so that the dislocation line energy is only dependent on dislocation length. Then the energy of E_1 can be expressed as:

$$E_1 = \frac{Gb^2}{2}(2R\arcsin\frac{\lambda}{2R}) \tag{4.3}$$

After an incremental interfacial glide, as in Fig. 4.6 b), it is assumed that the new curved dislocation glides along the precipitate broad facet with no change in curvature, which gives its energy E_3:

$$E_3 = \frac{Gb^2}{2}(2R\arcsin\frac{\lambda_2}{2R}) \tag{4.4}$$

It should be noticed that λ_2 is larger than λ so that the length of the new curved dislocation is longer than the dislocation when it is in the critical condition. This leads to an increase in the energy δE.

The energy criteria can be revised as:

$$\delta E + E_i + \tau b(S_1 - S_2) < E_2 - E_1 \tag{4.5}$$

The evolution from E_1 to E_2 is because of a change in the radius of curvature. Since the change is infinitesimal, the criterion becomes:

$$\delta E + E_i + \tau b(S_1 - S_2) < dE \tag{4.6}$$

The right side of equation (4.6) is a derivative of equation (4.3) with regard to radius R. Its expression is given as:

$$dE = \frac{Gb^2}{2}\left(\frac{2\frac{\lambda}{2R}}{\sqrt{1-\left(\frac{\lambda}{2R}\right)^2}} - 2\arcsin\frac{\lambda}{2R}\right)dR \tag{4.7}$$

To solve δE,

$$\delta E = E_3 - E_1$$

$$\delta E = \frac{Gb^2}{2} * 2R(arcsin\frac{\lambda_2}{2R} - arcsin\frac{\lambda}{2R}) \qquad (4.8)$$

Because the difference between λ_2 and λ is infinitesimally small, the value of the expression in parentheses in equation (4.8) can be solved by Taylor expansion. Expanding arcsinx on x=$\frac{\lambda}{2R}$ yields

$$arcsinx = \arcsin\left(\frac{\lambda}{2R}\right) + \frac{1}{\sqrt{1-\left(\frac{\lambda}{2R}\right)^2}}\left(x - \frac{\lambda}{2R}\right) + o(x - \frac{\lambda}{2R})^2 \qquad (4.9)$$

The last term of this polynomial is a higher order term that can be ignored in the following derivation. Utilizing the approximation in equation (4.9) and setting x= $arcsin\frac{\lambda_2}{2R}$, the equation (4.8) can be approximately written as

$$\delta E = E_3 - E_1 = \frac{Gb^2}{2}\frac{1}{\sqrt{1-\left(\frac{\lambda}{2R}\right)^2}}(\lambda_2 - \lambda) \qquad (4.10)$$

λ_2 can be expressed as

$$\lambda_2 = \sqrt{(\lambda + dlcos\theta)^2 + (dlsin\theta)^2}$$

$$\lambda_2 = \sqrt{\lambda^2 + 2\lambda dlcos\theta + dl^2} \qquad (4.11)$$

where dl is the length of interfacial dislocation, which is also an infinitesimally small value. Hence λ_2-λ is infinitesimally small. The approximation of that difference is in the same manner as the previous Taylor expansion. The result can be expressed as

$$\lambda_2 - \lambda = \frac{1}{2\lambda}(2\lambda dlcos\theta + dl^2) \qquad (4.12)$$

Ignoring the higher order term dl^2, the final expression for δE is

$$\delta E = E_3 - E_1 = \frac{Gb^2}{2}\frac{1}{\sqrt{1-\left(\frac{\lambda}{2R}\right)^2}}\, dlcos\theta \tag{4.13}$$

To solve S$_1$ and S$_2$, we come up with a function defining the green shaded area in Figure 4.7.

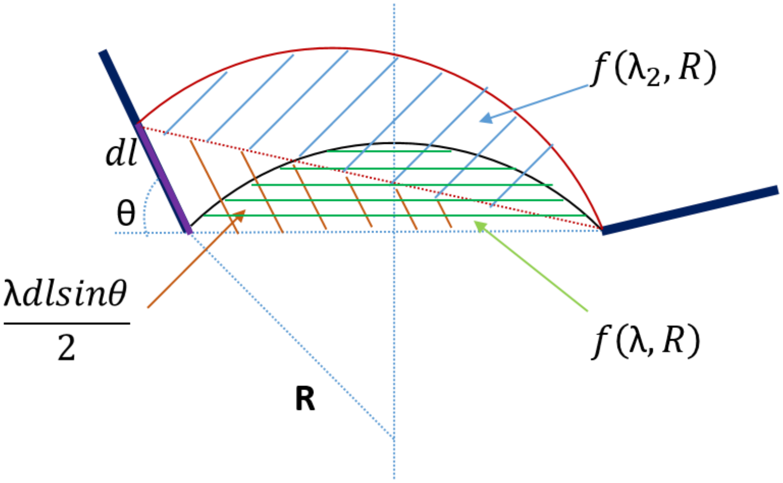

Fig. 4. 7 Schematic shows area of different regions. The green shaded area is the dislocation swept area before interfacial glide is initiated. The sum of orange and blue shaded area is the swept area caused by bowing and interfacial glide.

The function can be expressed as

$$S = f(\lambda, R) = R^2 \arcsin\left(\frac{\lambda}{2R}\right) - \frac{\lambda}{2}\sqrt{R^2 - \left(\frac{\lambda}{2}\right)^2} \tag{4.14}$$

The expression for S$_1$ is basically the derivative of $f(\lambda, R)$ with respect to radius R.

$$S_1 = \frac{\partial f}{\partial R}(-dR) = \left(-\frac{2\lambda R}{\sqrt{4R^2-\lambda^2}} + 2Rarcsin\left(\frac{\lambda}{2R}\right)\right)(\text{-dR}) \tag{4.15}$$

Mathematically dR is defined as the difference between radii of E$_2$ and E$_1$, which is negative for this bowing configuration. Hence, the negative sign for dR is to ensure a positive value of dR.

It takes more effort to acquire S_2 since it involves three shaded areas in Figure 4.7. S_2 can be calculated as the sum of blue and orange shaded area after subtracting the area marked in green.

$$S_2 = f(\lambda_2, R) + \frac{\lambda dl sin\theta}{2} - f(\lambda, R) \tag{4.16}$$

A similar approximation method is used to solve $f(\lambda_2, R) - f(\lambda, R)$. The result is given as

$$S_2 = (\frac{R}{\sqrt{4-\frac{\lambda^2}{R^2}}} - \frac{2R^2-\lambda^2}{2\lambda\sqrt{4R^2-\lambda^2}}) dl cos\theta + \frac{\lambda dl sin\theta}{2} \tag{4.17}$$

Up to this point, most of the terms in the energy criteria equation (4.6) are solved except for the interfacial dislocation energy, E_i. Results from earlier studies suggest that the energy of interfacial dislocations is lower than that in the matrix [41]. The line energy at the particle interface is given as:

$$E_i = \frac{Gb^2}{2} \mathrm{K} dl \tag{4.18}$$

where K is the relaxation parameter which is related to the interface property such as coherency and atomic bonding strength. The value of K ranges from 0 (interfacial dislocations have no energy) to 1 (no interfacial dislocation relaxation). We will use this equation to study how dislocation line energy at interfaces affects interfacial glide.

Inserting all the terms into the energy criteria (4.6) and simplifying, results in the following equation:

$$\mathrm{K} - sin\theta x + \sqrt{1-x^2} cos\theta < 0 \tag{4.19}$$

It should be noted that equation (4.19) is valid for θ from 0 to 180° even though the schematic in Fig. 6 and 7 only shows θ smaller than 90°.

4.3.2 Model Application

For any given precipitate-dislocation configuration, Equation (4.19) can be used to predict whether or not interfacial glide is energetically favorable. For example, if the pinning precipitates are perpendicular to initial dislocation line direction, then θ is set equal to 90º. For this geometry, equation (4.19) yields the energy criteria that are required to satisfy $К < x$. If interfacial glide can occur, equation (4.19) must solve a value of x within the range from 0 to 1. In the situation above, if no interfacial dislocation relaxation exists in this interface (К=1), there is no resolved x from equation (4.19) meaning no interfacial glide is allowed. In fact, for К=1, for any given value of θ we input into equation (4.19), there is no solution for x. In conclusion, the energy criteria suggest that the root cause of interfacial glide is the existence of interfacial dislocation relaxation.

For any К<1, interfacial glide may be activated but not for any given precipitate-dislocation configuration. Solving the equation (4.19) under different constraints can provide results below. The mathematical derivation is omitted.

1. When К<1, interfacial glide is not allowed if orientation θ is smaller than

$$\theta^* = arccos\sqrt{1 - К^2} \tag{4.20}$$

2. When К <1 and θ^*<θ, interfacial glide happens when

$$x = К sin\theta + \sqrt{1 - К^2} cos\theta \tag{4.21}$$

3. When К <1 and θ>90º, the left side of equation (4.19) is always smaller than zero if θ is larger than

$$\theta^{**} = \pi - arccos К \tag{4.22}$$

Case 1 indicates a threshold value for initiation of interfacial glide. It also implies an orientation-dependent effect. If the precipitate has orientation factor θ smaller than θ^*, no interfacial glide is allowed meaning the bowing magnitude of pinned dislocation can reach to 1. Recall that equation (4.2) can be written in terms of the bowing magnitude x to reflect the maximum back stress when dislocation reaches the critical condition.

$$\tau = \frac{Gb}{2R} = \frac{Gb}{\lambda} x$$

$$\tau = \frac{Gb}{\lambda}(\mathrm{K} sin\theta + \sqrt{1-\mathrm{K}^2} cos\theta) \tag{4.23}$$

From Case 2, the resultant stress calculated for the critical condition is a function of the orientation factor θ. It follows that the stress τ is monotonically decreasing with θ when it ranges from θ^* to θ^{**}. The function of equation (4.23) is plotted in Figure 8. This explains the experimental result in section 4.2.2 where dislocations are bowed strongly for segment 1 and no interfacial glide is allowed to initiate whereas for segment 2, it is easy for interfacial glide to occur. Because of the different precipitate-dislocation configurations for the two segments, the one with smaller precipitate orientation angle is more difficult or even impossible to initiate interfacial glide and this is the case for segment 1. Although it is not possible to measure the external stress from the *in situ* video, the shape of bowed dislocation can be used to infer the level of stress acting on dislocation. The stronger bowing shape of segment 1 indicates a higher back stress against the external stress, which supports the hypothesis that interfacial glide is sensitive to precipitate orientation and may have an influence on the overall precipitation hardening. In addition, Case 3 provides an interesting situation in which the dislocation segment will spontaneously glide along the interface because the energy criteria is automatically satisfied when θ is larger than θ^{**}. This may explain the result in section 4.2.2 where the initial incoming dislocation segment 1 directly deposits interfacial dislocations on the first precipitate interfaces. However, this mechanism is only accountable for pinning at front end. After the interfacial glide, the dislocations will get anchored at departure end and thus the strengthening also depends on the detachment process. The pinning effect from departure side is unsolved. For example, dislocation segment 1 in Fig. 4.1 receive strong pinning from left end resulting a strong bowing shape whereas the segment 2 in Fig. 3 easily glide out of view from departure side without severe bowing. The overall precipitation strengthening is determined by the higher pinning effect from front and departure end. The detachment process is discussed in the Chapter 5.

As indicated, interface relaxation parameter Κ is of great significance in determining if interfacial glide is to be expected. Equation (4.19) provides a method for determining the interface relaxation parameter Κ. The value of Κ can be determined if the orientation angle θ is measured from *in situ* experiments and the bowing magnitude is extracted from critical condition. However, practically, the bowing magnitude is difficult to measure precisely due to the image quality and strain field around dislocations and precipitates. A shape fitting method is used to increase the measurement accuracy. A circle is matched to the curved segment, hence the half central angle α is measured graphically from the critical condition and the bowing magnitude is determined. In Figure 4.8, three critical conditions are extracted from *in situ* videos. The first one comes from section 4.2.1 and the other two come from another video but all in the same basal view direction. The result is summarized in Table 4.1.

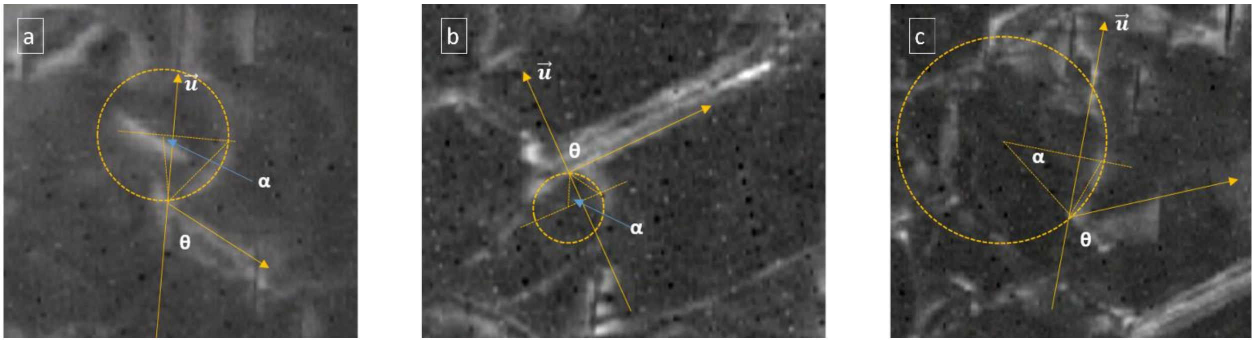

Fig. 4. 8 Method for measuring the half central angle for three critical conditions used to determine the relaxation parameter К. All images are exerted from in situ video recorded in dark field condition with near basal orientations. The yellow arrows show broad facet orientations and the initial dislocation line direction.

	Table 4. 1 Relaxation parameter determination on three different configurations			
	$\theta/^{o}$	$\alpha^{*}/^{o}$	x	К
a)	62	81.9	0.99	0.81
b)	90	64.2	0.90	0.90
c)	113	36.1	0.59	0.86

Although the three critical conditions have different precipitate-dislocation configurations, the calculated relaxation parameters are relatively consistent. The average value of К is 0.86. The relative constant value of К suggests that the interface dislocation relaxation is closely related to interface itself, which is thought to be linked to the interface geometry and atomic structure [41]. Research characterizing this relaxation parameter in other alloy systems [41, 57], especially in oxide dispersion strengthened (ODS) alloys suggests that interface dislocation relaxation affects the creep behavior of those alloys. In the ODS system the reinforcing particles in those alloys are incoherent with matrix. The lower bound for relaxation parameter can be 0.66 for INCONEL MA754 superalloy [57]. The upper bound can reach as high as 0.93 for MA6000 [41]. Although this phenomenon is widely observed, the physical meaning remains unclear. In semi-coherent metallic interfaces [58], dislocation core spreading may lead to interface relaxation. Incoherent or semi-coherent interfaces which have relatively lower shear strength of the interface can ease atomic rearrangement and facilitate local interface diffusion resulting in a lower energy spread dislocation core along the interface plane [59]. The value of К of 0.85 in the present work seems to fall into a reasonable range. Although β_1 precipitates in Mg are generally reported to be coherent

[60], the samples characterized in this study were over-aged and may have resulted in semi-coherent precipitates.

The dislocation energy model in this study successfully explains the theoretical foundation of interfacial glide and shows the orientation-dependent effect. Nevertheless, it should be recognized that many simplifications have been made in deriving this model. In reality, dislocation energy is sensitive to Burgers vector and surrounding dislocations. Calculations related to individual precipitate-dislocation interaction are only suitable for ideal situations. A more accurate study may involve use of dislocation dynamics (DD) simulations. A better understanding of interfacial glide is believed to be important for alloy development. It could be a general mechanism for dislocation interactions with linear extended precipitates. From the analysis of relaxation parameter K, this study suggests that interface engineering may play an important role in determining the strengthening effect due to extended precipitates.

4.4 Conclusions

In situ straining in TEM is performed on over-aged Mg-2.35% *wt*.% Nd binary alloy. The unit process for precipitate-dislocation interaction was observed for extended lath β_1 precipitates. A dislocation based model is developed to analyze the unit process. The key findings from the experimental characterization and theoretical analysis are summarized below.

1. The pinned dislocation may glide along the precipitate broad facet to overcome precipitate blocking, thereby creating interfacial dislocations.
2. An orientation-dependent effect is observed suggesting a stronger pinning effect for precipitates with low orientation angle θ, as defined in Figure 4.6 θ is measured clockwise from dislocation line direction to the trace of the broad facet of the precipitate.

3. Dislocation theory-based analysis shows that the proposed interfacial glide mechanism is energetically favorable if interface dislocation relaxation exists.
4. The model shows that the resultant stress for glide is affected by interfacial glide which is determined by the orientation angle θ and an interface relaxation parameter Κ that ranges from 1 (no glide along the interface implying high resistance to creating interfacial dislocation segments) to 0 (easy glide along the interface, low interface resistance to creating interfacial dislocation segments).
5. A higher value of θ and a lower value of Κ will result in a lower value of the glide stress for single dislocation, and ultimately a reduced level of strengthening from precipitate front end.

CHAPTER 5

Dislocation cross-slip in precipitation hardened Mg-Nd alloys

5.1 Introduction

As reviewed in Chapter 2, non-basal <a> dislocation cross-slip in single crystal Mg has been studied experimentally [2] and computationally [61, 62]. *Couret* and *Caillard* [2] published their *in situ* TEM work on prismatic slip in single crystal Mg showing that the prismatic glide is controlled by thermally activated motion of rectilinear screw component, known as the Friedel-Escaig (F-E) mechanism [3]. According to F-E mechanism (F-E), a cross-slipped basal dislocation is dissociated into two partial dislocations on the basal plane, and glides by thermally activated kink pairs that lie in the cross-slip prismatic plane and move in a direction parallel to the Burgers vector of the screw dislocation. The mechanism is shown in Fig. 2.3.

In general, cross-slip mechanisms relieve local stress concentrations and lead to multiplication of mobile dislocations that is hypothesized to be beneficial for room temperature tensile ductility [18, 17, 24, 23]. The cross-slip mechanism has also been observed in precipitation hardened magnesium alloys. For example, *Clark* [63] observed basal dislocations cross slipped to prismatic plane when they interacted with $Mg_{17}Al_{12}$ precipitate in Mg-9wt.%Al alloy. Recent MD simulation by *Liao et al.* [64] also showed dislocation cross-slip at $Mg_{17}Al_{12}$ precipitate.

In the current study, a Mg-2.4wt.%Nd alloy was heat treated to produce two different kinds of precipitate microstructures β′′′ ($Mg_{3-7}Nd$) and $β_1$ (Mg_3Nd), to investigate dislocation-precipitate interactions. Both these precipitates form as high aspect ratio prismatic plates, lying perpendicular to the basal plane. These two precipitates are typical strengthening phases in the technologically important Mg-RE alloys such as WE43 and WE54 [30]. As mentioned in Chapter 2, the $β_1$ precipitate is considered as strong and non-shearable since its $D0_3$ ordered structure is different from the HCP matrix. On the other hand, β′′′ precipitate possesses an ordered structure on the HCP lattice and is fully coherent with the HCP Mg matrix [65]. Previous study [Huang 2019] showed that it is difficult for single basal dislocations to shear $β_1$ precipitates, whereas recent experimental results show that β′′′ precipitates can be sheared by basal dislocations [66, 67].

5.2 Results

This section is arranged to first describe the macroscopic tensile test to show the different mechanical behavior between β’’’ and $β_1$ precipitate strengthened conditions. A post-mortem study was then conducted to reveal the dislocation behavior after failure for various aging conditions. Finally, *in situ* indentation in TEM was performed to study the difference between dislocation interaction with β’’’ and $β_1$ precipitate, followed by MD simulation to understand the atomic scale mechanisms of the dislocation behavior observed in experiments.

5.2.1 Texture and Tensile Behavior

The texture of a solution heat treated tensile sample is shown in Fig. 5.1 a). More than 200 grains were scanned in EBSD and the result indicates a weak fiber texture, with $(10\bar{1}0)$ parallel to extrusion direction (ED) and (0001) spread to radial direction (RD). The average grain size (area average) is around 165µm from EBSD data. The tensile axis was parallel to the extrusion direction. With the weak fiber texture in the extrusion direction, the tensile axis is about 10-20°

away from the basal plane for most of the grains. The engineering stress-strain curves for 6 different aging conditions are shown in Fig. 5.1 b). The corresponding microstructures are shown in Fig. 5.2. The precipitates present in each condition were identified by selected area diffraction (SAD).

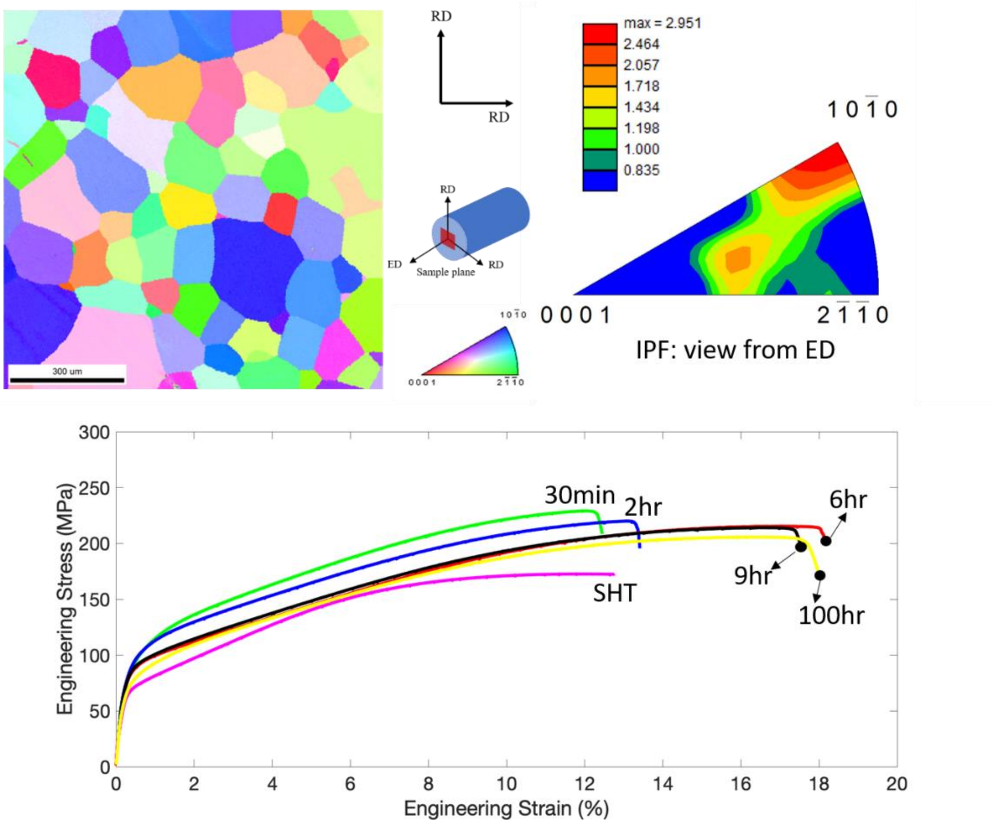

Fig. 5. 1 Weak fiber (viewing from ED direction) texture of SHT sample in a) and engineering stress-strain curve of six aging conditions at 250 °C in b). ED= extrusion direction; RD= radial direction.

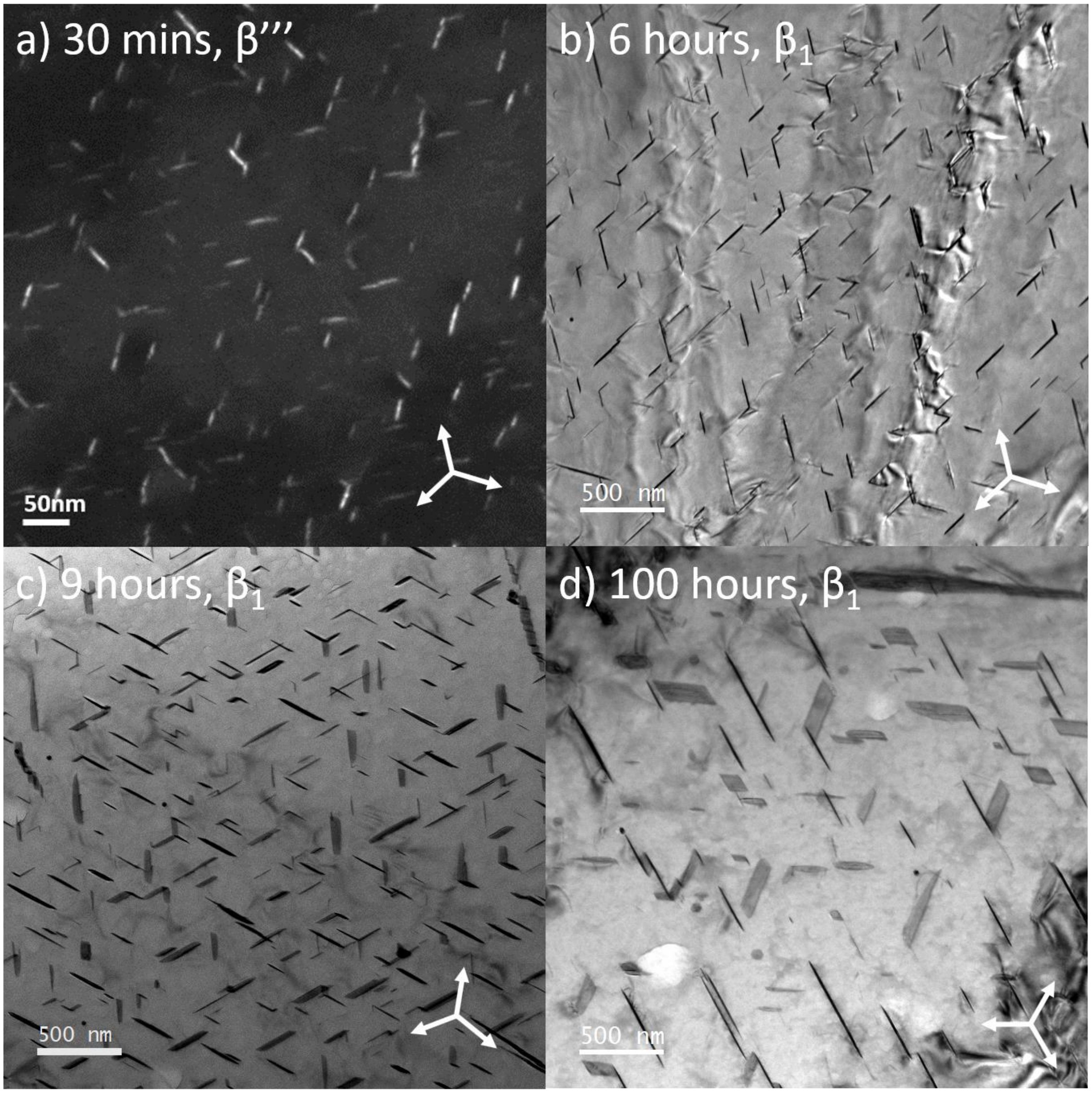

Fig. 5. 2 Dark field image a) and bright field image b-d) show microstructure and precipitate configuration for different aging conditions. All foils are viewed in $[\mathbf{0001}]$ direction. The triad represent $\{\mathbf{1\bar{2}10}\}$ direction. Aging temperature is 250 °C.

The β’’’ precipitate starts to nucleate at the initial stage of aging at 250 ^{o}C. The 30-min aging condition results in very fine β’’’ precipitates. The β_1 precipitate is believed to appear after around 1-hour aging, which results in a mixture of β’’’ and β_1 precipitates in the 2-hour aging condition. All 6, 9, and 100-hour aging conditions are β_1 dominant microstructure. The prolong aging in 100-hour doesn't alter the precipitate type but the β_1 microstructure gets coarser. Both 6 and 9-hour samples have comparable 0.2% tensile yield strength (76MPa) to the 30-min sample, all of which are higher than SHT sample (62MPa). The coarsening in 100-hour aged sample lowers the yield strength but does not improve the overall ductility compared to the 6 and 9-hour conditions. The 30-min sample has a higher ultimate tensile stress (UTS) of 230MPa compared with 215MPa for the 6 and 9-hour samples.

The measured tensile data show that the presence of β_1 precipitates does not degrade but unexpectedly increase the ductility. It is also noticeable that the β''' precipitates, on the other hand, exhibits a similar ductility compared to SHT condition. Table 5.1 summarizes the measured strain to failures in samples with and without β_1 precipitates.

Table 5. 1 Ductility values for conditions with and without β_1 precipitates

Microstructure	No precipitates	Only β''' precipitate	Only β_1 precipitates
Sample conditions	SHT	30 mins	6 hours, 9 hours, 100 hours
Strain to failure	13.7% ±1.3%	12.4%	17.9% ±0.3%
Number of samples	4	1	4

<u>5.2.2 Postmortem Characterization</u>

TEM samples were extracted from the tensile samples after failure to analyze the dislocation structures. Samples were taken perpendicular to the loading axis and approximately 5mm from the fracture surface. Non-basal dislocations were observed primarily in 9-hour aging sample as shown in Fig. 5.3. Diffraction analysis on the 9-hour aged sample in Fig. 5.3 c) and d) shows that the non-basal dislocations are <a> type $\frac{1}{3}[1\bar{2}10]$ dislocations since they are invisible under (0002) (g•b=0) but visible under $(\bar{1}011)$ diffraction vector (g•b≠0). Although non-basal dislocations can be observed in all tensile tested samples, as shown in Fig. 5.3 a) and b) where some basal dislocations extend out of the basal plane, the magnitude of dislocations extending out of plane, presumably by cross-slip, is different in these three conditions. Comparing Fig. 5.3 a) and b), the dislocation segment length and magnitude of cross-slip are much larger in the 9-hour aged sample compared to the 30 minutes aged samples. The 30-min-aged sample exhibited shorter dislocation segments due to the finer β′′′ precipitate distribution, resulting in a higher stored dislocation density as compared to the 9-hour aged sample. This may explain the relatively higher strain hardening in the 30 minutes aged sample.

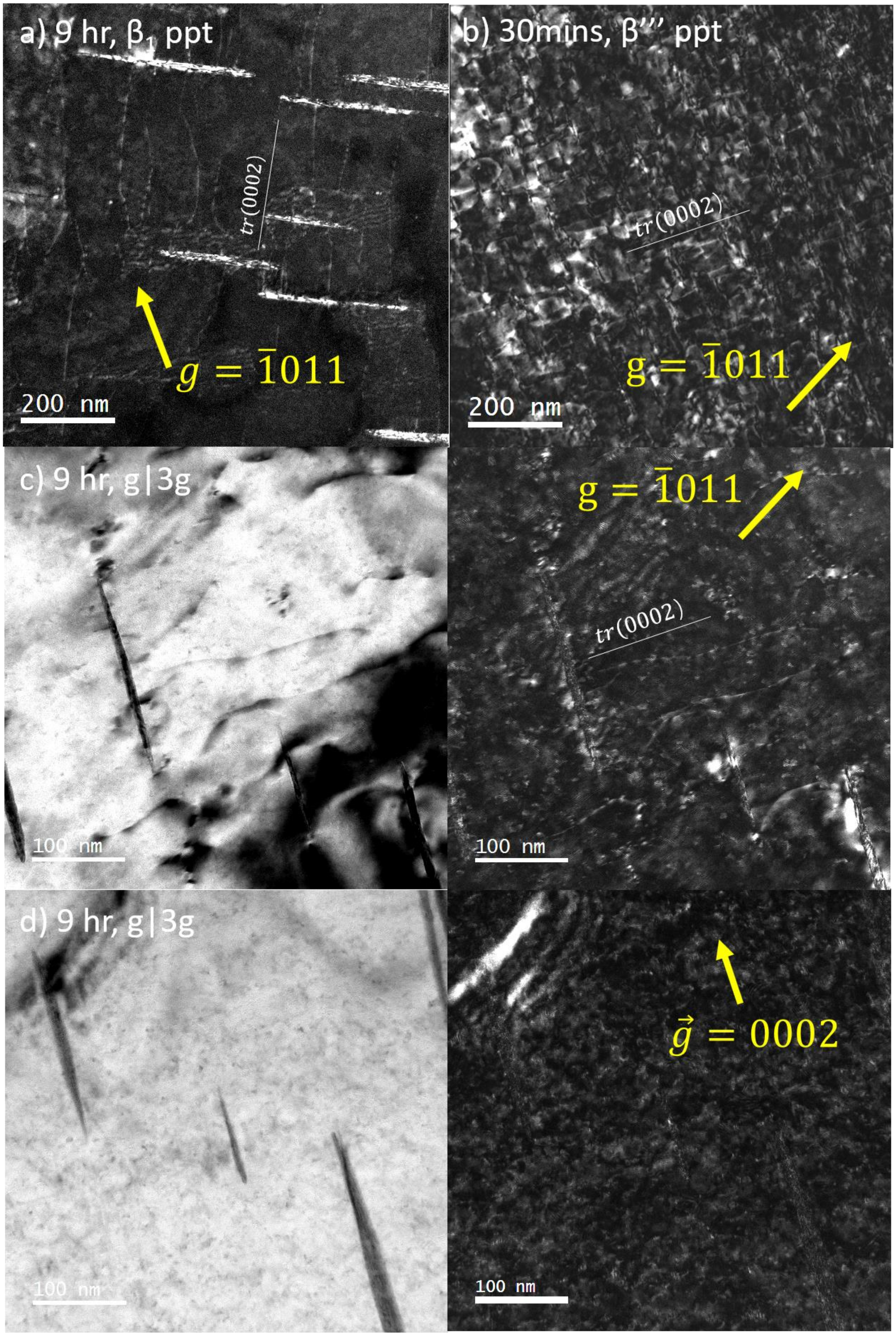
a) 9 hr, β1 ppt
tr(0002)
g = 1̄011
200 nm
b) 30mins, β''' ppt
tr(0002)
g = 1̄011
200 nm
c) 9 hr, g|3g
100 nm
g = 1̄011
tr(0002)
100 nm
d) 9 hr, g|3g
100 nm
g⃗ = 0002
100 nm

Fig. 5. 3 Dislocation structure of samples deformed to failure (10-20% plastic strain). Samples were from two aging conditions aged 9 hours (a, c-d) at 250oC and aged 30 min at 250oC (b). A high density of non-basal dislocations were present in all failed tensile samples. Two beam analysis on one specific area provided in c-d shows that the non-basal dislocations in 9 hours sample are <a> type dislocations. Image c) and d) are shot in g|3g weak beam dark field condition. Electron beam is parallel to $[1\bar{2}10]$ direction.

<c+a> dislocations were completely absent in the region shown in Fig. 5.3. This is consistent with *Koike's* result [17] in which no <c+a> dislocations existed if the stress axis was inclined (~10^{o} or more) away from basal plane. The weak fiber texture in the studied samples provides such a condition. Nevertheless, <c+a> dislocations were observed in other regions of all aged samples and an example from the 9-hour aged sample is shown in Fig. 5.4. The <c+a> dislocations dissociated onto basal planes and appeared as a long rectilinear line in Fig. 5.4. They occasionally double cross-slip to another basal plane leaving a step structure behind (as marked by the red line in Fig. 5.4 b)). This <c+a> dislocation configuration is very similar to the dislocation structure in pure Mg matrix [9]. The dislocation configuration difference between Fig. 5.3 and 5.4 is suspected to be related to the stress condition of the studied grains, which will be discussed in the next section.

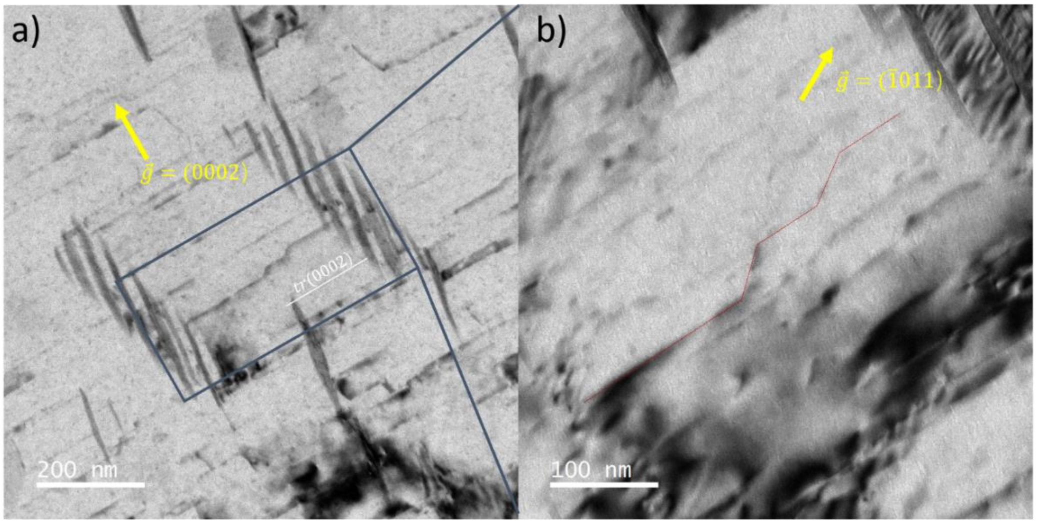

Fig. 5. 4 Dislocation structure in failed tensile samples of 9-hour aged materials. Note <c+a> dislocations are readily apparent in this foil. The red dashed line in b) is the <c+a> dislocation in the highlight box shown in 10a). The electron beam is parallel to $[1\bar{2}10]$ direction.

5.2.3 *In situ* Indentation in TEM

In situ straining in TEM provides a means to observe real time dislocation-precipitate interactions. In this section, both β′′′ and β_1 precipitate-dislocation interactions are described.

β’’’ precipitates

Fig. 5.5 shows the interaction of dislocations with β′′′ precipitates. The images in Fig. 5.5 were extracted from a video taken from an *in situ* experiment (see supplementary information). The sample was tilted to an approximate $[1\bar{2}1\bar{3}]$ orientation and had fine β′′′ precipitates embedded in the matrix. The basal plane was inclined to the plane of view and the schematic shows the wavy shape of gliding dislocations (blue curvy line). The full force field applied by the indentation tip is difficult to quantify. However, it should have an angle (10~20^{o}) to the basal plane, which is ideal for generating basal dislocations. Dislocations were emitted from the tip when the indenter contacted with the TEM foil. The observed dislocations were determined to be gliding on the basal plane. Propagating dislocations (1,2,3,4) were blocked by the β′′′ precipitates. When the indenter tip provided a sufficiently high shear stress, the pinned dislocations sheared through the β′′′ precipitates and moved to another pinned position. The arrowheads point to the locations of leading-edge components of the moving dislocations. The prismatic plane trace is marked in Fig. 8 as well to examine the motion along the c-axis. No significant motion of the leading-edge dislocation was observed along a prismatic trace, indicating that dislocation motion was mostly confined to the basal plane. For example, the dislocation labeled as “2” is observed to shift vertically from a) to b) in Fig. 5.5, along the trace of the basal plane. If any cross-slip occurred, the marked dislocation should have shown a displacement along the c-axis which would have also been reflected in the *in situ* video, resulting in a horizontal shift along prismatic plane trace. This was not observed.

Following the *in situ* indentation, the TEM foil was removed after the initial *in situ* test and mounted on a conventional double-tilt stage to characterize the precipitate morphology after dislocation interaction. Fig. 5.6 shows high-angle annular dark field (HAADF)-STEM images of precipitates near the indent. The electron beam was parallel to the $[1\bar{2}1\bar{3}]$ orientation and both basal and prismatic traces are marked in the figures. A clear offset along the basal trace indicates that the β’’’ precipitate was sheared by the basal dislocations in the *in situ* video. The offset is 1.3 nm suggesting shearing by a total of four to five basal dislocations, which is consistent with the number of dislocations observed in the *in situ* video. This characterization confirms that basal dislocations were contained in the basal plane during the interaction and sheared through the β’’’ precipitates when the shear stress exceeded some critical value.

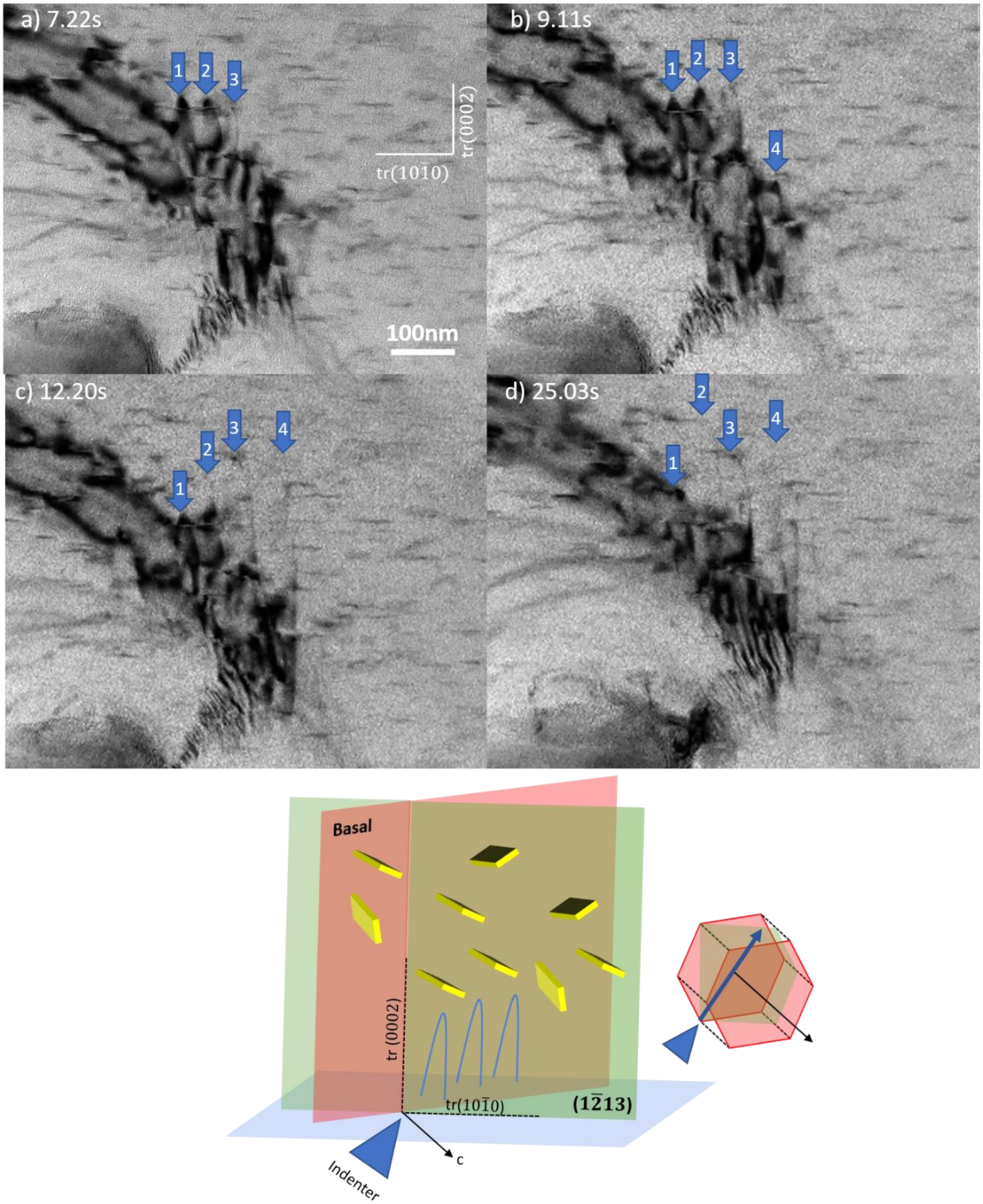

Fig. 5. 5 a) to d) shows basal dislocation interaction with β''' precipitates. The dislocations of interest are marked with numbered arrow heads. The schematic illustrates the relative orientation between the observation plane and basal and prismatic planes. Yellow blocks and blue wavy lines represent β''' precipitates and basal dislocations, respectively. The blue arrow in the schematic HCP structure shows an approximate force vector applied to the TEM foil. Dislocations were emitted from the indenter tip.

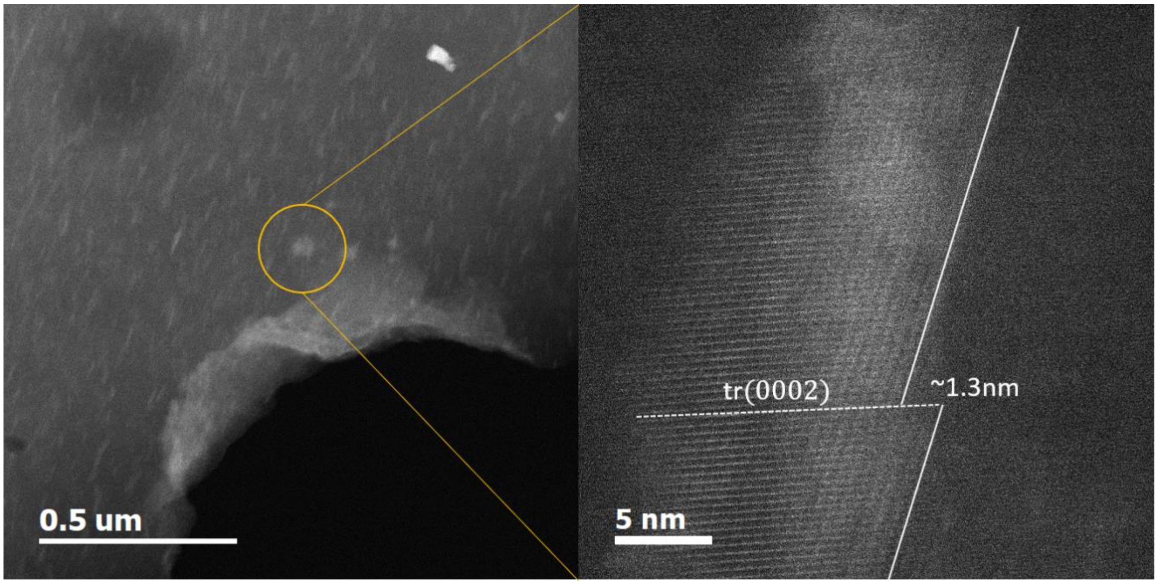

Fig. 5. 6 Postmortem characterization of precipitate morphology after an in situ indentation experiment. The basal offset shown in the image on the right was observed at a β''' precipitate close to the indenter tip.

β_1 precipitates

TEM foil orientation $[1\bar{2}1\bar{3}]$ was selected to show dislocation interaction with β_1 precipitates. The β_1 precipitates have a plate-like morphology which is similar to the β′′′ precipitates but are coarser due to the longer (9 hours) aging time. Fig. 5.7 shows the $[1\bar{2}1\bar{3}]$ sequence of basal dislocation interactions at the β_1 precipitate interfaces. The applied stress direction is similar to the β′′′ precipitate case shown in Fig. 5.5. The dislocations of interest (marked as 1 and 2) were elongated along the <a> Burgers vector to maximize the low energy screw segments, with two ends attached respectively to two precipitates highlighted by yellow dashed lines. In Fig. 5.7 a), when the dislocations 1 and 2 first make contact with the precipitate, they were moving on two parallel basal planes. The basal plane containing dislocation 1 is outlined by the red dashed lines. The green and blue dots track the motion of the pinning points of the two dislocations on precipitate interface. The purple box represents one prismatic plane close to the interacted precipitate. Once the dislocations get pinned, (Fig. 5.7 b), they spontaneously start to straighten and elongate the screw segment. An important dislocation configuration transformation was observed between Fig. 5.7 b)-c). In dislocation 1, the segment close to the pinning point straightened itself as well as exhibiting a zig-zag shape in Fig. 5.7 c). This transformation forced the dislocation segment close to the pinning point to change to a screw component, which enabled further cross-slip movement on prismatic plane (Fig. 5.7 d). Immediate after the transformation, the pinning points of both dislocations moved upward and straightened as one rectilinear screw dislocation. As shown in Fig. 5.7, the direction that dislocations moved upward is along the c-axis and the plane containing the cross-slip dislocation is the prismatic plane.

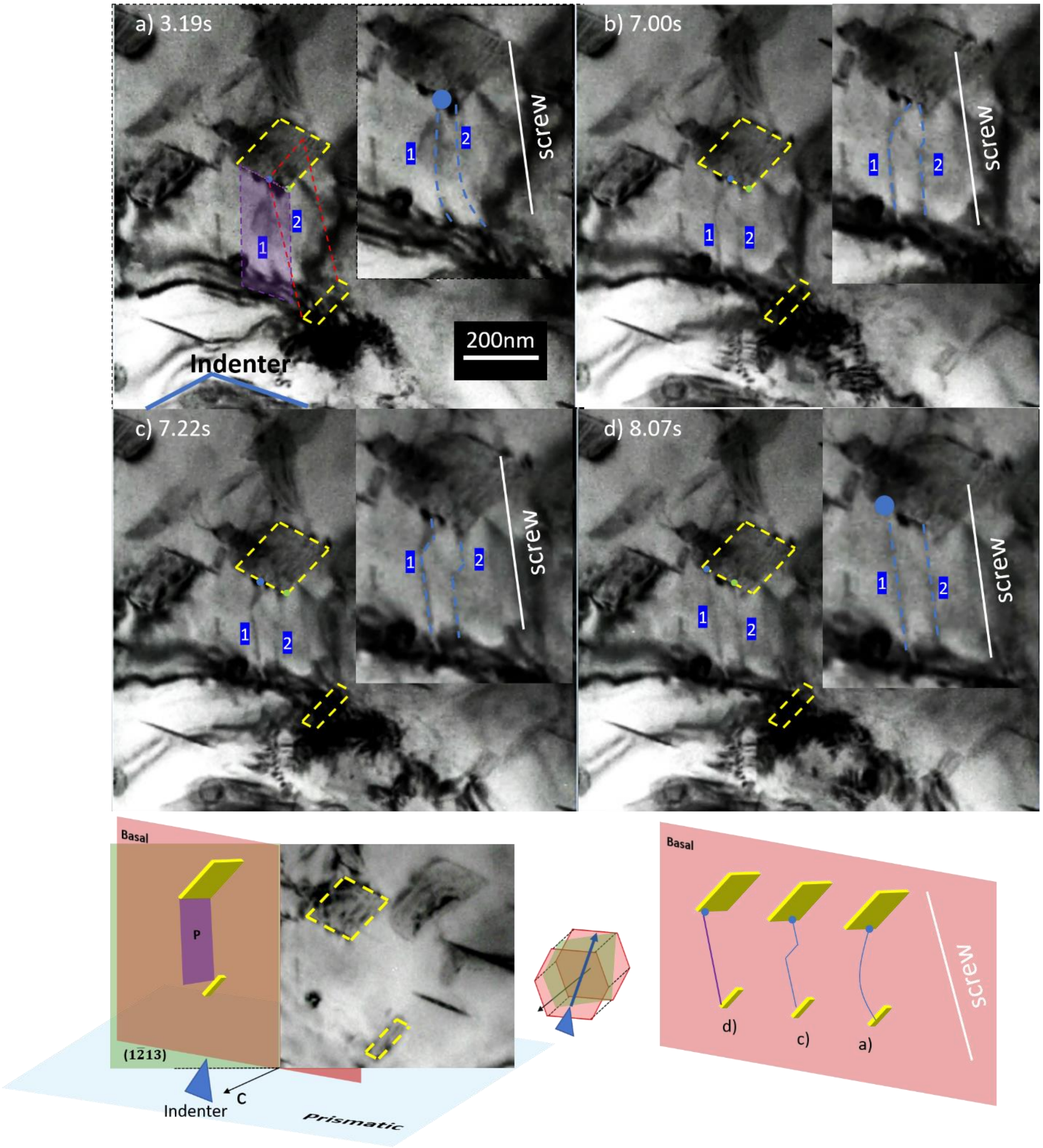

Fig. 5. 7 Sequence of dislocation interactions with β_1 precipitates. Images show a cross-slipped dislocation pinned at the departure side of the precipitate. The pinning point of dislocations 1 and 2 are marked with blue and green dots. The dislocations of interest are marked by dashed blue line in the enlarged inset at top right of each image. The schematic shows the viewing angle and applied force direction. The bottom right schematic summarizes the cross-slip process of <a> dislocation forward to prismatic plane. The purple color line suggests the dislocation is out of original basal plane.

Another cross-slip activity in the later portion of the video is shown in Fig. 5.8. The dislocation marked as “3” cross slipped on the yellow highlighted precipitate as tracked by the blue attached point moving upward from b-d). The cross-slip phenomenon is similar in nature to the interaction shown in Fig. 5.7 except that dislocation 3 interacted with interface dislocation 4 during the cross-slip. From b-c), dislocation 3 connected with one end of dislocation 4 when it moved upward and dragged it up at the yellow highlighted precipitate broad interface. It is more obvious from c-d) as dislocation 3 kept moving forward. The interfacial dislocation 4 suggests that it can move on the precipitate broad interface.

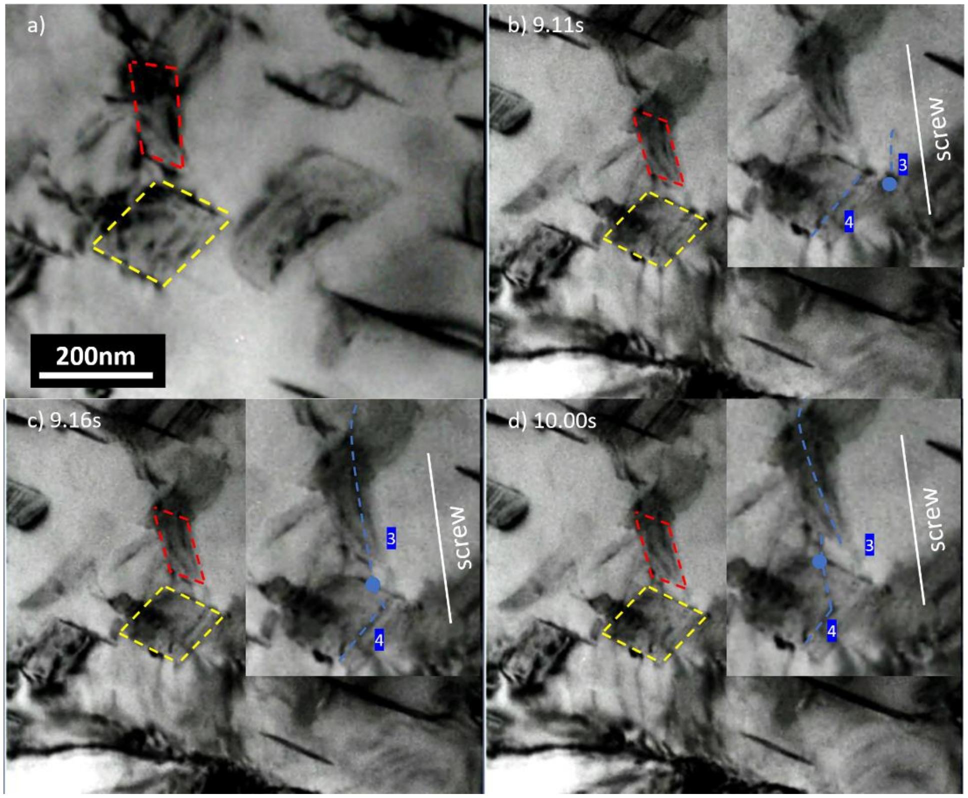

Fig. 5. 8 The sequence of dislocation 3 cross slip at the precipitate interface. a) shows the precipitate configuration before deformation.

Although dislocation 3 in Fig. 5.8 cross slipped significantly, moving upward approximately 150nm, in the end it did not overcome the yellow highlighted precipitate. However,

Fig. 5.9 shows that, in some situations, dislocations are able to overcome precipitates by double cross-slip. For example, dislocation 2 cross slipped to the upper surface of the red highlighted precipitate in c) and glided on it in d-e) and eventually cross slipped back to original basal slip plane in f). The reason for the difference between the cross-slip events in Fig. 5.8 and 5.9 is assumed to be the shear force along the c axis. A higher local shear stress in Fig. 5.9 leads to the higher distance of cross-slip.

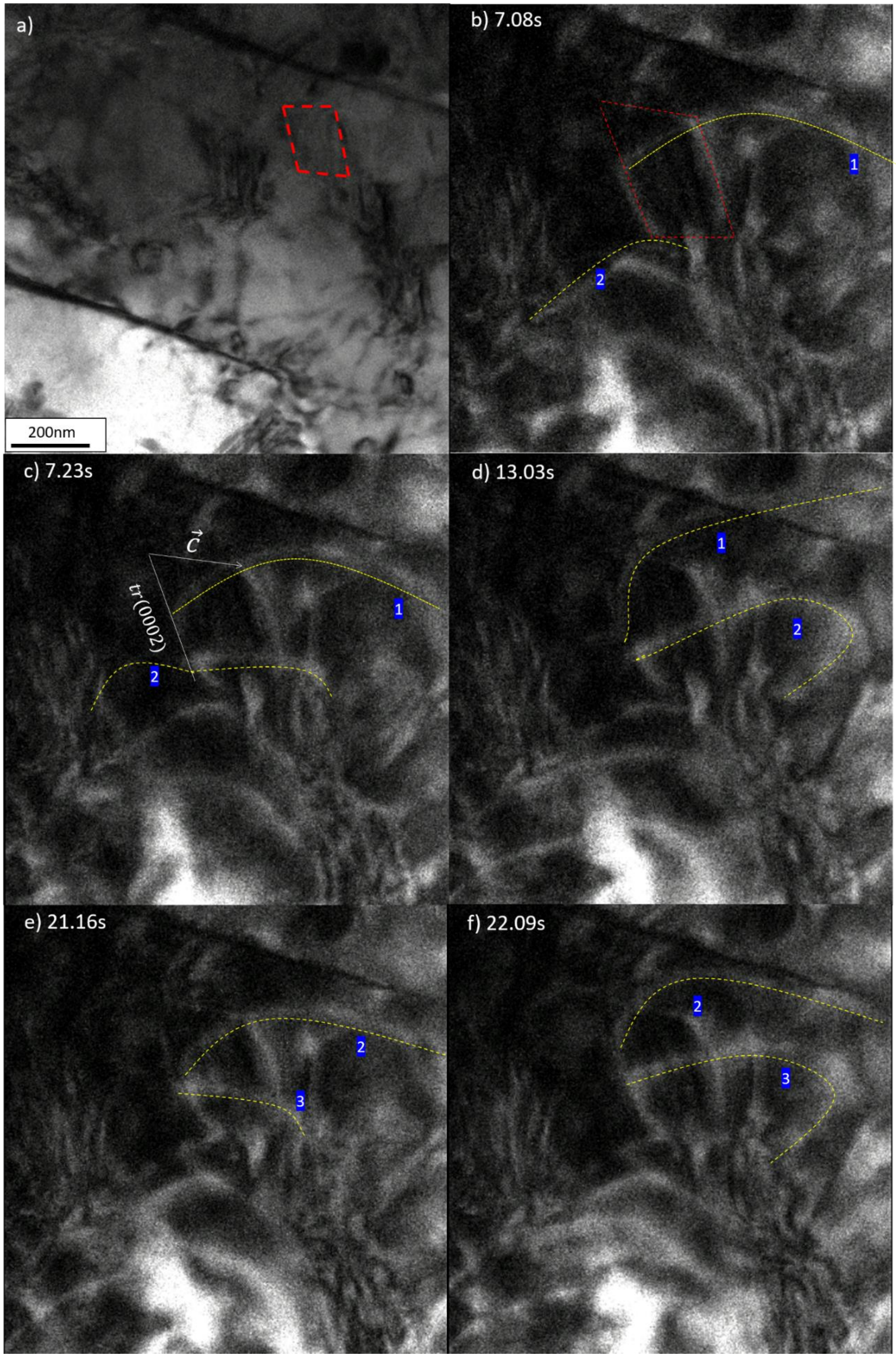
a)
200nm
b) 7.08s
1
2
c) 7.23s
$\vec{c}$
tr(0002)
1
2
d) 13.03s
1
2
e) 21.16s
2
3
f) 22.09s
2
3

Fig. 5. 9 The sequence of dislocations 1,2,3 overcome the blocking precipitate by double cross-slip mechanism. The TEM foil orientation is close to $[\mathbf{1\bar{2}1\bar{3}}]$.

5.2.4 Simulations Results for β_1 Precipitate-Dislocation Interaction

MD simulation results for the edge dislocation case interacting with a β_1 precipitate are shown in Fig. 5.10 and Fig. 5.11. As mentioned in the method section, we use a more reliable Y MEAM potential [44] to simulate the Nd behavior, which has been verified by DFT result to be a suitable replacement. For clarity, we will use Nd rather than Y in the following analysis.

This simulation showed a perfect basal edge dislocation that naturally dissociated into two partial dislocations connected by stacking fault areas (green color in Fig 5.10). A consistent shear stress of 200MPa is applied to the dislocation to overcome the inter-precipitate gap. The studied edge dislocation glides to the end of departure side. Nd atoms are isolated and highlighted as yellow color from Mg_3Nd precipitate to show the precipitate deformation. Other than bowing around the interacted precipitate, the studied dislocation glided at the precipitate interface from a)-d), leaving an interface dislocation at the interface marked by the red arrows. However, the interface dislocations are absorbed at β_1 precipitate interface, leaving atom displacement at the interface as shown by the black box in the Fig. 5.10. From a)-d), it is shown that the deformation localizes at the front end and precipitate interface as dislocation gliding along interface, hence the inside of the precipitate is free of displacement. Unexpectedly, the shearing occurs at f) in which the inside of the whole precipitate shows a clear shift compared to previous images. The precipitate is eventually sheared and it shows an offset (marked by purple arrows) at the precipitate edge in e) and f). This discrepancy between the simulation and experiment may be due to the inherent high strain rate in MD simulation and the small size of simulated precipitate. The small precipitate size increases the dislocation curvature, and hence raises its line tension, resulting a higher shear stress which may enhance shearing through the precipitate.

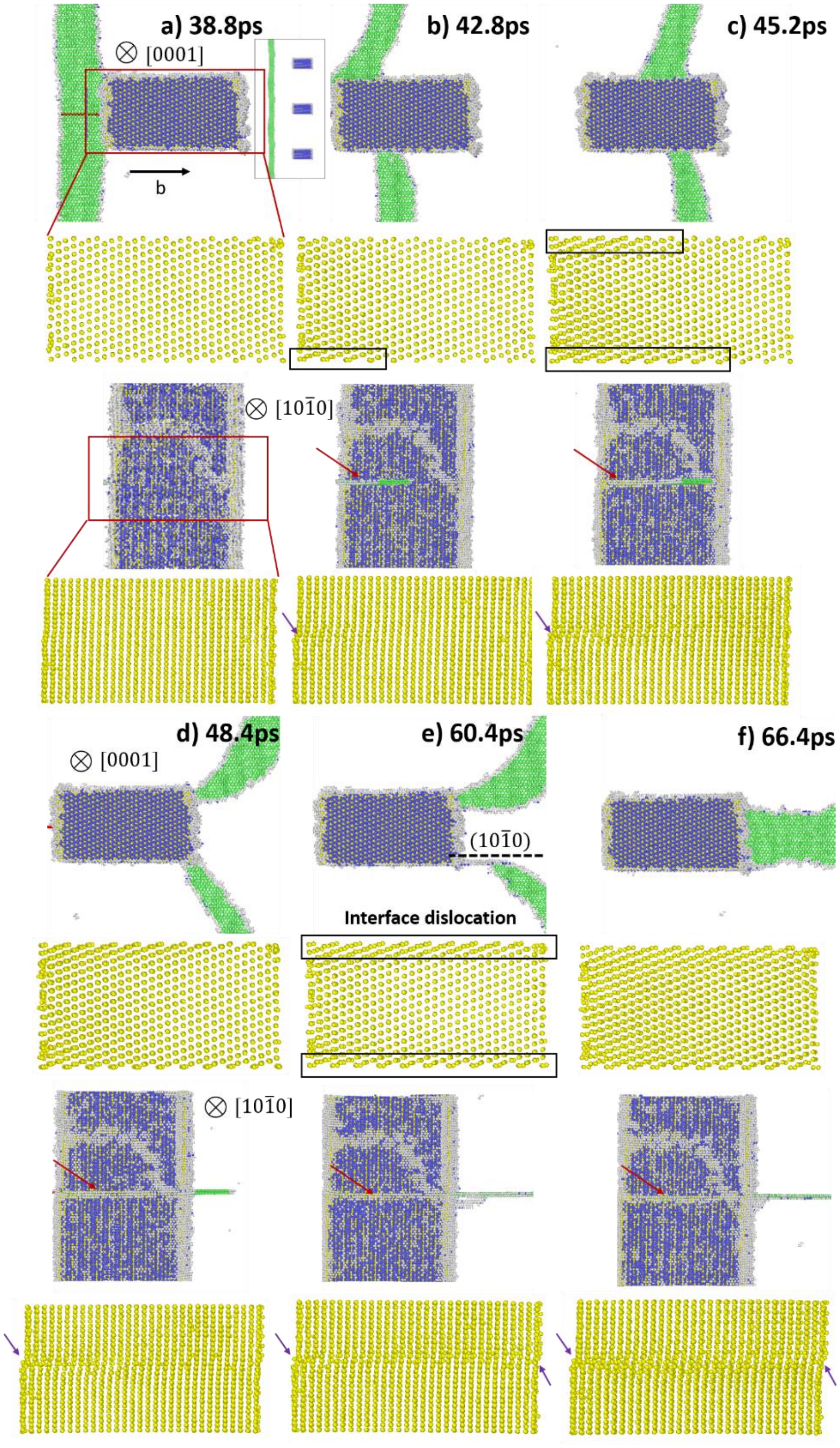

Fig. 5. 10 Basal edge <a> type dislocation glided to the end of precipitate and eventually sheared the precipitate. Color represents different local atomistic structure. Green is fcc, blue is bcc and grey indicates other structures. The Nd particles are highlighted as yellow and isolated at bottom image for viewing purpose. Dislocation glide was from left to right in the bottom image.

As one may notice in Fig. 5.10 e), the dislocation is arranged with some component aligned to $[10\bar{1}0]$ plane which adopts a screw configuration. A small degree of cross-slip is found when viewed from $[10\bar{1}0]$ direction. The cross-slip phenomenon is more significant in the second dislocation-precipitate interactions for the second dislocation gliding from the left side of each image due to the periodic condition of the supercell shown in Fig. 5.11. Close attention should be paid to the precipitate departure side (the right side of each image in Fig. 5.11), where the dislocations are strongly pinned and unable to easily detach from the precipitate. The subsequent dislocation cross-slip activities are shown in b) to f), in which the dislocation activity is demonstrated from two aspects, the top ones viewed from [0001] direction and bottom ones viewed from $[10\bar{1}0]$ direction.

Under this pinning position, a bowed segment on the departure side adopts a screw characteristic as indicated by the arrow in Fig. 5.11 b). The screw component spontaneously cross-slips on the prismatic plane and forms a kink behind. The cross-slipped region is then dissociated again on another basal plane and drags up more dislocation segments by kink propagation. The MD simulations reflect the exact F-E cross-slip mechanism shown in Fig. 2.3. Interestingly, the non-cross-slip segment on the original slip basal plane combines on the departure side of the precipitate as shown in Fig. 5.11 d-e). The subsequent simulations e) and f) show that the movement of the kink is reversed, gradually pulling back the previous cross-slip dislocation to the original slip plane. Eventually, all cross-slip components in b) to e) are pulled back to original basal slip plane and able to keep propagating as shown in f).

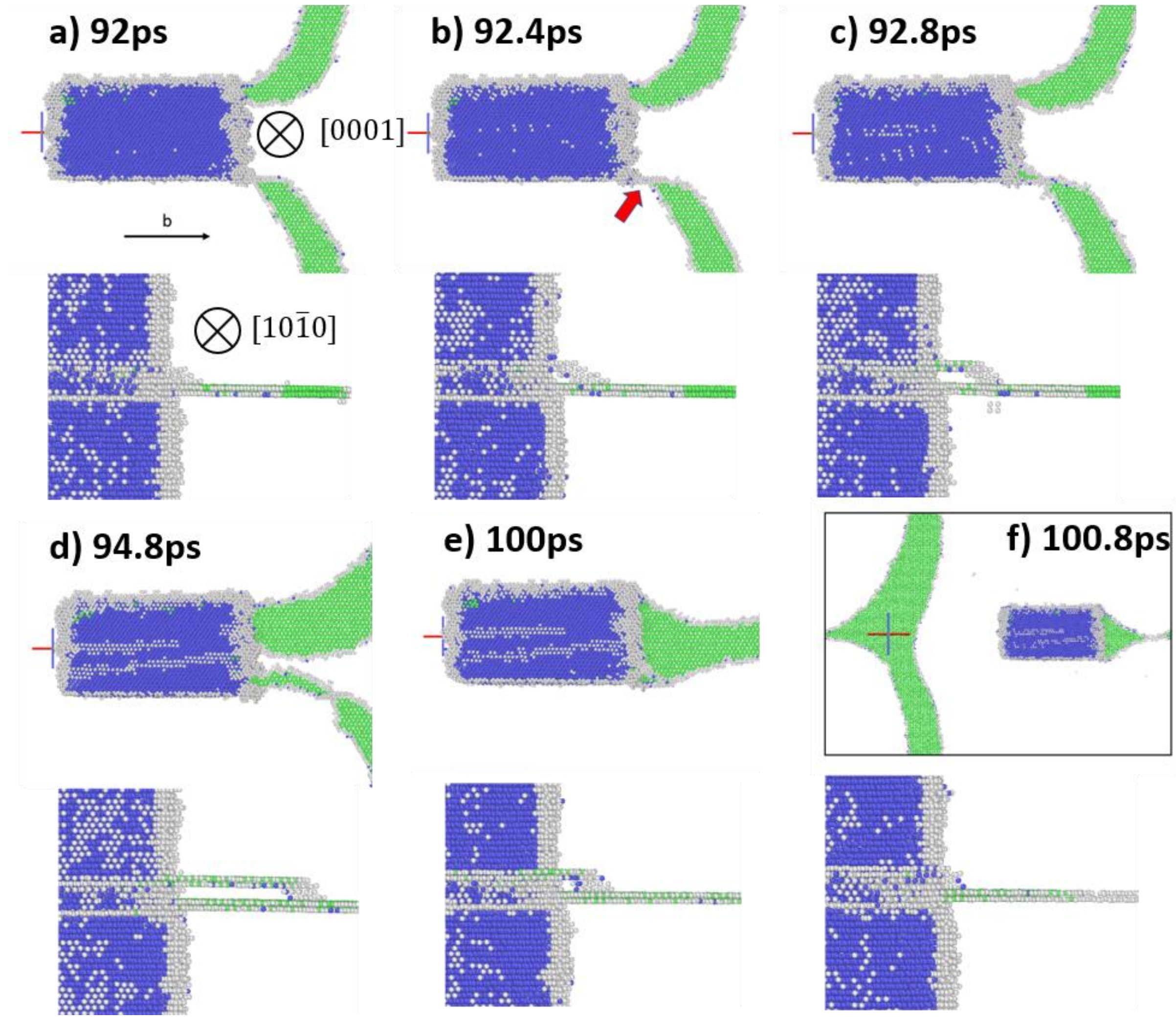

Fig. 5. 11 shows MD simulations of second edge dislocations in the HCP matrix interacting with β_1 precipitates. Note the cross slip of the screw segment on the departure side of the precipitate starting early in this process (from image b). In each sub-figure, the above image is the view along [0001] direction, and the bottom image is the view along $[10\bar{1}0]$ direction.

Interactions between a screw dislocation and β_1 precipitate are shown in Fig. 5.12. To reduce the computational work load, precipitates are shortened but maintained their interface structure. The realistic configuration is shown in Fig. 5.12 a). The screw dislocation behaves similar to the edge dislocation case: the glide of a perfect screw dislocation shown in Fig. 5.12 a) to b), and the cross-slip on the prismatic plane shown in Fig. 5.12 c) to d). However, in this case, a screw dislocation itself has the screw component suitable for the cross-slip, hence leading to a higher magnitude of the cross-slip event and a longer cross-slipped dislocation line out of the original basal slip plane once the dislocation meets the precipitate, as shown in Fig. 5.12 c) and d). In addition, the cross-slipped region does not re-dissociate on another basal plane. In Fig. 5.12 c) to d), the non-cross-slipped region is bowed significantly, which inhibits the propagation of dislocation kink. The cross-slipped region does not retreat to the original basal plane but is maintained on the prismatic plane despite a high local shear stress for a longer time compared with the cross-slipped region for the edge dislocation in Fig. 5.10 and 5.11. This indicates that this cross-slipped region has a very high lattice friction in the propagating direction. It also indicates that it is possible for this dislocation to overcome the whole precipitate by cross slip to another basal plane. However, in this simulation, the cross-slipped part still is pulled back to the original basal plane as the simulation continues (not shown in Fig. 5.12). In reality, the magnitude for the dislocation to cross slip and the possibility that a dislocation can overcome a whole precipitate by cross slip is assumed to be related to many factors such as the local shear stress, dislocation characteristics, inter-precipitate spacing and the size/shape of precipitates.

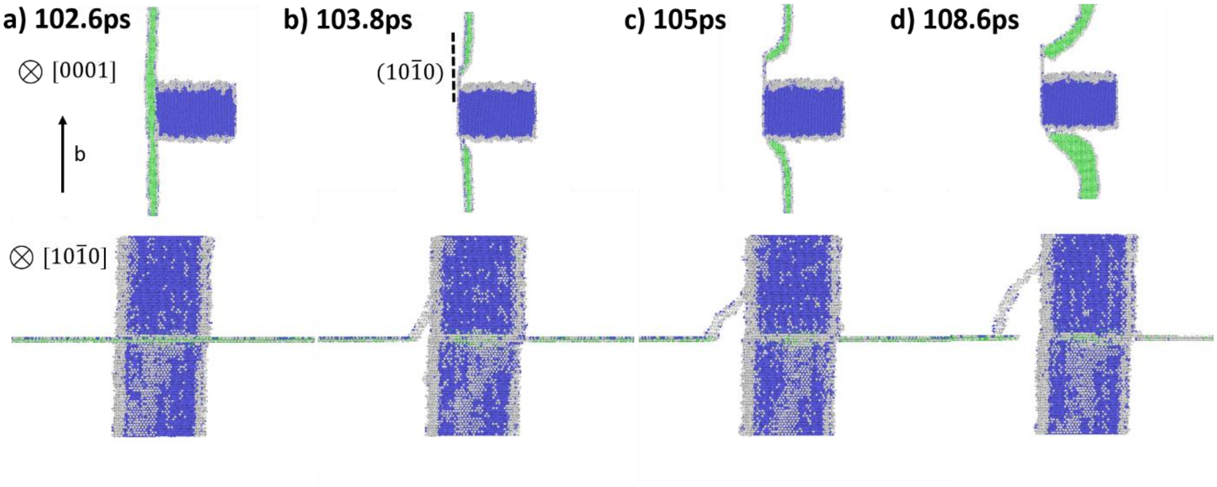

Fig. 5. 12 shows screw dislocation cross-slip phenomenon when it interacts with the precipitate. The top images are viewed from [0001] and the bottom images are viewed from $[10\bar{1}0]$ directions. The

long cross-slipped region of the dislocation can be observed on the left side of the precipitate (the grey curves out of the basal slip plane).

5.3 Discussion

5.3.1 Cross-Slip Mechanism

The *in situ* straining experiments on β''' and β_1 dominant microstructure show a significant difference in behavior. In the microstructure with only β''' precipitates, dislocations directly shear through the β''' precipitates. In contrast, in conditions in which β_1 precipitates predominate, dislocation generally do not shear the precipitates but, as shown in Fig. 5.7 and Fig. 5.10, by-pass them by an interface glide mechanism as described in Chapter 4 and then exhibit a pinning on the departure side which involves a cross-slip mechanism. In the case of screw dislocations, cross slip happens when they first contact the precipitate as shown in Fig. 5.8, Fig. 5.9, Fig. 5.12 and Fig. 5.14. Both scenarios indicate that the intrinsic strength of precipitate plays an important role in dictating dislocation interactions. The fully coherent β''' precipitate has basal slip systems that are identical to the HCP matrix hence they can be sheared. In contrast, the β_1 precipitate has an ordered $D0_3$ structure which has only one continuous slip system with the matrix. Our study (presented in Chapter 6) shows it requires at least 250MPa for that special aligned basal dislocation to shear a β_1 precipitate. In fact, for most of the matrix dislocations, their Burgers vectors and glide planes do not align with β_1 precipitate slip system, making it even harder to shear. Since basal dislocations cannot easily shear the β_1 precipitates, as shown in MD simulation Fig. 5.10 and Fig. 5.11, they will instead glide along the interface to the departure end of precipitate. Interface dislocations are generated during the dislocation gliding event as shown in Fig. 5.10. This process has been characterized and discussed by our previous *in situ* experiment result in Chapter 4. As mentioned in Chapter 4, we pointed out the interface dislocation energy relaxation is the fundamental reason for the interfacial gliding mechanism. The simulation result in Fig. 5.10 reveals the interface dislocation absorption may be responsible for the energy relaxation. Similar results have been found in $Mg_{17}Al_{12}$ precipitate-dislocation MD simulation [64, 43]. It is also plausible that the dislocations adopt a screw characteristic before they interact with precipitate as shown in Fig. 5.8 and MD simulation Fig. 5.12. The dislocation characteristic facilitates the cross-slip process so that they may cross slip rather than move by interfacial glide when they interact with precipitate. Therefore, it is important to note that the interaction mechanism is dependent on the initial dislocation characteristic.

For the scenario in which the dislocation glides at the precipitate interface, after gliding to the departure end of β_1 precipitate, the detachment process is presumably controlled by dislocation at the departure side. As shown in Fig. 5.13, the red solid line dislocation is pinned between two precipitates, a situation very similar to Fig. 5.7. The successive propagation or the detachment process is dependent on dislocations on the other side represented as red dash line in route one. If there is no such dislocation, the solid line dislocation must bow out as shown in route two. If there is no dislocation to combine and the pinning gap is narrow which requires large shear stress, the pinning dislocation is unable to propagate until shear stress is built up. Before the basal plane shear stress is enough for the dislocation to overcome the pinning position, meanwhile the stress along the c-axis, which leads to cross-slip, can build up as well.

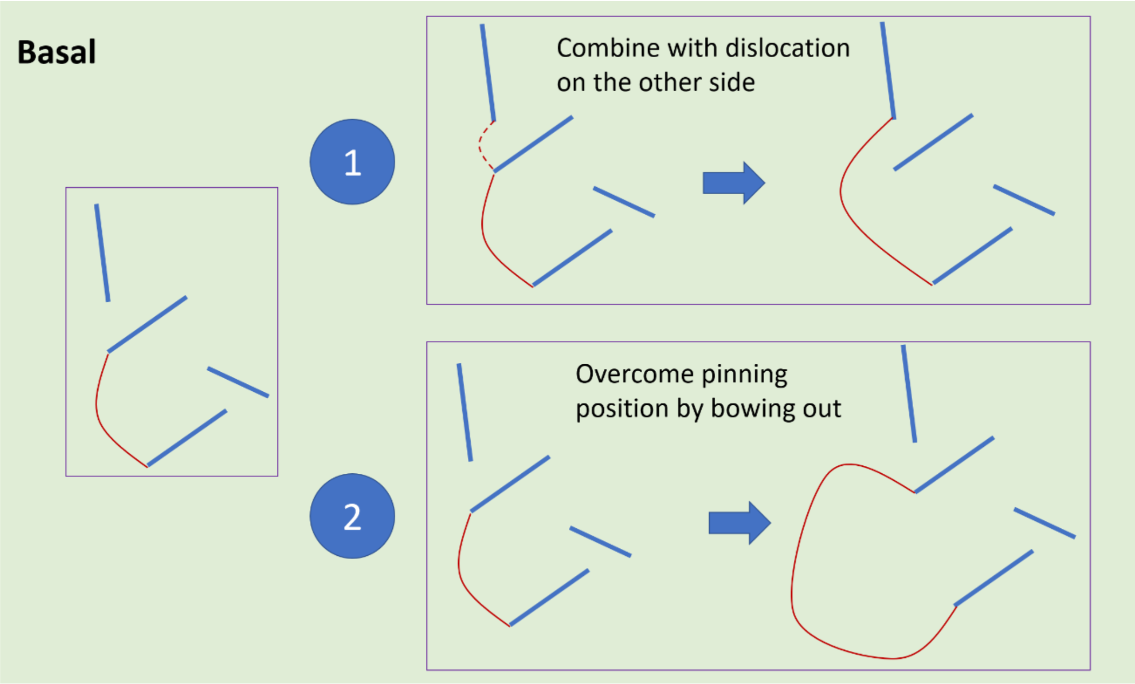

Fig. 5. 13 Schematic of dislocations (red line) that get pinned at the β_1 precipitate (blue line) departure side and two scenarios are plausible for the dislocation.

As shown in MD simulations Fig. 5.11 and 5.12 that correspond to TEM images (Fig. 5.7 c and d), the curved mixed dislocation has to realign itself to the screw configuration before cross-slip. This is very similar to the F-E cross-slip mechanism described in the introduction section.

For a dislocation with a screw characteristic, it is shown in Fig. 5.9 that it can overcome the precipitate by cross-slip. The mechanism is illustrated in the Fig. 5.14 below. This mechanism requires interfacial dislocations to move on the precipitate broad facet in order to maintain dislocation continuity. The fact that this mechanism leaves no prismatic loop behind distinguishes it from the Hirsch mechanism, in which dislocation cross slips two to three times, leading to formation of prismatic loops [68, 69]. However, Hirsch's model was for spherical precipitates (alumina in copper-zinc alloys). In this study, the plate-like β_1 precipitates provide a broad facet parallel to prismatic plane which is also a glide plane. One hypothesis is that the interfacial dislocations are generated from cross-slip and they are able to move as <a> type dislocation on the prismatic plane which is precipitate broad facet as well. The fact that these non-basal dislocations are confined at precipitate interface makes it glissile. This mechanism is not applicable to β''' precipitate, not only because it is easier to shear through but also the β''' precipitate has habit plane $[1\bar{2}10]$ which is not the slip plane for prismatic <a> dislocations.

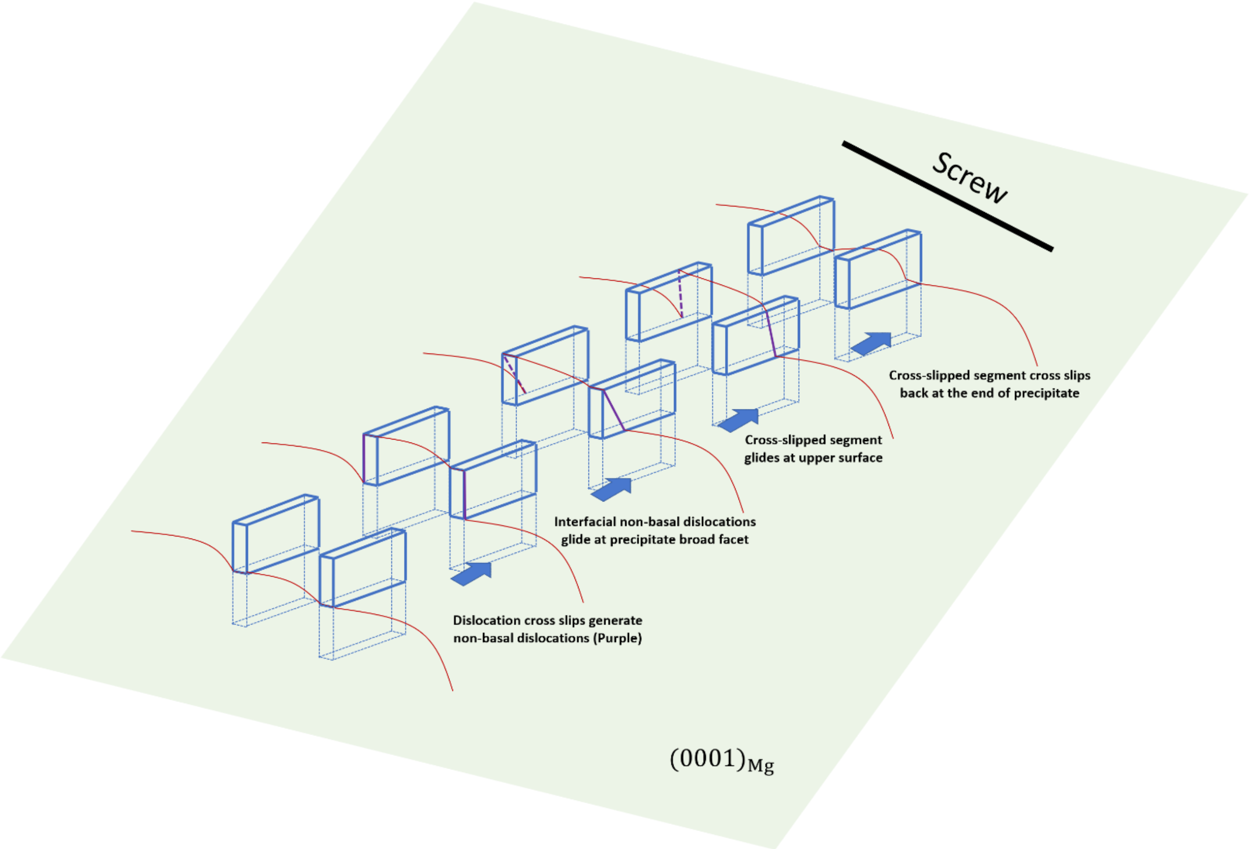

Fig. 5. 14 Schematic of screw dislocation overcoming a precipitate by a cross-slip mechanism. The red lines represent dislocations and blue boxes represent precipitates.

Considering the non-basal dislocations, cross-slip was observed in all heat treatment conditions in tensile tested samples, the mechanism is regarded as intrinsic to the Mg matrix. However, in the 30 min. aged condition containing β''' precipitates, at least at the initial deformation stage as shown in Fig. 5.6, dislocations mainly glide on basal planes and no cross-slip is observed. We hypothesize that dislocations are not strongly pinned at β''' precipitates and so the local stress does not build up along c-axis to initiate cross-slip, hence, basal dislocation slip is favored and observed in β''' precipitate microstructures. At later stages of deformation, the increase of dislocation density will promote dislocation-dislocation interactions, resulting in a pinning environment for basal dislocation which apparently leads to cross-slip. However, since the cross-slip occurs at later deformation stage, dislocations are close to each other, making the magnitude of cross-slip limited as shown in Fig. 5.3 a) and b).

5.3.2 Implication on Room Temperature Tensile Ductility

The engineering stress-strain curves shown in Fig. 5.1 and ductility values presented in Table 5.1 suggest that the presence of β_1 precipitates helps to improve the strength as well as marginally increase the overall ductility. The fine β''' precipitate distribution in 30-min aged sample accounts for the initial high strain hardening but doesn't increase the ductility. Similar mechanical properties comparison between β''' and β_1 precipitate microstructure can be found in Zheng *et al.* study on Mg-Gd-Nd-Zr alloy [23]. In the research, Zheng aged the sample from SHT to peak aged and overaged conditions, providing different precipitate microstructures including exclusively β''' and β_1. It was found that conditions in which the β''' precipitate microstructure predominates have inferior elongation compared with a condition in which the β_1 precipitate microstructure predominates (~2.5% *vs.* ~11%), while maintaining similar tensile yield strength (~225MPa *vs.* ~200MPa). It can be argued that the improvement of ductility in β_1 precipitate microstructure is due to the larger inter-particle spacing. However, the overaged sample in Zheng's research shows the difference is minimal since the coarsened β_1 precipitates have been almost interconnected with each other. Although both conditions have lower elongation than SHT condition (~21%) in Zheng's study, this may attribute to the casting texture and different alloy composition. Another study by Zhou *et al.* [24] reports on the tensile behavior of extruded Mg-2.2wt.%Nd, which is very similar to our study. The tensile tests from β_1 precipitate dominated sample and SHT sample show both conditions have similar strain to failure. Regardless of the texture difference in these studies, we can conclude the β_1 precipitates microstructure has a better balance between strengthening material and preserving ductility.

The *in situ* indentation in this study gives an insight for the precipitation hardened alloy ductility from dislocation-precipitate interaction perspective. Considering that the sessile <c+a> dislocations in the matrix are detrimental to ductility and combining the *in situ* results, it can be hypothesized that the ductility improvement is related to the promotion of non-basal (prismatic) dislocation cross-slip due to interactions with the β_1 precipitate microstructure. With the activation of basal dislocation cross-slip activity, a newly generated non-basal dislocation can glide as a kink in the matrix or glide as an interfacial dislocation along the precipitate broad interface (Fig. 5.14). As Agnew pointed out for the case of AZ31B alloy [18], two extra slip systems $\frac{1}{3} < 1\bar{2}10 >$ $(10\bar{1}0)$ are added through cross-slip. Furthermore, it is also hypothesized that the cross-slip mechanism may lead to a dislocation source for non-basal dislocation multiplication [70, 71].

Although the four new slip systems do not completely satisfy the Von Mises criterion for tensile ductility of a random polycrystal, it appears to have some positive effect on the tensile ductility in this study. Part of the reason for this observation is likely due to the weak fiber texture present in the extruded bar (as shown in Fig. 5.1). This causes the tensile axis to be oriented 10-20^{o} away from basal plane, which is highly favorable for <a> type dislocation activation. In other words, the deformation is mainly relieved by basal slip. As shown in Fig. 5.3, some samples only have <a> type dislocations suggesting a major deformation on basal plane.

However, as argued by Agnew [18], the four slip systems only help with ductility when the material is deformed under unconstrained condition which essentially means little strain along c- axis. Due to the compatibility stress from surrounding grains, certain grains are deformed along c- axis, suggested by activation of <c+a> slip. In the failed tensile bar, there are samples that have significant amount of basal dissociated <c+a> dislocations as shown in Fig. 5.4. Although the activation of <c+a> dislocations could provide the strain along the c-axis, these dislocations get dissociated into sessile segments, and therefore, are considered to be detrimental to the ductility [9]. In conclusion, although the <a> type dislocation cross-slip can help with ductility to some degree, the limitation of tensile ductility for random polycrystals still comes from c-axis strain.

5.4 Conclusions

In situ straining in TEM was performed to characterize the interaction between <a> dislocations and β’’’ and β_1 precipitates. Tensile properties of different precipitate microstructures were characterized. Coupled with *postmortem* study of dislocation structures and MD simulations, the key findings are:

1. β’’’ precipitates are sheared by <a> dislocations on basal planes but β_1 precipitate barriers are overcome by cross-slip. For <a> non-screw dislocations interacting with β_1 precipitates, the departure side provides a strong pinning point for propagating dislocations, where the stress along the c-axis can build up to activate cross-slip. The cross-slip mechanism is similar to Friedel-Escaig (F-E) mechanism and requires formation of perfect screw dislocation and nucleation of kinks.
2. Screw dislocations can cross slip once they interact with β_1 precipitate on the front end. The cross-slip activity provides non-basal (prismatic) dislocation segments that can glide

at β_1 precipitate broad facet. The blocking β_1 precipitate can be overcome with double cross-slip.

3. The profuse activity of dislocation cross-slip in β_1 precipitate dominant microstructure adds up to two extra slip systems which may be at least a partial explanation for the increase in tensile ductility observed in the aged Mg-Nd alloys containing β_1 precipitates.

CHAPTER 6

Dislocation Pile-ups at β_1 Precipitate Interfaces

6.1 Introduction

For these non-spherical, extended β_1 precipitates, the interaction between dislocations and precipitates have not been fully characterized. Given the size, shape and distribution of β_1 precipitates, a variety of dislocation-particle interaction mechanisms are feasible [38, 40, 72]. In our earlier investigation (Chapter 4) on dilute aged Mg-Nd alloys, we reported on a new interfacial glide mechanism of a single dislocation interacting with β_1 precipitates [73]. It was shown that the bypass of dislocations around precipitates involved glide along the broad interfacial facets of the precipitates. This should result in a somewhat lower stress for bypassing the precipitates compared to the classical Orowan looping. The interface glide mechanism describes the dynamic process between single dislocation and precipitate. More specifically, the interaction occurs when dislocation motion direction is parallel or close to the broad facet of β_1 precipitates. As discussed in Chapter 4, the interface gliding mechanism is suppressed when the gliding dislocation motion direction is perpendicular to the broad facet. In the Chapter 5, the *in situ* straining experiment in Fig. 5.8 reveals that screw basal dislocation can cross slip to prismatic plane when moving toward the β_1 precipitates broad facet.

Supplementary MD simulations further point out the cross-slipped components receive a high lattice friction along propagating direction, as shown in Fig. 5.12. Such cross-slipped dislocations components are pinned by precipitates and potentially behave as obstacle to the following dislocations. The influence of cross-slip strong pinning effect is under evaluated to the dislocations-precipitates interactions.

In this Chapter, we investigate, using *in situ* straining in TEM, a microstructural region that has a high density of planar precipitates that act to confine slip within a small region. This small confined region provides a unique window to characterize and analyze a general precipitate-dislocation interaction mechanism in such an extended β_1 precipitate microstructure. We validate this strengthening potential using the results of a computational first-principles study.

6.2 Results

For the aging condition used in this study, the average dimensions of the β_1 precipitates were measured from $[1\bar{2}10]$ (length and thickness) and [0001] (width) orientations, to be approximately 130nm (width w) x10nm (thickness t) x310nm (length). Because of the symmetry of HCP habit planes, the average inter-particle spacing of β_1 can be estimated to be approximately 260 nm according to Eq. 6.1 [72]. f is the precipitate volume fraction.

$$\lambda_{basal} = \frac{1.075\sqrt{wt}-(0.5w+0.866t)\sqrt{f}}{\sqrt{f}} \tag{6.1}$$

However, in some regions due to the range of precipitate sizes and varying local density, smaller inter-particle spacings were observed, as shown in Fig. 6.1. These are what we call "confined" regions.

Selected frames from an *in situ* TEM video from such a confined region are provided in Fig. 6.2. These images show the glide of matrix dislocations in the channels confined by β_1 precipitates. The images shown in Fig. 6.2 were recorded in the dark field condition with the diffraction vector parallel to $[10\bar{1}0]$ so that dislocations appear as bright lines. As the *in situ* video shows, the propagation of dislocations through the array of precipitates follows a four-step sequence from 1) initial pinning and bowing to 2) dislocation propagation within confined region to 3) dislocation pile-up and finally 4) shearing of blocking precipitates. As shown in Fig. 1c, with the indenter tip aligned approximately parallel to the $(\bar{1}014)$ plane the Schmid factor for basal and prismatic planes are calculated to have comparable values of 0.35 and 0.37 respectively. Since basal slip generally has a much lower critical resolved shear stress (CRSS) at room temperature than other slip systems in magnesium, dislocations observed in the *in situ* indentation experiments in TEM are basal dislocations, consistent with our earlier study (Chapter 4).

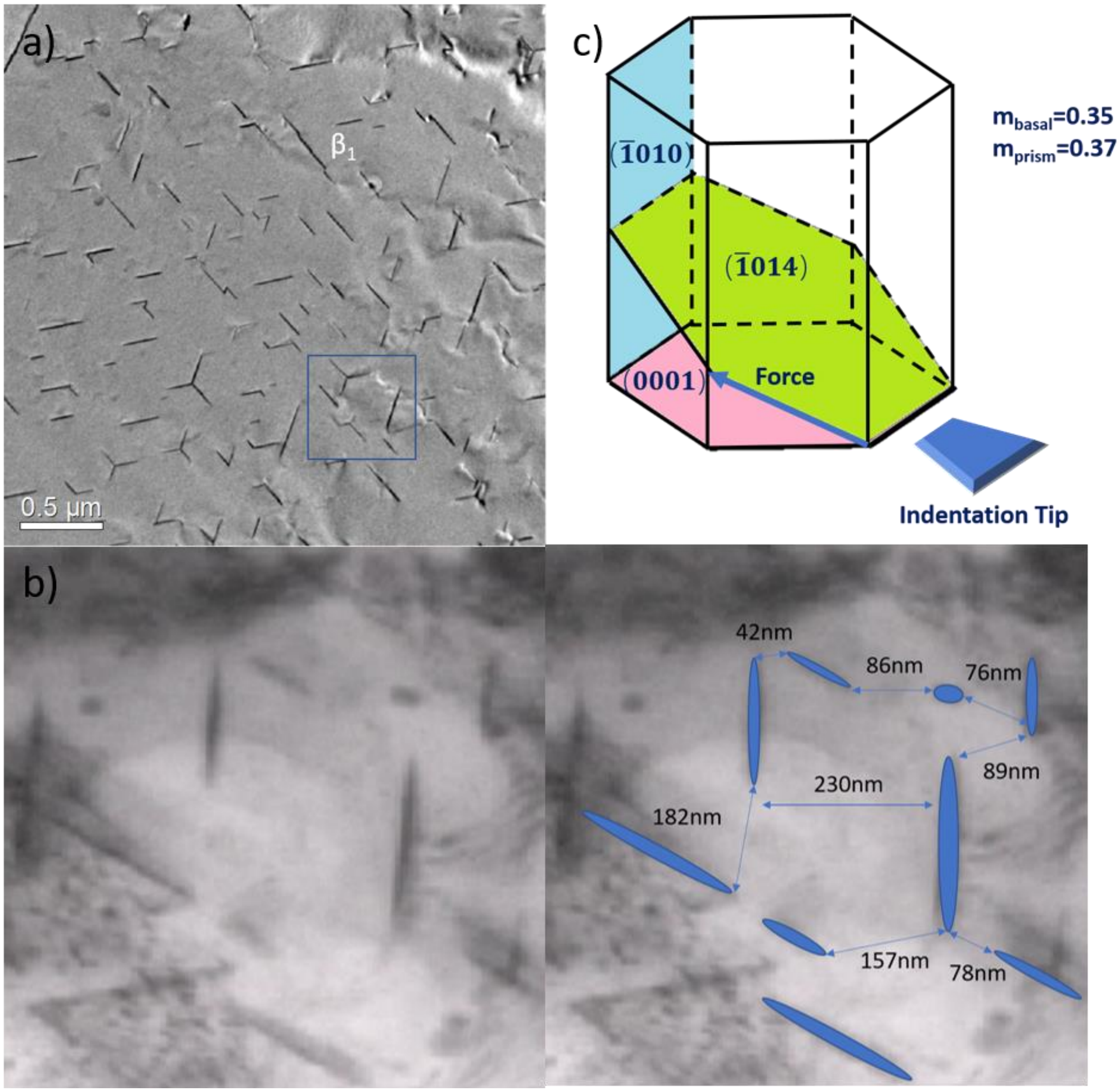

Fig. 6. 1 A coarse β1 precipitate microstructure results from 9 hours aging at 250oC in a). Interparticle spacings are generally large but the local region highlighted in the outlined box show a confined precipitates configuration. An image b) from the supplement in situ video in a region with a confined precipitate configuration. The analyzed precipitates are highlighted and the effective inter-particle spacings are marked. Both images were recorded with incident beam close to $[0001]$ direction. A schematic of the indentation set up is shown in c). The applied force is approximately 22o incline to the basal plane.

6.2.1 Initial pinning and bowing

The images extracted from the *in situ* straining video and their corresponding schematics in Fig. 6.2 show that the incoming dislocations get pinned by precipitates and bow out under the local stress to generate new dislocation segments (step 1 in the four-step process). When the incoming dislocation first contacts the precipitate it immediately moves to the pinning position by gliding along the precipitate interface as shown in Fig. 6.2 a) to b). A more detailed analysis of this interfacial glide mechanism can be found in Ref [73]. In order to maintain the continuity of dislocations, interfacial dislocations are introduced at the precipitate interface, marked as dashed lines in the schematics shown in Fig. 6.2. The dislocations are strongly bowed out suggesting a strong pinning effect from the interface. When the local stress is sufficiently large, as in Fig. 6.2 c) and d), the dislocation is able to bow out of the initial pinning position and glide into the matrix channel confined by precipitates. This process is somewhat analogous to the Frank-Read source in which the pinned dislocation segment lengthens itself under the applied shear stress. It should be noted in Fig. 6.2 d), that the leading dislocation detaches from the departure side of the pinning precipitate and then becomes anchored at the departure side of a second precipitate. The detachment process from the departure side seems to be very effective at hindering dislocation movement since in Fig. 6.2c this dislocation (see arrow) bows extensively prior to detaching from the precipitate. The abnormal hindering effect from departure side is also critical for dislocation pile-up in the following step. The dislocation that are pinned at the detachment point prevent the movement of incoming dislocations. This is discussed in the next section.

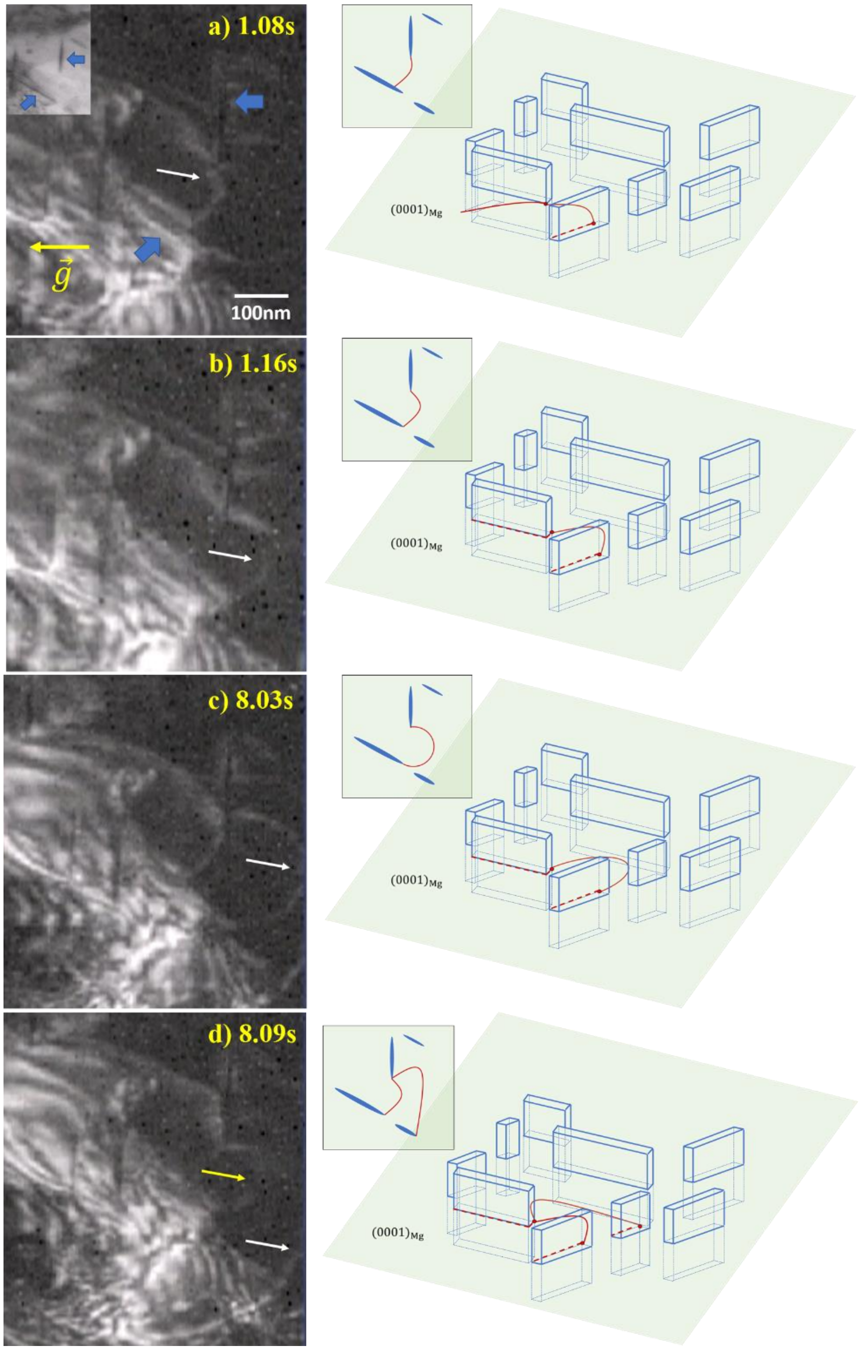

Fig. 6. 2 Image frames from the in situ straining video and corresponding schematics show initial pinning and a dislocation bowing out. The analyzed dislocation is marked with white arrow. The new incoming dislocation in d) is marked by yellow arrow. The video is recorded under diffraction vector $[\bar{1}010]$ shown in a).

6.2.2 Confined glide and pile-up of dislocations at precipitate interface

A group of incoming dislocations leads to a pile up and the trailing dislocations experience back stresses from the leading dislocations. This leads to a sluggish dislocation motion observed within the matrix channels confined by the surrounding precipitates. A dislocation pile-up forms at precipitate interfaces, over a time interval of 20s to 40s in the experiment. In Fig. 6.3, the analyzed dislocation (marked as 2) is in a position in between a leading dislocation (marked as 1) and an incoming dislocation (marked as 3). Due to the repulsive force from leading dislocations, the trailing dislocations on the slip plane appear to slow down as a pile-up forms at the precipitate interface. When the leading dislocation (segment 1) runs into the array of precipitates (the configuration on the top part of the schematic), its movement is significantly reduced because of the close spacing of the precipitates. On the other side, although the bottom part of segment 1 is able to thread through the precipitates on the right (Precipitate A), it seems that the precipitate departure side in Fig. 6.3 c) effectively prevents subsequent dislocation propagation resulting in a dislocation pile-up at Precipitate A. Although there is a large inter-particle spacing (250nm marked in Fig. 6.3c) for the detaching dislocation at the departure side, it is effectively pinned by Precipitate A. An abnormally strong pinning effect is observed for the detachment process.

With increasing applied strain, incoming dislocations enter the confined region at a faster rate than the escape rate from leading dislocations. Consequently, a clear dislocation pile-up is formed inside the confined region. The number of pile-up dislocations in Fig. 6.3 c) is six as marked by white arrowheads.

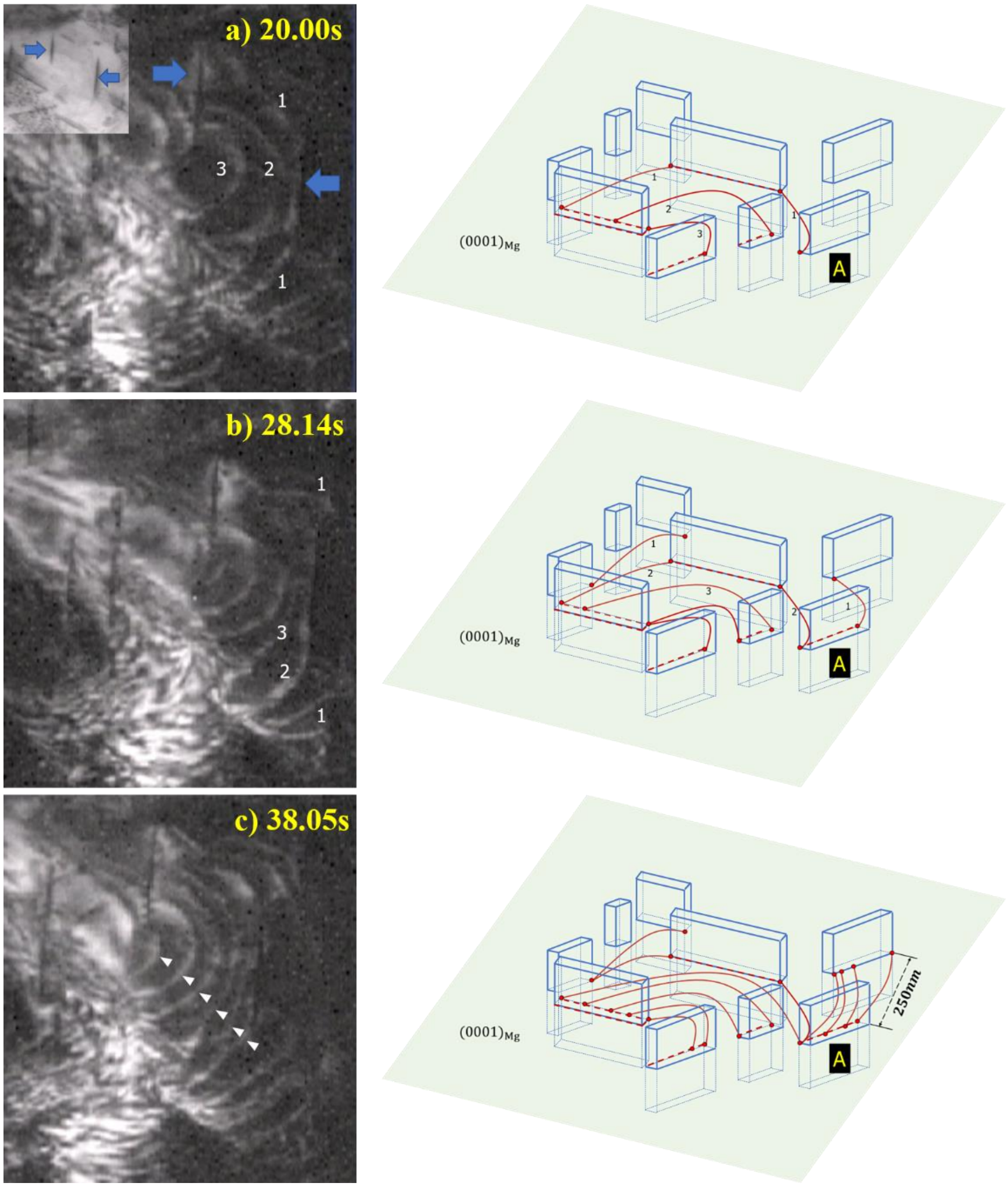

Fig. 6. 3 TEM images and corresponding schematics showing dislocation glide in the matrix channels confined by precipitates from a) to b) and dislocation pile-up in front of precipitate interface in c). A dislocation pile-up is also observed in the right bottom of c).

6.2.3 Dislocations overcoming the precipitate barrier

As the seventh dislocation enters the pile-up region in Fig. 6.4 b), the leading dislocation (marked as yellow arrow in Fig. 6.4 b) and c)) appears on the other side of the blocking precipitate (Precipitate C) with one end connected to the pre-existing dislocation and another one lying at the back of the blocking precipitate interface. We attribute this new dislocation on the back side of the precipitate to precipitate shearing. Similar phenomena occur several times at later stages and eventually the dislocations that are constricted by the precipitates on the right top of the image are able to overcome the precipitate barrier as well. As in Fig. 6.4 d), the marked dislocation bypasses the top blocking precipitate (Precipitate D outlined by yellow line). The mechanism involved in this process is deemed to be the same as in Fig. 6.4 c). In the final stage of the *in situ* video, many dislocations rapidly overcome the blocking precipitate.

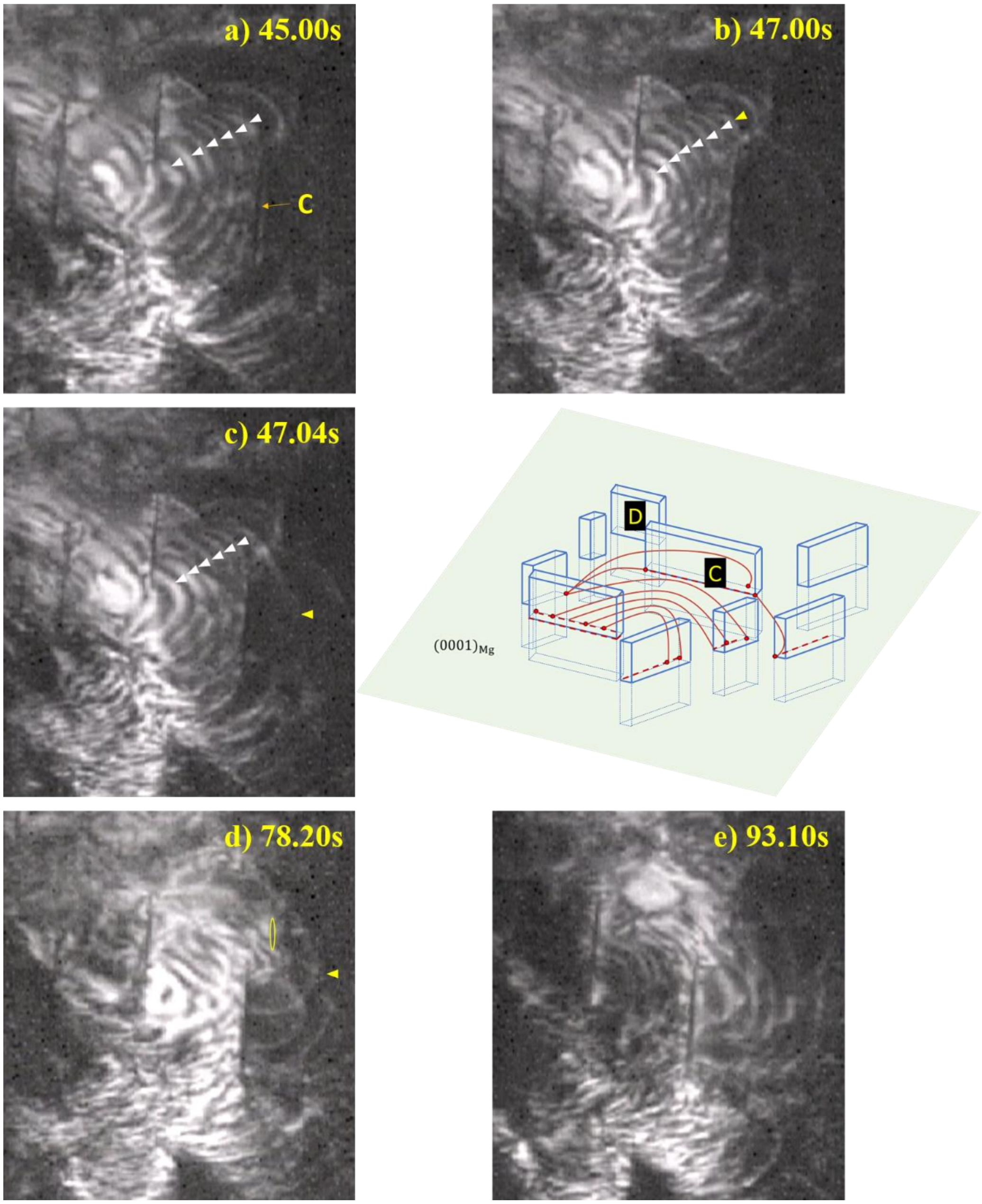

Fig. 6. 4 Images show how dislocations overcome the blocking precipitates. From a) to c), the number of piled-up dislocations is tracked with white arrowheads. The yellow triangle in b), c) and d) show that the leading dislocation escaping from the confined region in e).

6.2.4 Post-mortem TEM characterization

HAADF-STEM images were taken from compressed samples (total strain 5%) to supplement the *in situ* straining results. Fig. 6.5 shows the precipitate morphology before and after *post-mortem* compression. From Fig. 6.5 a) to b), β_1 precipitates are aligned along the $[0001]$ direction and exhibit a continuous interface $\{\bar{1}12\}_{\beta_1}//\{1\bar{1}00\}_{Mg}$ with the magnesium matrix. In Fig. 6.5 c), the annular bright field image (ABF) shows the impingement of basal dislocations on β_1 precipitates. Some precipitate interface discontinuities are seen in the highlighted box. The enlarged HAADF image Fig. 6.5 d) shows a clear offset along a basal slip trace. These offsets are readily visible in the deformed samples and usually combine with another offset in an adjacent precipitate such as that shown in the inset image in Fig. 6.5 c). This phenomenon indicates an intensive slip localization along one slip plane and appears to shear several precipitates in a row. This phenomenon is presumably related to the presence of a dislocation pile-up.

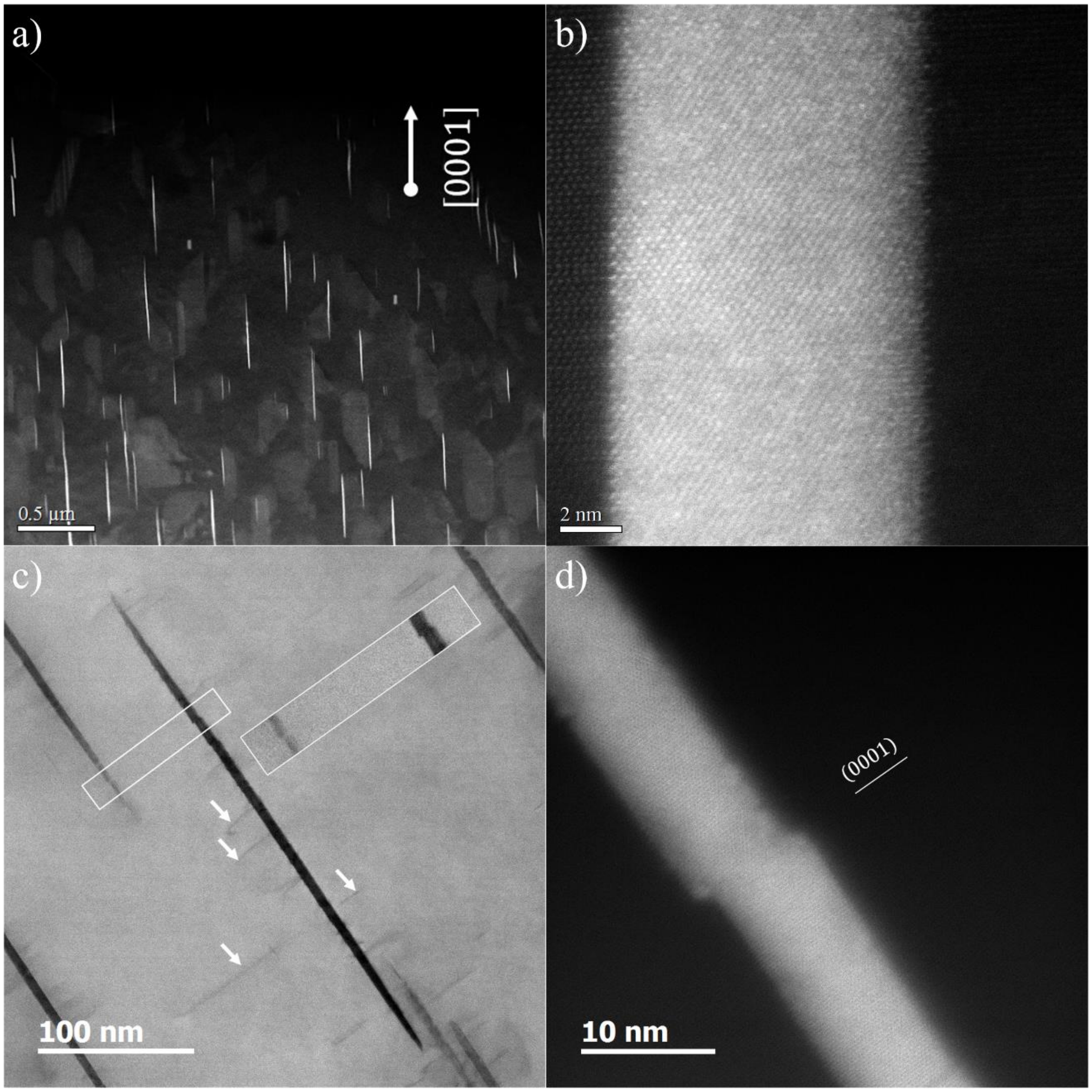

Fig. 6. 5 Undeformed samples show straight precipitates with an intact interface with the matrix in a) and b). Images c) and d) are taken from samples compressed 5% showing that the precipitate is cut by basal dislocations leaving an offset at the sheared interface. Image c) is an annular bright field (ABF) image and the thin dark lines (marked with arrows) are dislocations impinging on the precipitate. The inset in c) is a high magnification image of interface offsets. All images are viewed from $[1\bar{2}10]$ direction.

6.2.5 Estimation of critical shear stress for slip transmission across a β_1 precipitate

Interactions between dislocations and coherent precipitates include two forms: hard-contact interactions and soft-contact (or diffuse) interactions [74]. In precipitates that can form superlattice ordering, the hard-contact interactions refer to atomic-order strengthening that occurs when dislocation shearing of precipitates induces antiphase boundaries inside the precipitates. The soft-contact interactions are size-misfit and modulus misfit interactions. As hard-contact contributes the primary resistance for dislocation cutting through the precipitates, we focus on atomic-order strengthening to estimate the critical resolved shear stress for slip transmission across a β_1 precipitate.

The Mg matrix and β_1 precipitates have coherent lattices with the orientation relationship as $[\bar{1}11]_{\beta_1}//[11\bar{2}0]_{\mathrm{Mg}}$ and $(110)_{\beta_1}//(0001)_{\mathrm{Mg}}$, and the $\frac{1}{4}[\bar{1}11]$ lattice vector in the β_1 precipitate matches the Burgers vector $\frac{1}{3}[11\bar{2}0]$ of basal <a> dislocation in Mg matrix in terms of both magnitude and direction. As shown in Fig. 6.6, a $\frac{1}{4}[\bar{1}11]$ Burgers vector generates an APB in the β_1 precipitate since it only consists ¼ of a translational-symmetry vector in the β_1 lattice. Once a consecutive dislocation glides through, it adds another $\frac{1}{4}[\bar{1}11]$ shift to the precipitate and induces another APB. The whole energy landscape along <111> shifting requires nudged elastic band (NEB) calculations to handle energy barriers. As our interest centers on APB energies rather than energy barriers, we used MD calculations based on MEAM potential [75, 44] to confirm the shape of the energy landscape along a <111> shift, and only applied DFT calculations for configurations near the local/global minimum in the energy landscape. As shown in Fig. 6.6b, in the energy landscape sketch the local minimum energies correspond to APB energies, and our DFT calculations show the APB energy γ_{apb} is 0.0158 eV/Å^2 (253.1 mJ /m^2) for $\frac{1}{4}[\bar{1}11]$ shift and 0.0103 eV/Å^2 (165.0 mJ /m^2) for $\frac{1}{2}[\bar{1}11]$ shift.

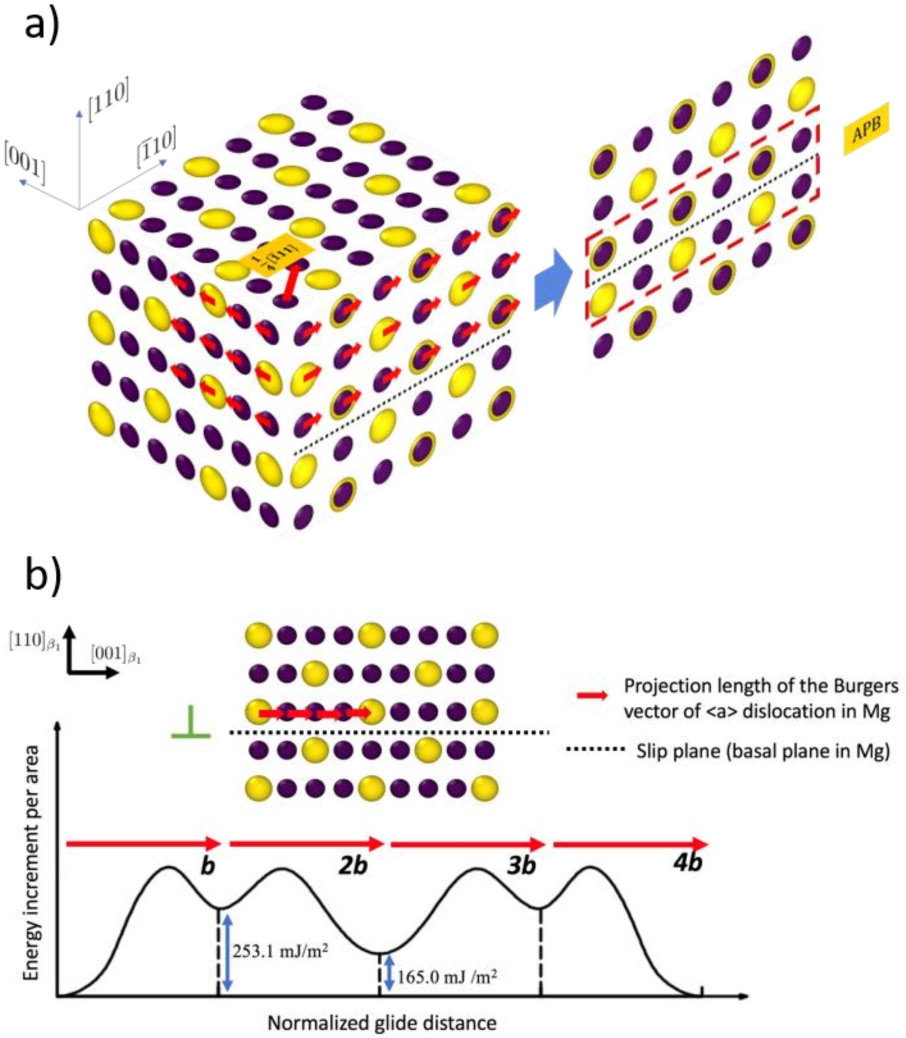

Fig. 6. 6 a) Illustration of the APB generated by $\frac{1}{4}[\bar{1}11]$ Burgers vector in the lattice of a β1 precipitate. Purple and yellow atoms stand for Mg and Nd, respectively. b) Sketch of energy increment when <a> basal dislocations consecutively cut the lattice of a β1 precipitate.

For only one dislocation cutting the precipitates, based on average spacing and dislocation bowing model from Ardell, A.J. [37], the critical shear stress to cut through a β_1 precipitate is estimated by

$$\tau_c = \frac{\gamma_{apb}}{b}\left(3\pi^2\gamma_{apb}f<r>/(32\Gamma)\right)^{1/2} \tag{6.2}$$

where the γ_{apb} is ABP energy per unit area for 1/4<111> shift, *f* is volume fraction of precipitates and <*r*> is the average radius of precipitates and Γ is the dislocation line tension. The volume fraction *f* was measured from TEM micrographs as 0.013 and the average radius is calculated by $\sqrt{w * t}$, where *w* is the width of precipitate (130 nm) and *t* is the thickness of precipitate (10 nm). The line tension, Γ, depends on dislocation characteristics. For the dislocation line tension in hexagonal crystals, we adopt the anisotropic elasticity formula Eq. 6.3 [76].

$$\Gamma(\theta) = \frac{b^2}{4\pi}[K_e sin^2\theta + K_s cos^2\theta + 2(K_e - K_s)cos2\theta] ln\frac{R}{r_0} \tag{6.3}$$

The line tension, Γ(θ), is a function of the angle θ between the dislocation line and the Burgers vector.

Furthermore, as shown in Fig. 6.6, the influence of the second, third, and forth dislocation on CRSS are also profound. For example, when a second dislocation cuts through the precipitates, it decreases the APB energy and thus the APB force assists the dislocation cutting through the precipitates. The multiple dislocation effects are difficult to calculate due to statistical distribution for dislocation-dislocation spacing and different extent of bowing. We consider relatively weakly coupled dislocations. The balanced forces acting on a group of four dislocations satisfy the equation

$$4\tau b = \gamma_1\frac{d_1}{L_1} + (\gamma_2 - \gamma_1)\frac{d_2}{L_2} + (\gamma_3 - \gamma_2)\frac{d_3}{L_3} + (\gamma_4 - \gamma_3)\frac{d_4}{L_4} \tag{6.4}$$

Where γ_i (i=1,2,3,4) denotes the APB energy after the i-th dislocation cuts the precipitate, d_i/L_i denotes the fraction of the i-th dislocation that exists inside precipitates. Due to lattice inverse symmetry along <111>, we have $\gamma_3 = \gamma_1$. Based on the energy landscape in Fig 6.6, we apply the assumption that the first and third dislocation bow out due to resistance and the second and forth dislocation remain straight. Combining the APB energies calculated by DFT, the CRSS for four loosely coupled dislocations can be calculated by

$$\tau_{c4} = \frac{\gamma_1}{4b}[(3\pi^2(\gamma_1)f < r >/32\Gamma\,)^{\frac{1}{2}} - f] + \frac{\gamma_1 - \gamma_2}{4b}[(3\pi^2(\gamma_1 - \gamma_2)f < r >/32\Gamma\,)^{\frac{1}{2}} - f] \qquad (6.5)$$

Where γ_{apb1} and γ_{apb2} are ABP energies per unit area for 1/4<111> shift and 1/2<111> shift respectively. Γ is the dislocation line tension and f is precipitate volume fraction. The calculation results for dislocation line tension, CRSS for a single dislocation, and CRSS for four loosely coupled dislocations based on <a> dislocation of different mixed angles θ ranging from 0 (for pure screw dislocations) to 90^{o} (for pure edge dislocations) are shown in Table 6.1.

Table 6. 1: Line tension (Γ) and critical shear stress (τ_c) for dislocations with different angles, θ, to cut through β_1 precipitate according to Equation (6.2, 6.5)

θ [^{o}]	0	22.5	45	67.5	90
Γ [eV/Å]	0.720	0.645	0.464	0.283	0.208
τ_c [MPa]	250	264	310	398	465
τ_{4c} [MPa]	72	76	91	117	137

6.3 Discussion

In the *in situ* straining experiment, the incoming dislocations were observed to lengthen under the applied strain and enter a confined space where they are forced to interact. The dislocations enter the confined space and pile-up behind the leading dislocations until it can shear the blocking precipitate. From Fig. 6.3 and 6.4, the strong pinning from the precipitate departure side is essential to keep dislocations within the confined region. The detaching dislocations provide a strong back force for the trailing dislocations regardless of their inter-particle spacing. Subsequently, successive trailing dislocations are forced to form pile-ups within the confined region. The mechanism responsible for this abnormally strong detachment process is still under investigation. It is suspected that some non-basal dislocations reaction occurs at the departure side resulting in sessile dislocations. Combining with the found cross-slip mechanism (Chapter 5), it was hypothesized certain dislocation reaction or cross-slip activity attribute to the phenomenon. The schematic in Fig. 6.7 shows a hypothesized cross-slip mechanism occurs at precipitate departure side.

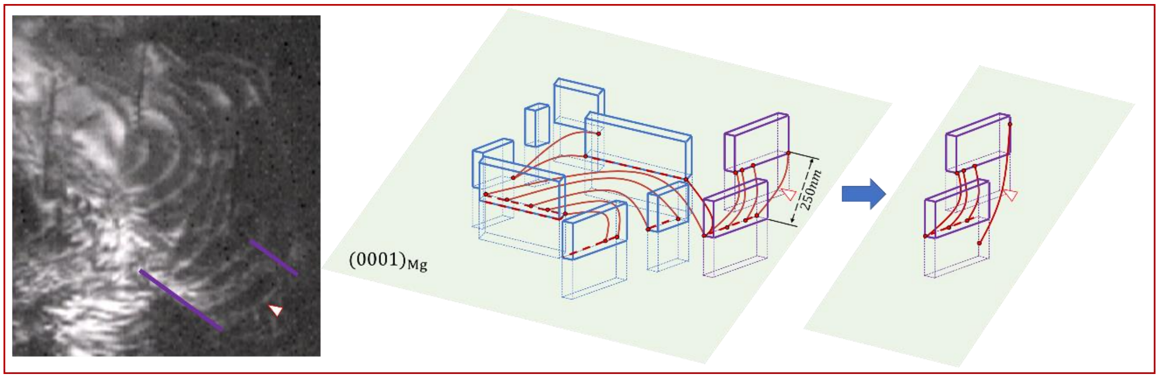

Fig. 6. 7 Image from in situ video (viewing along [0001] direction) and its corresponding schematic. Dislocations appear as bright line in the experiment and red line in schematic. Precipitates are represented as block (blue and purple) in schematic. The arrowed dislocation is pinned at departure side of purple highlighted precipitates. The rightmost schematic shows the hypothesis that dislocation cross-slip at precipitate departure side.

The observations from the *in situ* straining experiments (Fig. 6.4) enabled us to measure the critical size of the pile-up for overcoming the barrier to slip due to the presence of a β_1 precipitate. In this particular region, once the seventh dislocation enters the pile-up, the leading dislocation is observed to quickly escape from the region. Dislocation cutting through precipitate is the most plausible mechanism that accounts for this phenomenon. Although there is lack of direct evidence of precipitate cutting from the *in situ* video, the *post-mortem* study shows that precipitates are sheared by basal dislocations. It is clear that a single dislocation that glides along precipitate interface or loops around does not cut through the precipitate. Simulation results also suggest the required stress to cut through a β_1 precipitate is at least 300 MPa, which is unlikely to be achieved by a single dislocation. We attribute the cutting offset to slip localization (planar slip) combined with the presence of a dislocation pile-up. We hypothesize that when a critical pile-up stress is achieved the dislocation pile-up overcomes the blocking precipitate by shearing across the interface. When successive dislocations shear the precipitate C in Fig. 6.4 e), it is no longer an obstacle to subsequent dislocations on this slip plane. This dislocation pile-up and precipitate cutting process is analogous to slip transmission across planar interfaces [77]. This is somewhat similar to pile-ups at grain boundaries.

In this study, the *in situ* video shows a Frank-Read-type source that generated dislocations that formed a single-ended pile-up at the β_1 precipitate facets. The number of allowed dislocations of single-ended pile-up [78] can be described as

$$N = \frac{\pi\sqrt{1-\nu}d\tau}{Gb} \tag{6.6}$$

where υ is the Poisson's ratio of matrix (0.35), G is the shear modulus of matrix (16.5GPa), b is the Burgers vector of the basal dislocation (0.32nm), τ is the applied shear stress from external force and d is the diameter of the confined space which is equal to 230nm in this case described by Fig. 6.4 as measured in Fig. 6.1 b).

With rearrangement of Equation (6.6), the local shear stress τ due to the pile-up can be determined to be approximately 63MPa. For comparison, the required shear stress to generate the dislocations bowing out a certain gap is given by the Frank-Read model [79],

$$\tau_{F-R} = \frac{Gb}{\lambda} \tag{6.7}$$

where λ is the gap distance between two pinning points. For a 182nm gap (measured in Fig. 6.1 b), a shear stress of only 29 MPa shear stress should bow dislocations inside the confined region.

However, the local applied shear stress increases to 63MPa with the dislocations pile-up. The pile-up mechanism significantly improves the local strength level and indicates a higher strengthening comparing to dislocation looping.

The critical shear stress for shearing a β_1 precipitate is estimated by the stress on the leading dislocation $N\tau$. For N=7, the critical shear stress τ_c for shearing β_1 precipitate is 441 MPa. The experimental result is consistent with simulation result given in Table 1, in which the critical stress to shear a precipitate is estimated to range from 250-465MPa depending on the character of the dislocation. The dislocations in the pile-up are expected to have both screw and edge components, evident from the curved dislocation lines observed in the *in situ* experiment. Thus, 441 MPa is a reasonable estimation for a mixed dislocation to shear a β_1 precipitate. This analysis indicates a very high stress at the front of the pile-up. As discussed previously, the detachment of the dislocation from the precipitate (trailing edge) shows a significant pinning which appears to restrict dislocation bowing despite the fact that the leading dislocation experiences a high stress. Although the underlying detachment mechanism is unknown, the strong pinning effect from the precipitate trailing edge is essential to the pile-up and set it apart from Orowan looping. The classic Orowan looping states the strengthening depends on the interparticle spacing. However, this study shows the non-interconnected and relative coarse precipitate array is capable of trapping dislocations in a very high stress condition, which is not expected from the Orowan looping mechanism.

6.4 Conclusions

The *in situ* straining in TEM of dilute, over-aged Mg-Nd alloys revealed that dislocation glide in matrix channels confined by planar, prismatic β_1 precipitates leads to dislocation pile-ups and ultimately precipitate shearing. The *in situ* experiment shows that the formation of dislocation pile-ups is due to an unbalance between the number of dislocations entering and escaping these confined regions. During the formation of a dislocation pile-up, the strong pinning effect from the interface detachment process is essential to prevent dislocations from escaping out of the confined region. The strong pinning is suspected due to the dislocations cross-slip as described in Chapter 5.

Combined with the *post-mortem* characterization that showed basal slip offsets along the precipitate interface, it is hypothesized that the dislocation pile-ups ultimately overcome the blocking precipitate by shearing across the interface. DFT calculations confirm that the precipitate shear stress estimated from *in situ* results give a reasonable estimate of the β_1 precipitate critical shear stress.

CHAPTER 7

β_1 Precipitate Deformation in Mg-Nd Alloy

7.1 Introduction

Single dislocation shearing mechanisms in β''' precipitates have been characterized in Chapter 5 and been reported in literature [66, 67]. On the other hand, the β_1 precipitates that form during overaging are generally regarded as impenetrable precipitates for single dislocations, and are sheared (Chapter 6) when dislocation pile-ups form. The β_1 precipitates shearing phenomenon was observed in MN11 alloy as well [31]. It was pointed out by Cepeda-Jiménez *et al.* that the ease of β_1 precipitate shearing leads to the low precipitation hardening in MN11 alloy. *In situ* synchrotron X-ray diffraction study on Mg-Nd alloys [24] observed a very high micro-strain in β_1 precipitates, which is significantly larger than the micro-strain in the Mg matrix. The high strain in β_1 precipitates indicates certain degrees of precipitate structural change during the deformation. In Mg-0.3Ca-1.0In-0.1Al-0.2Mn (at.%) alloy, the precipitate shearing mechanism was observed to provide an inferior strength hardening compared with Orowan looping [80].

However, a closer look at the image of sheared precipitates in [31] and [80], revealed that the precipitates were not clearly sheared along the basal plane in tensile samples, and were continuously connected across the slip band. The continuous morphology of the precipitate across the slip band suggests that a deformation mechanism different from the classical precipitate shearing seems to be involved. The structure of the deformed precipitate and the details of the shearing mechanism are of great importance since it is critical to understand their influence on local strengthening or softening. In this chapter, we use both conventional TEM and high resolution HAADF-STEM images to characterize atomic structure change precipitates after tensile and compressive deformation.

7.2 Results

7.2.1 Precipitate shearing in tensile samples

Fig. 7.1 shows an extensive slip band extending across the sample after a tensile test. The sample was pulled to failure with a total engineering strain of around 18%. The sample is severely deformed as the diffraction contrast varies across these images and, moreover, the basal slip trace is curved as it propagates throughout the images. This can be seen in Fig. 7.1 in that the yellow dashed line at the top image is not parallel to the continuation of this image in the bottom image. In the TEM foil, the slip band was observed to extend from a grain boundary to a hole in the electropolished sample. In Fig. 7.1, many images are omitted between the two ends. The total length of the slip band is estimated to be at least 60µm, a length scale that is close to the sample grain size (165µm).

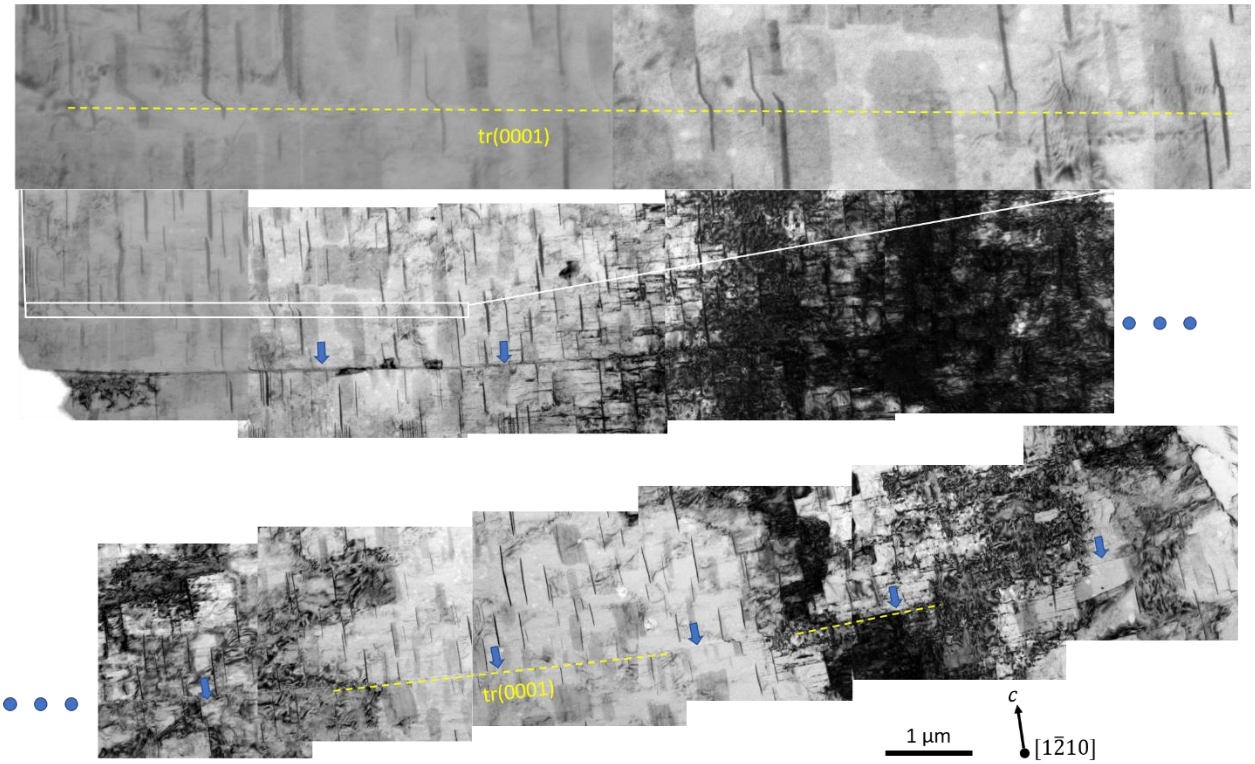

Fig. 7. 1 TEM bright field images show extensive basal dislocations slip activity in the failed tensile sample. Blue arrows track the trace of the slip activity. The white box shows another slip concentration without a basal trace left behind and which is provided at a higher magnification in the inset image. The incident electron beam is parallel to $[\mathbf{1\bar{2}10}]$.

It is commonly observed that the β_1 precipitates are deformed not only along the trace but also other regions such as the white box in Fig, 7.1. However, the precipitates along the trace show a significant shift along the basal plane. In Fig. 7.2, the HAADF-STEM images show an interesting shearing phenomenon along the slip trace. It is noticeable that the shearing is not confined to a single slip plane. As shown in Fig. 7.2 b), the highlighted precipitate is appears separated by basal dislocation shearing but actually remains connected by a severely deformed layer. The atomic structure of such a layer is shown in HAADF-STEM image in Fig. 7.2 c) and Fig. 7.3. As marked by double headed arrows in Fig. 7.2 c), the width of individual plane is almost identical in the deformation layer and close to the original precipitate thickness, whereas the shift between each layer is not constant.

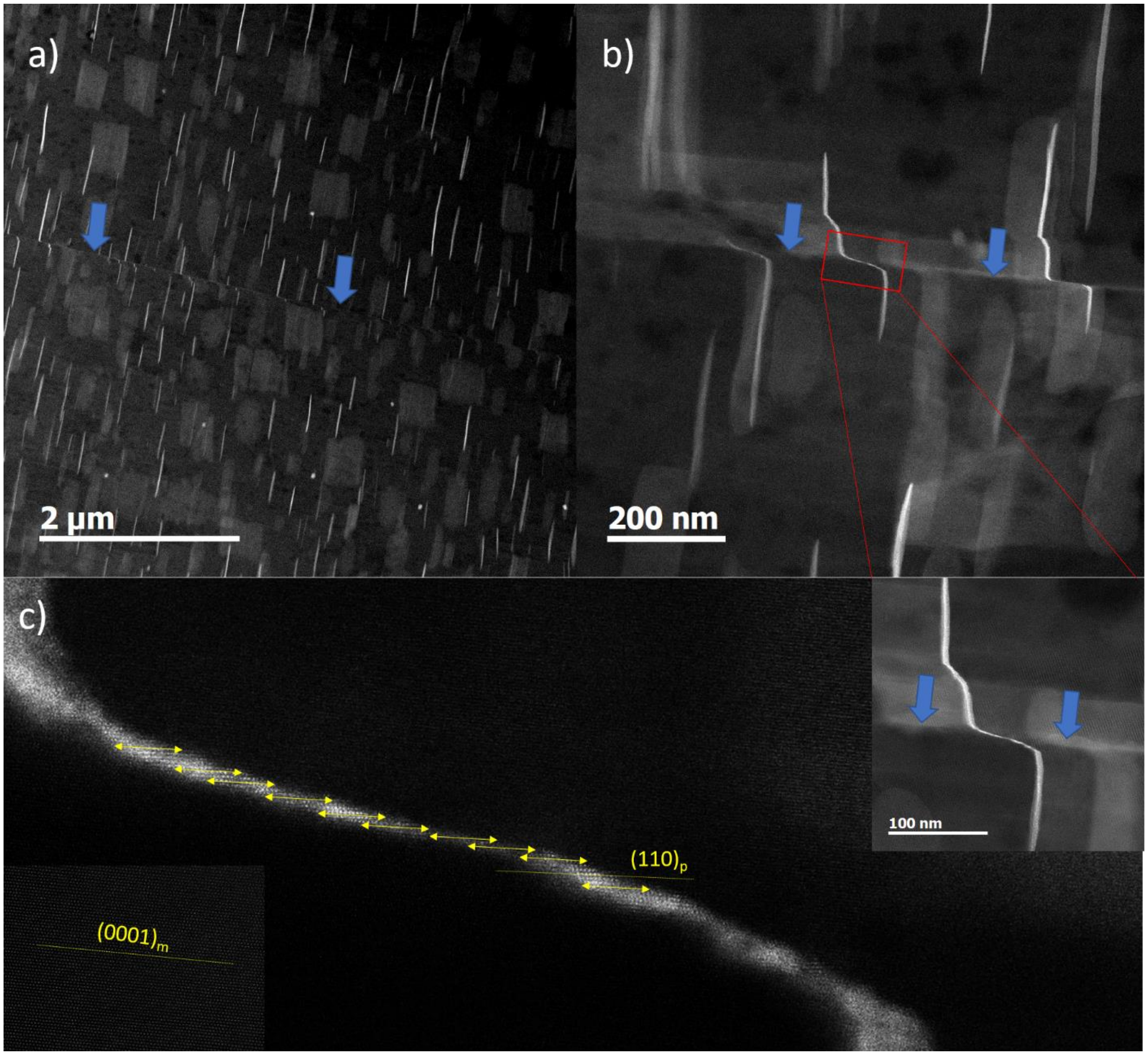

Fig. 7. 2 HAADF-STEM images on shearing events along slip trace. The left lower inset in c) is the enlarge image of local matrix structure. The yellow dash lines indicate the slip plane direction in precipitate (110)p and in matrix (0001)m. Double headed arrows aligned with (110)p have same length in image c). The blue arrows locate the slip trace. The incident electron beam is parallel to $[\mathbf{1\bar{2}10}]$.

Due to the highly localized micro-strain along the slip trace, the atomic structure of the deformation layer is not fully revealed, whereas at certain areas the Z-contrast from HAADF-STEM shows the positions of Nd atoms. The Nd atoms in each $(110)_p$ slip plane show an equal spacing between each other, suggesting a periodicity within the plane. However, between these planes, the Nd atom positions suggest they are not maintaining a perfect β_1 precipitate atomic structure but shuffling between each slip planes, presumably due to the distortion produced by the intense slip band activity.

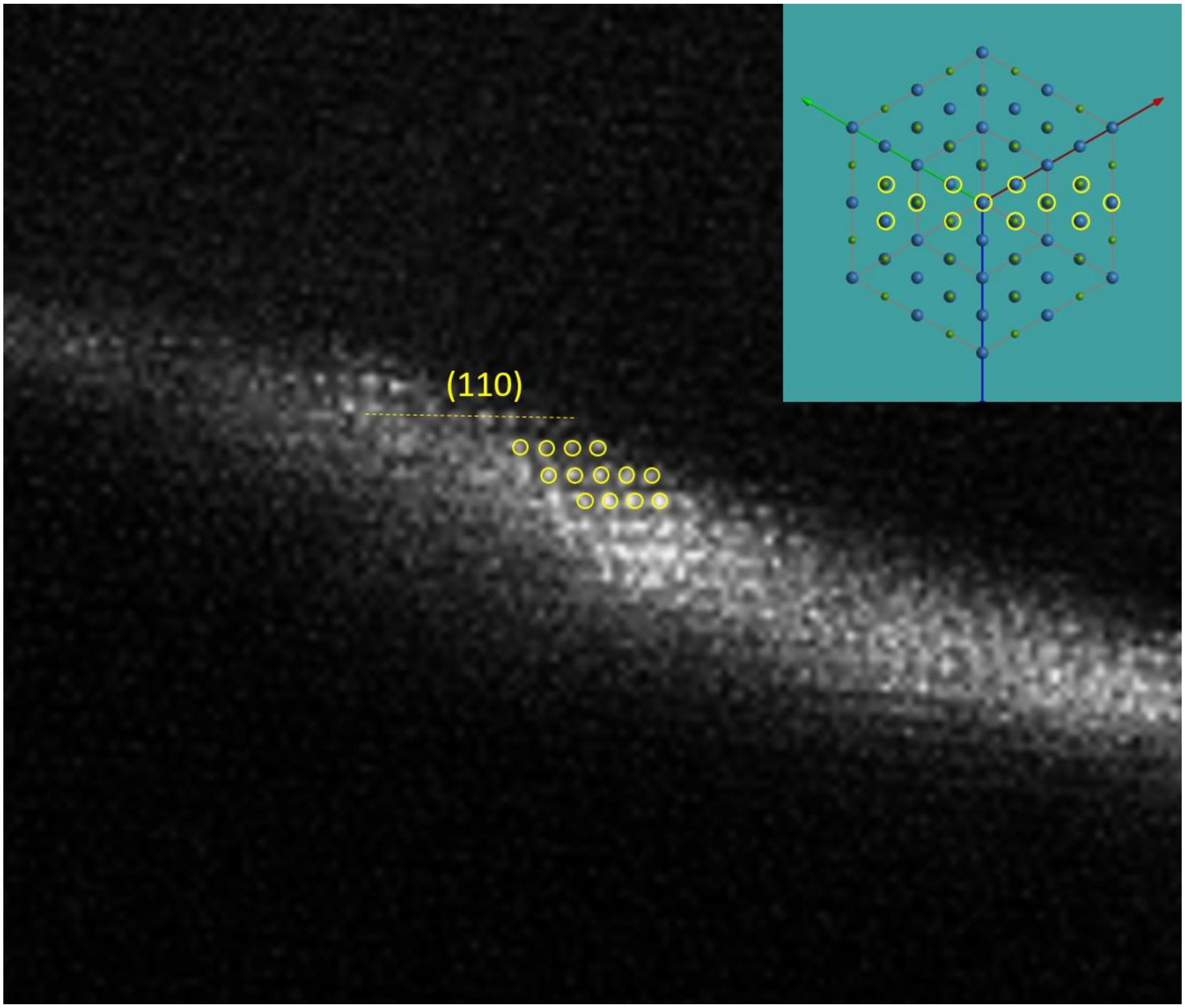

Fig. 7. 3 Atomic structure of deformation layer from region of Fig. 7.2 c). The inset shows the perfect β_1 precipitates atomic structure without deformation. The Nd atoms are highlighted with yellow circles.

These atomic shifts are ubiquitous throughout the sample and can be readily observed in Fig. 7.1 within the white box and in other locations. The dislocation pile-up concentration intensity is reduced as dislocations propagate in the sample. As shown in the white box in the top image of Fig. 7.1, the shift within the precipitates is gradually reduced from left to right. The same trend is observed along the observed slip trace where the precipitate shift decreases from the left hole to the right grain boundary. Judging from the shape and size of the hole in the Fig. 7.4 a), the hole is suspected to be a particle dispersoid from casting process. As shown in Fig. 7.4 d), an aggregated dispersoid is observed in a solutionized sample. The Energy Dispersive Spectroscopy (EDS) analysis shows it has a significant amount of Si and a trace amount of Fe. Such high melting point particles are difficult to dissolve during the solution heat treatment and might be etched out by electropolishing during sample preparation. It is reasonable to assume that the extensive slip concentration initiates from the dispersoid particle and is terminated by the grain boundary.

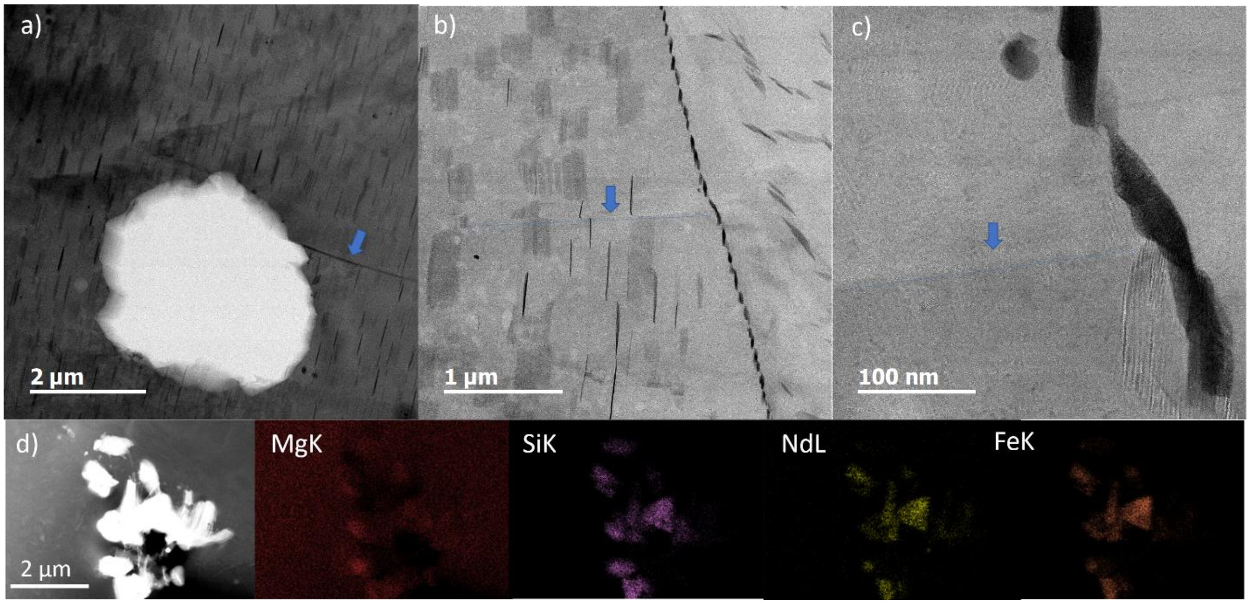

Fig. 7. 4 a)-c) ABF-STEM images of slip trace at its two ends. The blue arrows mark the slip trace. An aggregated dispersoid is characterized by EDS in image d).

7.2.2 Deformed precipitates in compressive samples

Compressive samples deformed to a total strain of 3% show an additional deformation feature for β_1 precipitates as shown in Fig. 7.5 a). Most of precipitates are deflected from their original straight shape. A closer look at deformed Precipitate 1 in Fig. 7.5 b), the HAADF-STEM image shows that the precipitate undergoes multiple fragmentation with a high frequency of serrations on both sides. Such serrations are also observed in a shear-band-free Precipitate 2 (Fig. 7.5c). These serrations are commonly observed in compressive samples but absent from tensile samples.

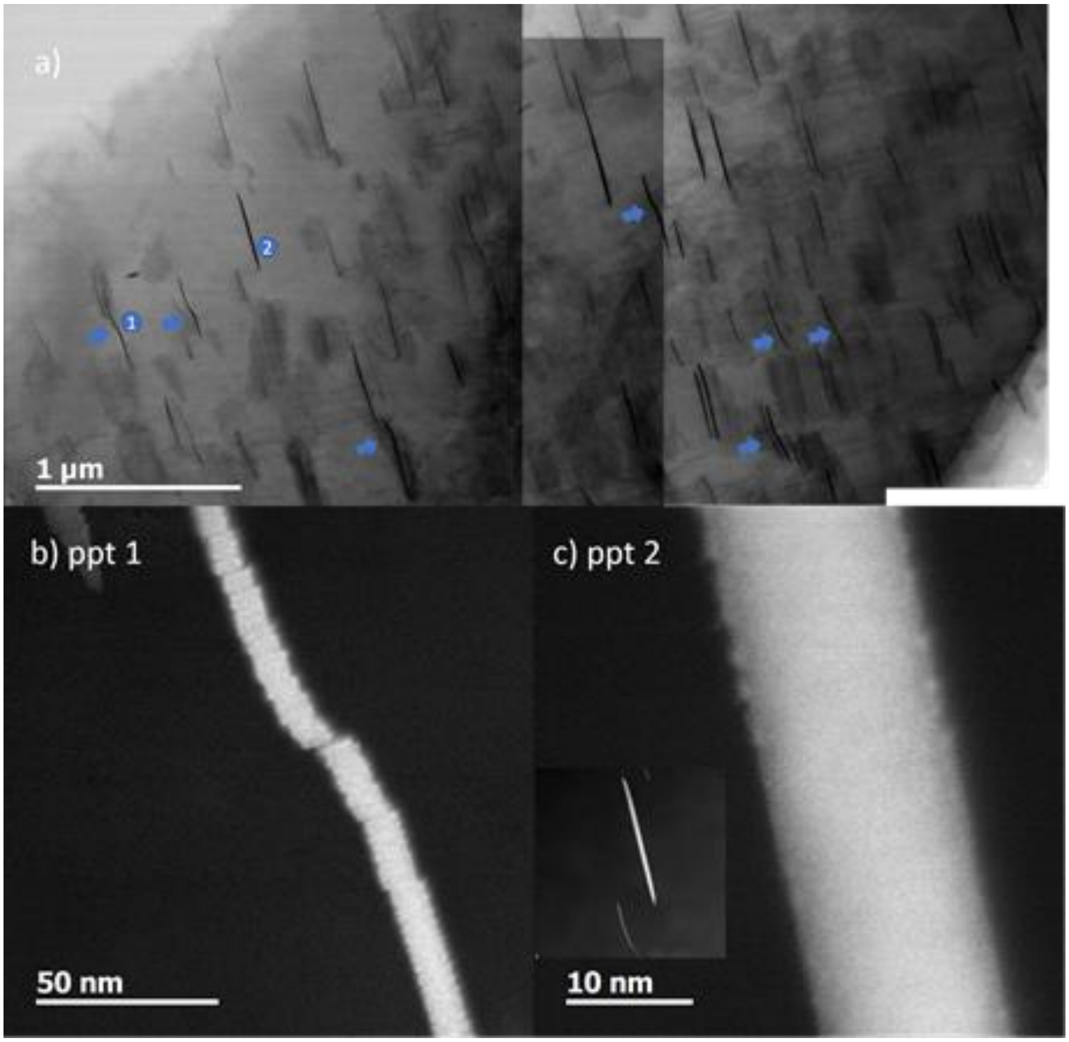

Fig. 7. 5 Overview of β_1 precipitates deformed in the compressive sample. The blue arrows mark deformed precipitates. Precipitate 1 and 2 in image a) are characterized by HAADF-STEM images in b) and c), respectively. Electron beam is parallel to $[\mathbf{1\bar{2}10}]$.

Compressive stress along the c-axis plays a critical factor to determine the precipitate deformation behavior. Although it is not feasible to extract the exact stress state of this sample, a compressive contraction twin observed in this grain (Fig. 7.6 a)) suggests a high compressive stress along the c-axis. In contrast, in Fig. 7.6 b), another observed grain with a different orientation from the same compressive sample does not show any sign of precipitate deformation.

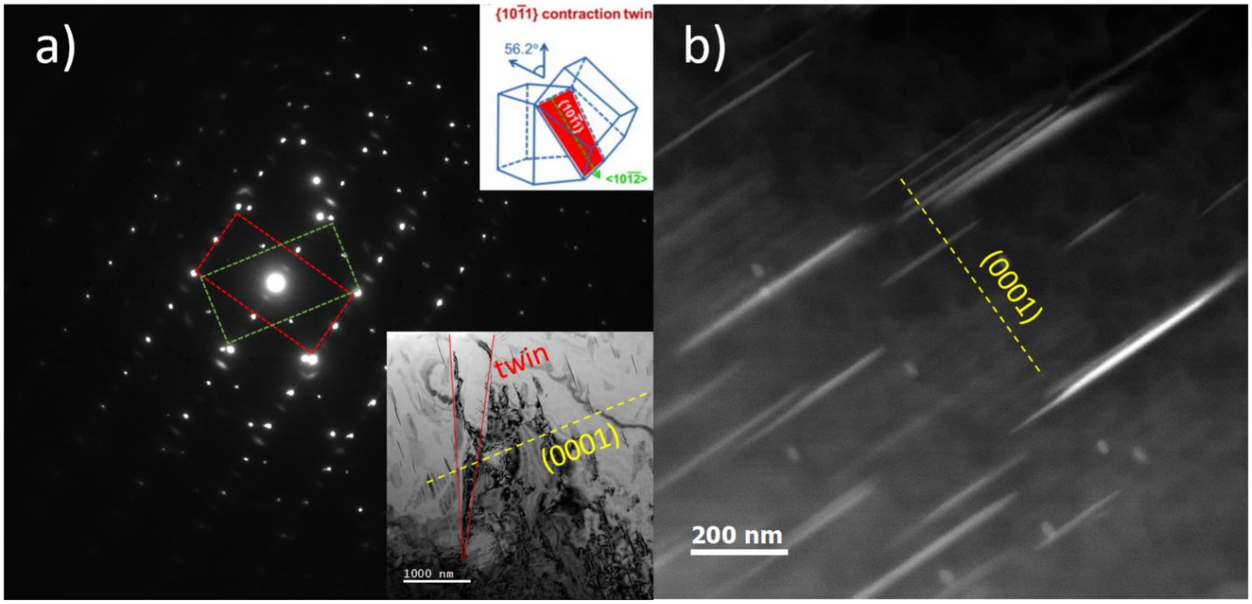

Fig. 7. 6 The SAD pattern shows the contraction compressive twin in this sample and image b) is the HAADF-STEM image of another grain with no significant precipitate deformation.

The precipitates shearing details in compression are different from tensile samples in another significant way the observation of rotated fragments. In a compressive sample deformed to a total strain of 5%, basal dislocation slip concentration was observed to transmit through an array of β_1 precipitates, producing a morphology similar to that reported by Cepeda-Jiménez *et al.* [31]. It is shown in Fig. 7.7 a) inset that β_1 precipitates are sheared by basal dislocations but, different from tensile sample in Fig. 7.7 b) and c), there are fragmented precipitate components rather than a smooth connection. The black dash lines in Fig. 7.7 a) that mark the precipitates upper sheared surface do not align with each other or with the basal plane. Furthermore, there is not even a sharp facet for the lower sheared surface in Fig. 7.7 a). The results suggest that the interfaces of the rotated fragments are not only come from shearing but also related to compression and potentially involve brittle fracture.

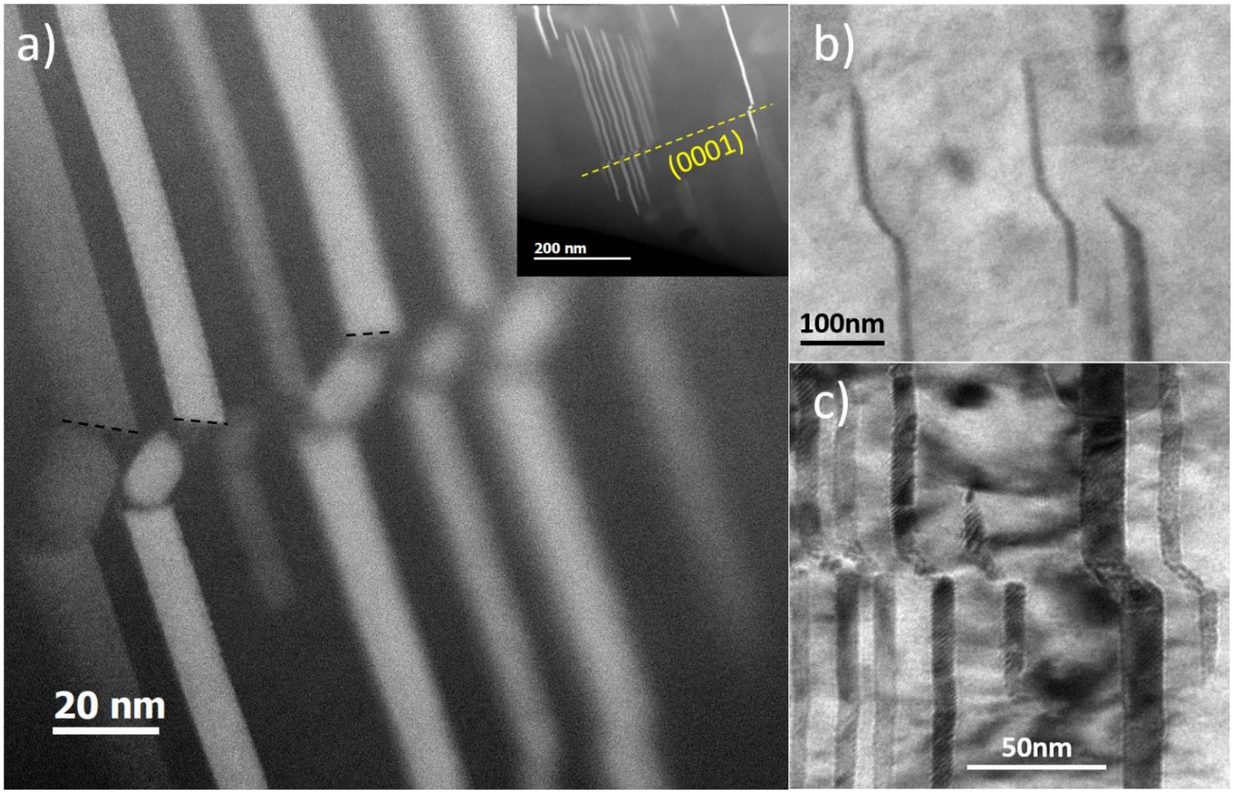

Fig. 7. 7 HAADF-STEM image a) shows the deformed β_1 precipitates structure after compression to 5% total strain. As in tensile samples, image b) shows the deformed precipitates in Fig. 7.1 white box and image c) is reprinted from Cepeda-Jiménez et al. work [31]. The black dash lines indicate the precipitate fragmentation surface.

An atomic resolution HAADF-STEM image reveals the structure of a precipitate shear surface, as shown in Fig. 7.8. An irregular interface with facets on different planes marked by yellow dash line is observed in Fig. 7.8 a). The majority of shearing interfaces are parallel to a basal plane with some steps connecting these shearing interfaces. As seen from the image Fig. 7.8 b), the precipitate shift in image Fig. 7.8 a) caused a fragment or potentially a fracture in the same precipitate which is characterized in Fig. 7.8 c). Instead of a shearing interface parallel to basal planes, the deformed precipitate component rotates within the matrix. As shown by slip trace in

Fig. 7.8 c), a rotational angle of approximately 12.5° is measured from the high resolution HAADF-STEM image. The fragment in Fig. 7.8 c) does not show any sign of a shearing shift, suggesting a rotational strain induced fracture.

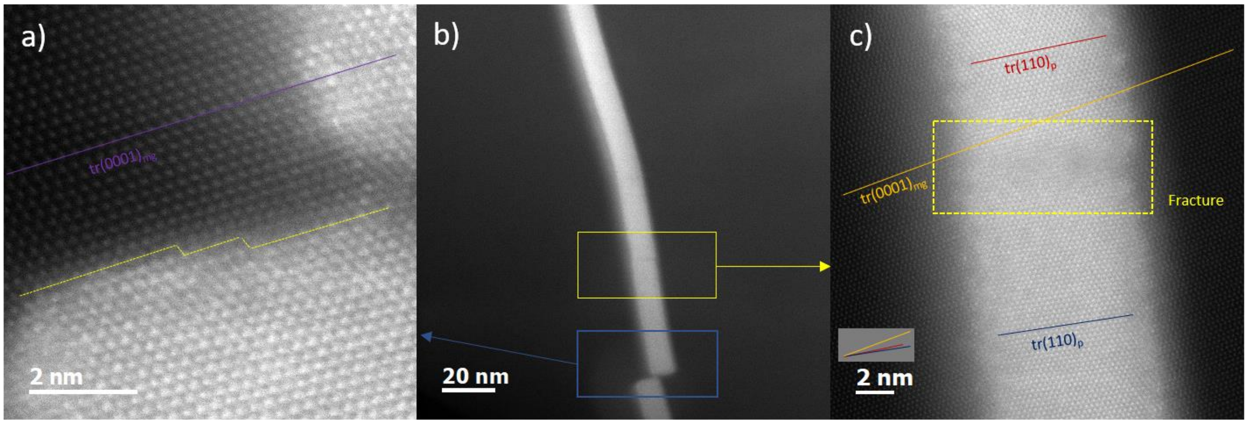

Fig. 7. 8 HAADF-STEM images of a sheared precipitate from a compression sample. Image a) and c) are the high resolution images of boxes in image b). Image a) shows the fragmentation surface is irregular facets on different planes. Image c) shows another fragment with no significant displacement inside the precipitate. The slip planes of both precipitates and matrix are marked by different color lines. The orientations of different slip planes are compared in the inset in image c).

7.3 Discussion

7.3.1 Interaction of Slip band with β_1 precipitates in tensile samples

The high resolution HAADF-STEM images Fig. 7.2 and 7.3 show that the deformed layer maintains a certain periodicity within each slip plane but exhibits a shuffling effect between adjacent $(110)_p$ planes. In addition, the double headed arrows in Fig. 7.2 show the length at each $(110)_p$ slip plane is almost identical. Therefore, it is hypothesized that the observed precipitate interacted with dislocations from multiple adjacent slip planes within the deformation band. Regardless of the shift, the deformation layers in these deformed precipitates have a similar dimension along the [0001] direction which is approximately 20nm. Multiple dislocations pile-ups are presumed to form within this layer. A schematic of hypothesized deformation mechanism is shown in Fig. 7.9.

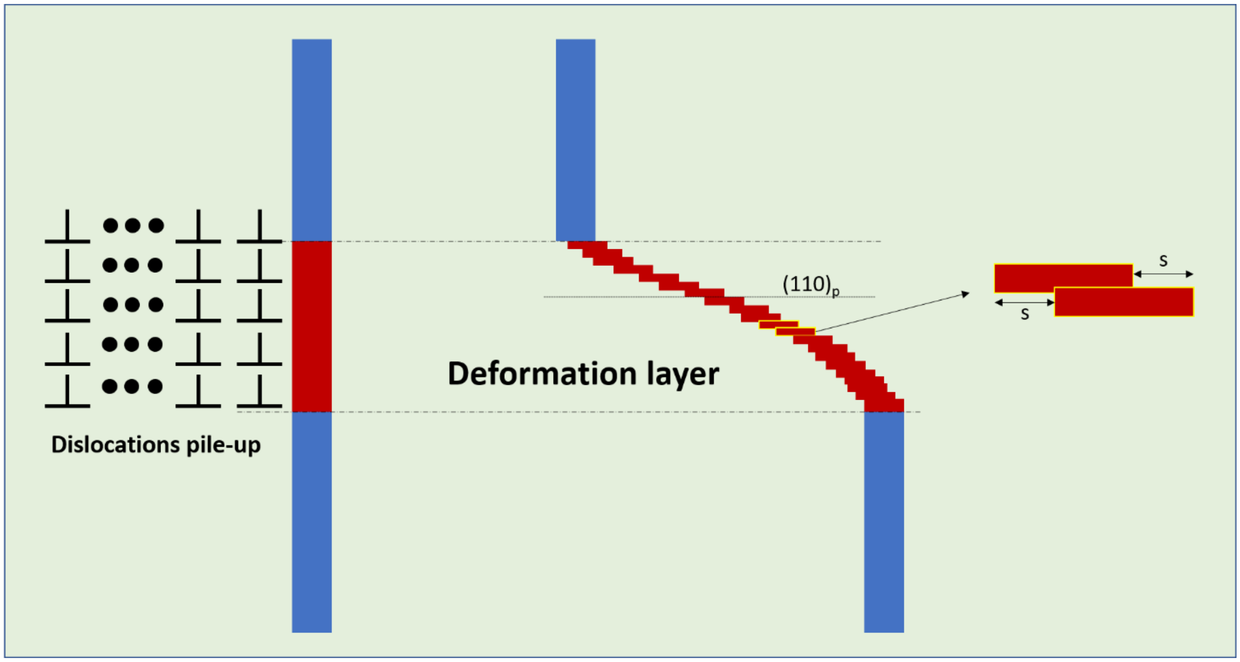

Fig. 7. 9 Schematic illustration of interaction mechanism between the slip band and β_1 precipitates. Successive adjacent slip bands combine to form the deformed layer.

As shown in the schematic, the deformation layer consists of a series of parallel slip plane which are corresponding to the dense dislocations pile-ups within the slip band. The shift between each slip plane depends on the number of dislocations that shear through, and hence appear to be fairly random. The summation of each slip plane shift results in an overall offset of the deformed precipitate as seen in Fig. 7.2.

The formation mechanism of observed slip bands is important to discuss since they commonly appear within the deformed samples. It is well known that cross-slip can thicken the slip band [81] at a macro-scale. At the nano-scale, as shown by the MD simulations results from Chapter 5, the cross-slipped dislocation components behave as immobile dislocations in the original propagation direction, potentially preventing the motion of incoming dislocations. The cross-slipped dislocations components normally extend 10-30nm out of original plane as shown in Fig. 5.3, which is in a good agreement with the dimension of the observed deformation layer. The low CRSS of the magnesium basal slip mode may contribute to this phenomenon as well.

The dislocations pile-ups amplify the local shear stress to shear through the strong β_1 precipitates. The previous DFT simulations in Chapter 6 (Fig. 6.6 and Table 6.1) shows that the lowest CRSS required to shear the precipitate is 250 MPa and easily may be above 400MPa if the slip system between precipitate and matrix is not well aligned. Under such a high local stress, additional mechanisms may also be involved during the shearing events such as local diffusion or phase transformations. As shown in Fig. 7.3, the deformed structure does not strictly maintain a perfect β_1 precipitate structure between the individual slip planes, which require more dedicated investigations in the future.

7.3.2 Fragmentation in compressed samples

As shown in Fig. 7.7, deformed precipitates in the compressed samples tend to undergo multiple fragmentation rather than going through a structural distortion when interacting with the slip bands. By comparing Fig. 7.5 and 7.6, it is observed that the compressive stress applied on the c-axis which is parallel to precipitate broad facet plays a critical rule on determining the deformation behavior. As the compressive twin was observed in studied sample in Fig. 7.6, the observed precipitates in Fig. 7.5 appear to be under a buckling condition. Precipitates receive compressive stress from both ends and a small deflection will result in fragmentation and eventual fracture. Similar plastic buckling phenomenon was also observed in many other alloys under compression condition, which include β_1 precipitate in magnesium MN11 alloys [31], θ’ plates in Al-Cu alloys [82, 83] and S precipitates in Al-Cu-Mg alloys [84].

Basal slip band will frequently coexist with plastic buckling phenomenon since the applied stress is unlikely to apply exactly along c axis. The deformation behavior observed in Fig. 7.5 is thus the consequence of both mechanisms, in which the array of precipitates is under high compressive stress and the precipitate fragmentation is trigger by dislocations pile-up. A schematic of the hypothesized mechanism is illustrated in Fig. 7. 10 where small deflection is caused by dislocations shearing leading to a buckling instability for the sheared component, which will rotate in the matrix and subsequentially result in fracture. The $(110)_p$ slip plane indicates such precipitate rotation in the matrix.

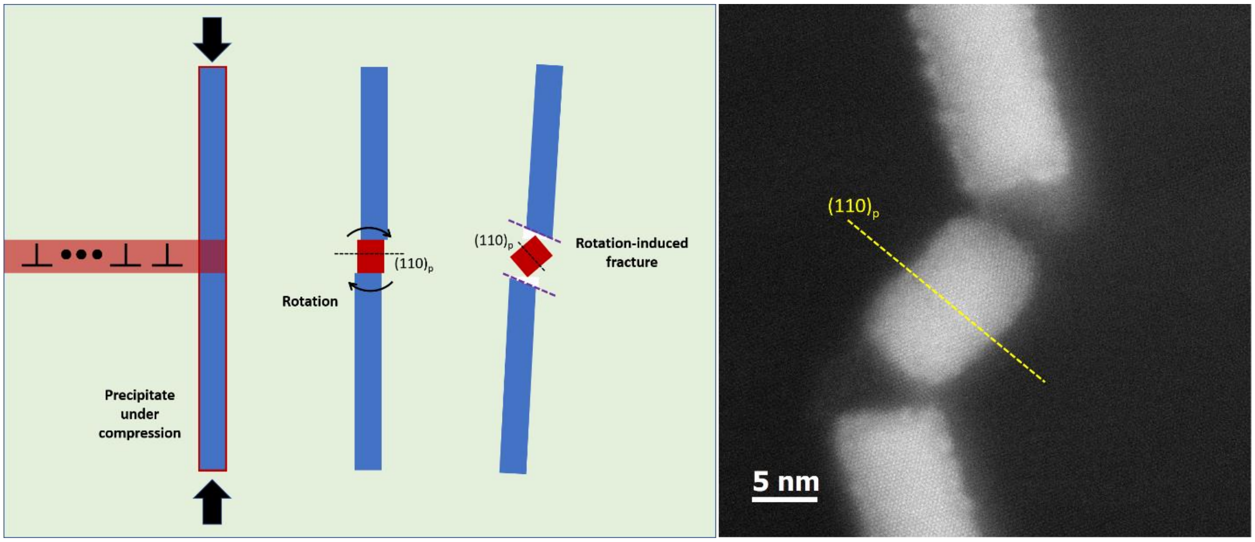

Fig. 7. 10 Hypothesized fragmentation mechanism for precipitates under compression. The red lines surrounding the precipitate represent as stress field under compression. Rightmost image is the HAADF-STEM image showing deformed structure similar to Fig. 7.7.

7.4 Conclusions

The structure of deformed β_1 precipitates in tensile and compressive sample is characterized by HAADF-STEM images. The shearing mechanism is different in these two conditions. The major characterization can be included as following:

1. Precipitates in tensile samples show a large shearing offset but still maintain connection after deformation. High resolution HAADF-STEM images suggest multiple dislocations shearing in a confined layer. This phenomenon is hypothesized as interaction with a nano-scale slip band. Within the deformation layer, each individual slip plane shift randomly between adjacent planes. The summation of these shifts contributes to the total shearing offset.
2. Precipitates in compressive samples show plastic buckling when the applied compressive stress is parallel to the c-axis. Dislocations shearing will trigger the precipitate fragmentation which will rotate in the matrix due to the buckling instability and eventually result in rotation-induced fracture.

CHAPTER 8

Conclusion Remarks and Future Work

Dislocation-precipitate interactions in Mg-Nd alloys have been characterized by *in situ* straining and postmortem TEM in this thesis. The two types of precipitates, β''' and β_1, investigated here represent different interaction mechanisms with gliding dislocations. The deformation mechanism for fine and coherent β''' precipitates follow the fashion of classical shearing which can be sheared by single dislocation and leave an offset at shearing plane. On the other hand, coarse and non-equaixed precipitates with high intrinsic strength such as β_1 precipitates are resistant to dislocations shearing. The interaction mechanisms are highly dependent on gliding dislocation characteristic and interaction configurations. As shown in Chapter 4 and 5, edge dislocation with propagation direction parallel to broad facet will spontaneously glide to the precipitate end at a lower bowing stress than that expected from Orowan looping. A screw dislocation can pass over precipitates via double cross-slip analogous to the Hirsch mechanism. When the dislocation motion direction is perpendicular to the precipitate broad facet, dislocations are able to pile-up in front of blocking precipitates as shown in Chapter 6. Such high intensity pile-up will form as nano-scale slip band and increase the local shear stress high enough to shear through the strong β_1 precipitates. Therefore, it can be concluded that there are a variety of possible dislocation-precipitate interaction mechanism with β_1 precipitates. The activated mechanisms are associated with specific dislocation-precipitate configurations. The mechanical behaviors of aged hardened magnesium alloy are governed by the contribution of each mechanisms.

In the future work, it will be important to understand the relationship between these observed dislocation-precipitate interaction mechanisms and their relationship with the associated mechanical behavior. Specifically, *in situ* investigations on single grain with controlled dislocation-precipitate interaction configuration would be useful to isolate mechanical contribution from individual mechanisms. It would also be helpful to study these phenomena with computational simulations such as Dislocation Dynamics (DD), using these observed mechanisms as inputs to at least understand the mechanical properties in single crystal. Another aspect is to utilize cold work before aging to provide higher precipitate density. Premature characterizations show a dramatical increment on β_1 precipitates density as shown in Fig. 8.1. It is of interests to characterize the precipitate-dislocation interaction in this high density precipitates microstructure. Moreover, further investigation can modify the alloy composition to design a desired precipitation hardened microstructure based on these observed dislocation-precipitate interaction principles.

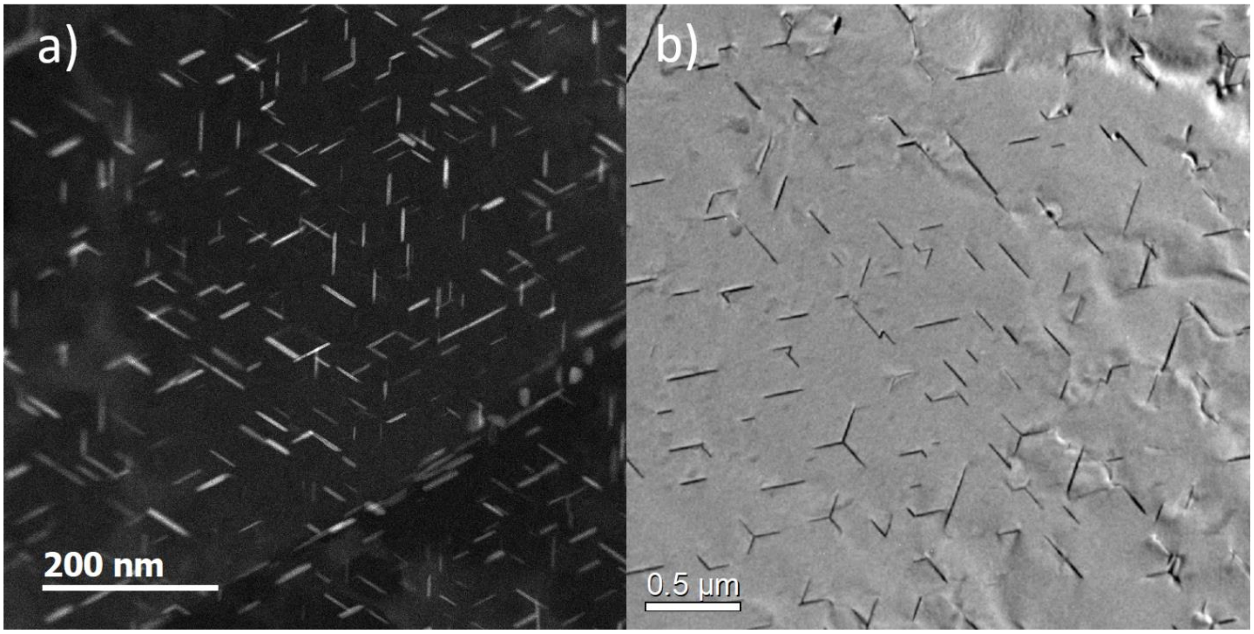

Fig. 8. 1 β_1 precipitates distribution of a) 30 mins aging at 250oC after 10% cold rolling b) 9 hours aging at 250oC without cold work. Electron beam is parallel to [0001] in both images.

REFERENCES

[1] Partirdge PG., The crystallography and deformation modes of hexagonal close-packed metals, Metall.Review,1967:12:169.

[2] Couret, A., and D. Caillard. "An in situ study of prismatic glide in magnesium—I. The rate controlling mechanism." Acta metallurgica 33.8 (1985): 1447-1454.

[3] Escaig, B. "L'activation thermique des déviations sous faibles contraintes dans les structures hc et cc Par." physica status solidi (b) 28.2 (1968): 463-474.

[4] CHINO Y, KIMURA K, HAKAMADA M, MABUCHI M. Mechanical anisotropy due to twinning in an extruded AZ31 Mg alloy[J]. Materials Science and Engineering A, 2008, 485: 311−317.

[5]Obara T., Yoshinaga H., Morozumi S., {11-22}<-1-123> slip system in magnesium, Acta Mater., 1973:21:845.

[6] Stohr JF., Poirier JP., Etude en Microscopie Electronique de Glissement Pyramidal {1122}<1123> dans le Magnesium. Phil. Mag., 1972:25:1313.

[7] Xie, K. Y., Alam, Z., Caffee, A., & Hemker, K. J. (2016). Pyramidal I slip in c-axis compressed Mg single crystals. Scripta Materialia, 112, 75-78.

[8] Tang, Y., & El-Awady, J. A. (2014). Formation and slip of pyramidal dislocations in hexagonal close-packed magnesium single crystals. Acta Materialia, 71, 319-332.

[9] Wu, Z., Ahmad, R., Yin, B., Sandlöbes, S., & Curtin, W. A. (2018). Mechanistic origin and prediction of enhanced ductility in magnesium alloys. Science, 359(6374), 447-452.

[10] Rosenbaum HS., Nonbasal slip in hcp metals and its relation to mechanical

twinning, Deformation Twinning. Gordon and Breach, New York, 1964.

[11] Sandlöbes, S., Friák, M., Neugebauer, J., & Raabe, D. (2013). Basal and non-basal dislocation slip in Mg–Y. Materials Science and Engineering: A, 576, 61-68.

[12] Agnew, S. R., Capolungo, L., & Calhoun, C. A. (2015). Connections between the basal I1 “growth” fault and< c+ a> dislocations. Acta Materialia, 82, 255-265.

[13] Taylor, Geoffrey Ingram. "Plastic strain in metals." J. Inst. Metals 62 (1938): 307-324.

[14] Wu, Zhaoxuan, and W. A. Curtin. "The origins of high hardening and low ductility in magnesium." Nature 526.7571 (2015): 62.

[15] Geng, J., Chisholm, M. F., Mishra, R. K., & Kumar, K. S. (2014). The structure of⟨ c+ a⟩ type dislocation loops in magnesium. Philosophical Magazine Letters, 94(6), 377-386.

[16] Stanford, N., Geng, J., Chun, Y. B., Davies, C. H. J., Nie, J. F., & Barnett, M. R. (2012). Effect of plate-shaped particle distributions on the deformation behaviour of magnesium alloy AZ91 in tension and compression. Acta materialia, 60(1), 218-228.

[17] Koike, J., Kobayashi, T., Mukai, T., Watanabe, H., Suzuki, M., Maruyama, K., & Higashi, K. (2003). The activity of non-basal slip systems and dynamic recovery at room temperature in fine-grained AZ31B magnesium alloys. Acta materialia, 51(7), 2055-2065.

[18] Agnew, Sean R., and Özgür Duygulu. "Plastic anisotropy and the role of non-basal slip in magnesium alloy AZ31B." International Journal of plasticity 21.6 (2005): 1161-1193.

[19] Sand Sandlöbes, S., Zaefferer, S., Schestakow, I., Yi, S., & Gonzalez-Martinez, R. (2011). On the role of non-basal deformation mechanisms for the ductility of Mg and Mg–Y alloys. Acta Materialia, 59(2), 429-439.

[20] Sandlöbes, S., Pei, Z., Friák, M., Zhu, L. F., Wang, F., Zaefferer, S., ... & Neugebauer, J. (2014). Ductility improvement of Mg alloys by solid solution: Ab initio modeling, synthesis and mechanical properties. Acta Materialia, 70, 92-104.

[21] Sandlöbes, S., Friák, M., Zaefferer, S., Dick, A., Yi, S., Letzig, D., ... & Raabe, D. (2012). The relation between ductility and stacking fault energies in Mg and Mg–Y alloys. Acta Materialia, 60(6-7), 3011-3021.

[22] Yin, B., Wu, Z., & Curtin, W. A. (2017). First-principles calculations of stacking fault energies in Mg-Y, Mg-Al and Mg-Zn alloys and implications for< c+ a> activity. Acta Materialia, 136, 249-261.

[23] Zheng, K. Y., Dong, J., Zeng, X. Q., & Ding, W. J. (2008). Precipitation and its effect on the mechanical properties of a cast Mg–Gd–Nd–Zr alloy. Materials Science and Engineering: A, 489(1-2), 44-54.

[24] Zhou, B., Wang, L., Zhu, G., Wang, J., Wen, W., & Zeng, X. (2018). Understanding the Strengthening Effect of β_1 Precipitates in Mg-Nd Using In Situ Synchrotron X-ray Diffraction. JOM, 70(10), 2315-2320.

[25] Bhattacharyya, J. J., Nakata, T., Kamado, S., & Agnew, S. R. (2019). Origins of high strength and ductility combination in a Guinier-Preston zone containing Mg-Al-Ca-Mn alloy. Scripta Materialia, 163, 121-124.

[26] Bhattacharyya, J. J., Sasaki, T. T., Nakata, T., Hono, K., Kamado, S., & Agnew, S. R. (2019). Determining the strength of GP zones in Mg alloy AXM10304, both parallel and perpendicular to the zone. Acta Materialia, 171, 231-239.

[27] Nie, J. F. (2014). Physical metallurgy of light alloys. In Physical metallurgy (pp. 2009-2156). Elsevier.

[28] Natarajan, A. R., Solomon, E. L., Puchala, B., Marquis, E. A., & Van der Ven, A. (2016). On the early stages of precipitation in dilute Mg–Nd alloys. Acta Materialia, 108, 367-379.

[29] H. Liu, Y.M. Zhu, N.C. Wilson, J.F. Nie, "On the structure and role of β'_F in β_1 precipitation in Mg-Nd alloys", Acta Materialia, 133 (2017) 408-426.

[30] Nie, J. F., & Muddle, B. C. (2000). Characterisation of strengthening precipitate phases in a Mg–Y–Nd alloy. Acta materialia, 48(8), 1691-1703.

[31] Cepeda-Jiménez, C. M., Castillo-Rodríguez, M., & Pérez-Prado, M. T. (2019). Origin of the low precipitation hardening in magnesium alloys. Acta Materialia, 165, 164-176.

[32] Courtney, T.H., Mechanical Behavior of Materials, ed. B.J. Clark and J.M. Morriss. 1990, New York, NY: McGraw-Hill, Inc

[33] R. C. CRAWFORD and I. L. F. RAy, Phil. Mag. 35, 549 (1977).

[34] Orowan, E. (1948). Internal stress in metals and alloys. The Institute of Metals, London, 451.

[35] Gladman, T. (1999). Precipitation hardening in metals. Materials science and technology, 15(1), 30-36.

[36] Brown LM, Ham RK. In: Kelly A, Nicholson RB, editors. Strengthening methods in crystals. London: Elsevier Publishing Company; 1971. p. 12.

[37] Ardell, A. J. "Precipitation hardening." *Metall. Mater.Trans A* 16.12 (1985): 2131-2165.

[38] Zhu, A. W., and E. A. Starke. "Strengthening effect of unshearable particles of finite size: a computer experimental study." *Acta Mater.* 47.11 (1999): 3263-3269.

[39] Nie, J.F., Muddle, B.C. and Polmear, I.J.,Mater. Sci.Forum, 1996,217-222, 1257.

[40] J.F. Nie Effects of precipitate shape and orientation on dispersion strengthening in magnesium alloys *Scr. Mater.*, 48 (2003), pp. 1009–1015

[41] Arzt, Eduard, and D. S. Wilkinson. "Threshold stresses for dislocation climb over hard particles: The effect of an attractive interaction." *Acta Metallurgica* 34.10 (1986): 1893-1898.

[42] Sun, F., Gu, Y. F., Yan, J. B., Zhong, Z. H., & Yuyama, M. (2015). Dislocation motion in a NI-Fe-based superalloy during creep–rupture beyond 700 C. Materials Letters, 159, 241-244.

[43] Vaid, A., Guénolé, J., Prakash, A., Korte-Kerzel, S., & Bitzek, E. (2019). Atomistic simulations of basal dislocations in Mg interacting with Mg17Al12 precipitates. Materialia, 7, 100355.

[44] Ahmad, R., Groh, S., Ghazisaeidi, M., & Curtin, W. A. (2018). Modified embedded-atom method interatomic potential for Mg–Y alloys. Modelling and Simulation in Materials Science and Engineering, 26(6), 065010.

[45] Stroh, A. N. "Dislocations and cracks in anisotropic elasticity." Philosophical magazine 3.30 (1958): 625-646.

[46] Bacon, D. J., Osetsky, Y. N., Rodney, D. Dislocation-obstacle interactions at the atomic level. In Dislocations in Solids (Eds. Hirth, J. P., Kubin, L.), 15, 1–90, Elsevier, Amsterdam 2009.

[47] Kresse, Georg, and Jürgen Furthmüller. "Efficient iterative schemes for ab initio total-energy calculations using a plane-wave basis set." Physical review B 54.16 (1996): 11169.

[48] Kresse, Georg, and D. Joubert. "From ultrasoft pseudopotentials to the projector augmented-wave method." Physical Review B 59.3 (1999): 1758.

[49] Perdew, John P., et al. "Atoms, molecules, solids, and surfaces: Applications of the generalized gradient approximation for exchange and correlation." Physical Review B 46.11 (1992): 6671.

[50] J.F. Nie, Precipitation and hardening in magnesium alloys, Metall. Mater.Trans. A 43 (2012) 3891-3939..

[51] Antion C, Donnadieu P, Perrard F, Deschamps A, Tassin C, Pisch A. "Hardening precipitation in a Mg–4Y–3RE alloy." Acta Mater. 51.18 (2003): 5335-5348.

[52] Apps, P. J., H. Karimzadeh, J. F. King, and G. W. Lorimer "Precipitation reactions in magnesium-rare earth alloys containing yttrium, gadolinium or dysprosium." Scr. Mater. 48.8 (2003): 1023-1028.

[53] Gao, Xiang, S. M. He, X. Q. Zeng, L. M. Peng, W. J. Ding, and J. F. Nie. "Microstructure evolution in a Mg–15Gd–0.5 Zr (wt.%) alloy during isothermal aging at 250 C Mater. Sci. Eng. A 431, no. 1 (2006): 322-327.

[54] Ahmed M, Lorimer GW, Lyon P, Pilkington R. In: Mordike BL, Hehmann F, editors. Proc magnesium alloys and their applications. Oberursel: DGM Informationsgesellschaft; 1992. p. 301.

[55] Liu, Hong, Yunzhi Wang, and Jian-Feng Nie. "Phase Field Simulation of Orowan Strengthening by Coherent Precipitate Plates in a Mg ‑ Nd Alloy." Proceedings of the 3rd World Congress on Integrated Computational Materials Engineering (ICME 2015). John Wiley & Sons, Inc., 2015.

[56] Burke, E. C., and W. R. Hibbard. The plastic deformation of magnesium single crystals. publisher not identified, 1951.

[57] Häussler, D., Bartsch, M., Messerschmidt, U., & Reppich, B. "HVTEM in situ observations of dislocation motion in the oxide dispersion strengthened superalloy MA 754." Acta Mater. 49.18 (2001): 3647-3657.

[58] Gao, Huajian, Lin Zhang, and Shefford P. Baker. "Dislocation core spreading at interfaces between metal films and amorphous substrates." Journal of the Mechanics and Physics of Solids 50.10 (2002): 2169-2202.

[59] Wang, J., Hoagland, R. G., Liu, X. Y., & Misra, A. "The influence of interface shear strength on the glide dislocation–interface interactions." Acta Mater. 59.8 (2011): 3164-3173.

[60] Xu, Z., M. Weyland, and J. F. Nie. "On the strain accommodation of β_1 precipitates in magnesium alloy WE54." Acta Mater. 75 (2014): 122-133.

[61] Yasi, Joseph A., Louis G. Hector Jr, and Dallas R. Trinkle. "Prediction of thermal cross-slip stress in magnesium alloys from direct first-principles data." Acta Materialia 59.14 (2011): 5652-5660.

[62] Yasi, Joseph A., Louis G. Hector Jr, and Dallas R. Trinkle. "Prediction of thermal cross-slip stress in magnesium alloys from a geometric interaction model." Acta Materialia 60.5 (2012): 2350-2358.

[63] Clark, J. B. (1968). Age hardening in a Mg-9 wt.% Al alloy. Acta Metallurgica, 16(2), 141-152.

[64] Liao, Min, B. Li, and M. F. Horstemeyer. "Interaction Between Basal Slip and a Mg 17 Al 12 Precipitate in Magnesium." Metallurgical and Materials Transactions A 45.8 (2014): 3661-3669.

[65] Ph.D. Thesis Solomon, Ellen L.S. “Precipitation Behavior of Magnesium Alloys Containing Neodymium and Yttrium.” University of Michigan, 2017.

[66] Bhattacharyya, J. J., Wang, F., Stanford, N., & Agnew, S. R. (2018). Slip mode dependency of dislocation shearing and looping of precipitates in Mg alloy WE43. Acta Materialia, 146, 55-62.

[67] Solomon, Ellen LS, and Emmanuelle A. Marquis. "Deformation behavior of β’ and β’’’ precipitates in Mg-RE alloys." Materials Letters 216 (2018): 67-69.

[68] Hirsch, Peter Bernhard, and F. J. Humphreys. "The deformation of single crystals of copper and copper-zinc alloys containing alumina particles-I. Macroscopic properties and work hardening theory." Proceedings of the Royal Society of London. A. Mathematical and Physical Sciences 318.1532 (1970): 45-72.

[69] Humphreys, F. J., and Peter Bernhard Hirsch. "The deformation of single crystals of copper and copper-zinc alloys containing alumina particles-II. Microstructure and dislocation-particle interactions." Proceedings of the Royal Society of London. A. Mathematical and Physical Sciences 318.1532 (1970): 73-92.

[70] Matsui, J. (1975). Cross‐Slip Dislocations and Their Multiplication in (001)‐Oriented Silicon Wafers. Journal of The Electrochemical Society, 122(7), 977-983.

[71] Yoo, M. H., Agnew, S. R., Morris, J. R., & Ho, K. M. (2001). Non-basal slip systems in HCP metals and alloys: source mechanisms. Materials Science and Engineering: A, 319, 87-92.

[72] Hidalgo-Manrique, P., J. D. Robson, and M. T. Pérez-Prado. "Precipitation strengthening and reversed yield stress asymmetry in Mg alloys containing rare-earth elements: A quantitative study." Acta Materialia 124 (2017): 456-467.

[73] Huang, Zhihua, John E. Allison, and Amit Misra. "Interaction of Glide Dislocations with Extended Precipitates in Mg-Nd alloys." Scientific reports 8.1 (2018): 3570.

[74] Argon, Ali. Strengthening mechanisms in crystal plasticity. No. 4. Oxford University Press on Demand, 2008

[75] Kim, Ki-Hyun, and Byeong-Joo Lee. "Modified embedded-atom method interatomic potentials for Mg-Nd and Mg-Pb binary systems." Calphad 57 (2017): 55-61.

[76] Chou, Y. T., and J. D. Eshelby. "The energy and line tension of a dislocation in a hexagonal crystal." Journal of the Mechanics and Physics of Solids 10.1 (1962): 27-34.

[77] Kondo, S., Mitsuma, T., Shibata, N., & Ikuhara, Y. (2016). Direct observation of individual dislocation interaction processes with grain boundaries. Science advances, 2(11), e1501926.

[78] Hirth, J. P., & Lothe, J. (1982). Theory of dislocations.

[79] Hull, D., & Bacon, D. J. (2011). Introduction to dislocations (Vol. 37). Elsevier.

[80] Nakata, T., Bhattacharyya, J. J., Agnew, S. R., & Kamado, S. (2019). Unexpected influence of prismatic plate-shaped precipitates on strengths and yield anisotropy in an extruded Mg-0.3 Ca-1.0 In-0.1 Al-0.2 Mn (at.%) alloy. Scripta Materialia, 169, 70-75.

[81] Johnston, W. G., & Gilman, J. J. (1959). Dislocation velocities, dislocation densities, and plastic flow in lithium fluoride crystals. Journal of Applied Physics, 30(2), 129-144.

[82] Embury, J. D. (1985). Plastic flow in dispersion hardened materials. Metallurgical transactions A, 16(12), 2191-2200.

[83] Harren, S. V., Deve, H. E., & Asaro, R. J. (1988). Shear band formation in plane strain compression. Acta Metallurgica, 36(9), 2435-2480.

[84] Feng, Z., Luo, X., Chen, Y., Chen, N., & Wu, G. (2019). Surface severe plastic deformation induced solute and precipitate redistribution in an Al-Cu-Mg alloy. Journal of Alloys and Compounds, 773, 585-596.